SISSA
Scuola
Internazionale
Superiore di
Studi Avanzati

Physics Area - PhD course in
Astrophysics and Cosmology

Foreground Modeling in the Context of Cosmic Microwave Background

Candidate:
Jian Yao

Advisors:
Nicoletta Krachmalnicoff
Carlo Baccigalupi

Academic Year 2023-24

Foreground Modeling in the Context of Cosmic Microwave Background © 2024 by Jian Yao.
E-mail: 1427456796@qq.com

This work is licensed under a Creative Commons "Attribution-NonCommercial-NoDerivatives 4.0 International" license.

Contents

List of Figures

List of Tables

List of Acronyms

ACT : Atacama Cosmology Telescope (experiment)

AliCPT : Ali CMB Polarization Telescope (experiment)

AME : Anomalous Microwave Emission

BAO : Baryonic Acoustic Oscillations

BBN : Big Bang nucleosynthesis

BICEP : Background Imaging of Cosmic Extragalactic Polarization (experiment)

BOOMERANG : Balloon Observations Of Millimetric Extragalactic Radiation And Geophysics (experiment)

CAMB : Code for Anisotropies in the Cosmic Microwave Background (software)

CDM : Cold Dark Matter

CIB : Cosmic Infrared Background

CL : Credible Level

CLASS : Cosmic Linear Anisotropy Solving System (software)

CMB : Cosmic Microwave Background

CNN : Convolutional Neural Network

CO : Carbon monoxide

COBE : Cosmic Background Explorer (experiment)

DASI : Degree Angular Scale Interferometer (experiment)

DL : Deep Learning

FGBuster : ForeGround Buster (software)

FLRW : Friedmann-Lemaître-Robertson-Walker

GAN : Generative Adversarial Network

GMF : Galactic Magnetic Field

GR : General Relativity

HEALPix : Hierarchical Equal Area isoLatitude Pixelization (software)

HFI : High Frequency Instrument (Planck experiment)

ICA : Independent Component Analysis (algorithm)

ILC : Internal Linear Combination (algorithm)

ISM : Interstellar medium

ISW : Integrated Sachs-Wolfe effect

kSZ : kinetic Sunyaev-Zel'dovich effect

ΛCDM : Λ Cold Dark Matter

LAT : Large Aperture Telescope

LFI : Low Frequency Instrument (Planck experiment)

LiteBIRD : Lite (Light) satellite for the studies of B-mode polarization and Inflation from cosmic background Radiation Detection (experiment)

LSS : (cosmic) Large-Scale Structure

MAXIMA : Millimeter Anisotropy eXperiment IMaging Array (experiment)

MCMC : Markov-Chain Monte Carlo (algorithm)

MFs: Minkowski Functionals

NILC : Needlet Internal Linear Combination (algorithm)

NN : Neural Network

PanEx GSWG : Pan-Experiment Galactic Science Working Group

PGW : Primordial Gravitational Waves

PNG : Primordial non-Gaussianity

POLARBEAR : POLARization of the Background Radiation experiment

PySM : Python Sky Model (software)

ReLU : Rectified Linear Unit

SAT : Small Aperture Telescope

SED : Spectral Energy Distribution

SMICA : Spectral Matching Independent Component Analysis (algorithm)

SO : Simons Observatory (experiment)

S-PASS : S-Band Polarization All Sky Survey (experiment)

SPIDER : Suborbital Polarimeter for Inflation Dust and the Epoch of Reionization

SPT : South Pole Telescope (experiment)

SW : (ordinary) Sachs-Wolfe effect

SZ : Sunyaev-Zel'dovich effect

TOD : Time Ordered Data

tSZ : thermal Sunyaev-Zel'dovich effect

WMAP : Wilkinson Microwave Anisotropy Probe (experiment)

ZE : Zodiacal Emission

ABSTRACT

The ΛCDM model has been the standard model of cosmology for several decades. With the increasing precision of current and upcoming measurements, we now have a unique opportunity to test this model with greater significance. A central focus of modern cosmology is the search for evidence of cosmic inflation. Its most promising signature is the detection of a distinct pattern in the polarization of the CMB, known as primordial B-modes, which can only be generated by gravitational waves during the inflationary epoch. However, one of the critical challenges in detecting B-modes arises from foreground emissions within our Galaxy, which dominate the CMB signal. Current experiments lack the power to fully disentangle these foregrounds, making a definitive detection of inflation elusive.

In this thesis, we aim at building upon current knowledge of foregrounds from observational data by developing a capability of simulating a diffuse foreground components that accurately captures their statistical properties. We focus specifically on thermal dust emission, which is one of the primary contaminants in polarized CMB signals. The first work consists in the development of the necessary estimators for measuring the level of non-Gaussianity using Minkowski functionals, in particular in the dust component which are currently in the `PySM3` package, an algorithmic environment which gathers the efforts by the entire CMB community in order to understand, characterize, model and simulate foreground emissions. In the second work, we introduce FORSE+, a Python package based on Neural Networks, designed to generate non-Gaussian thermal dust emission maps at arcminute resolution and in polarization, using the available information from data, with the capability of producing random realizations of small-scale structures, a feature which is essential for implementing simulations in the FORSE+. We validate these maps to ensure that their statistical properties, including power spectra and non-Gaussianity, align with real observational data.

These realistic simulations will be crucial for future studies of the impact of non-Gaussian foregrounds on CMB analysis, including lensing reconstruction, de-lensing, and the detection of cosmological gravitational waves in CMB polarization B-modes. They will significantly enhance the analysis of CMB data in upcoming experiments, such as those from the Simons Observatory and CMB-S4, ultimately pushing the boundaries of precision cosmology.

Introduction

From the steady-state model to the hot big-bang scenario where the Universe is observed to expand, and recently, at an accelerating rate, the understanding of human being for our Universe is constantly evolving. Passing from inflation, quasi-exponential expansion in the early Universe, to the dark energy which comes into dominance only recently, mysteries unanswered exist and wait for more insight. From the measured acoustic peaks in the CMB to the observed luminosity of type Ia Supernovae, every object and structure in the Universe tells a part of the story.

In this Thesis, we focus on the CMB radiation, which free streamed since when the Universe was only 380000 years old and has remained to the present day, with the age of the Universe being 14 billion years. Many of he CMB prediction has been verified by precise measurements. The next major breakthrough is expected to come from the detection of the primordial B-mode in the CMB polarization signal, a curl-like pattern that would confirm the occurrence of inflation. The possible amplitude of very faint B-mode is pushing down by detectors with ever-increasing sensitivity. Should this signal remain undetected, alternative cosmological theories may need to be considered.

From an observational perspective, it is not straightforward to detect the extremely weak B-mode signal which will require rigorous control over experimental systematics such as instrumental noise. The main challenge, however, comes from foreground emissions within our Galaxy, specifically thermal dust and synchrotron radiation, which are major contaminants to the CMB polarization signal. While there are methods to separate the foregrounds from the desired CMB signal, residual foregrounds are inevitable and can affect statistical analyses of the CMB, including two-point correlation functions (or power spectra in Fourier space) and higher-order statistics like non-Gaussianity.

Knowledge from observational side is of vital importance to understand the foregrounds, which is currently limited in terms of both frequency range and resolution, mostly derived from the dedicated experiments for CMB detection. Modeling the foregrounds is crucial to bridging the gap between the experimental knowledge and the foregrounds at smaller scales and unexplored frequencies.

In this Thesis, we investigate the thermal dust maps from two foreground models. One is `PySM3`, which integrates the latest development of the widely used `PySM2` from the PanEx GSWG. In particular my contribution consists in implementing the suitable

estimators to measure the level of non-Gaussianity in the newly obtained maps. The other is called ForSE+, with important extensions to the previous version of ForSE. In this work, rooted in machine learning which absorbs and reproduces information from existing data, we reach the arcminute scale for simulating thermal dust, as required by operating and future B-mode observations, and we comprehensively validate the produced maps from various perspectives, such as power spectra and level of non-Gaussianity. These new foreground models provide essential ingredients in the integrated pipeline to obtain the estimation of cosmological parameters.

This Thesis is organized as follows.

In Chapter 1, we introduce the standard model of cosmology, the ΛCDM, based on Einstein's GR. The cosmological principles are valid at largest scales, postulating a smooth background. On top of this background we then consider small fluctuations which grow to form the structures in the Universe. The initial condition for these fluctuations are widely believed to set by the inflation, which we will discuss in details at the end of this Chapter.

In Chapter 2, we focus on the basics physics and mathematics for describing CMB, which represents one of the most powerful probe of inflation. After that we discuss about the shape of observed power spectra of CMB total intensity and polarization, highlighting the specific pattern in the polarized CMB map that can only be sourced by the tensor perturbations during inflation. Before closing this Chapter, we review the latest measurements of CMB signals and highlight several future experiments.

In Chapter 3, we present the current knowledge about foregrounds, including the physical mechanism for them, the phenomenological modeling for different components and their observed properties. We then describe how they contaminate the detection of CMB signal, in terms of both the power spectrum and higher order statistics such as non-Gaussianity. Methods to separate the contribution from foregrounds to CMB are then introduced. The understanding of foregrounds is limited by the observational constraints and we review the latest models that try to extrapolate the acquired knowledge to the uncovered frequencies and resolutions.

In Chapter 4, we present our contribution to the new version of `PySM3` package. We begin with a summary of the new aspects of `PySM3` compared with the older version, which include implementation of new models for foregrounds and new templates. We then introduce the basic properties of Minkowski functionals, with which we try to measure the level of non-Gaussianity contained in the maps from new models.

In Chapter 5, our work dealing with the exploitation of machine learning techniques in order to simulate small scales of foregrounds is presented. The ForSE+ model extends the capabilities of its predecessor ForSE by reaching smaller scales and enabling the generation of random realizations. We first introduce the fundamentals of neural networks and the basics of the status of the art of the implementation. We then describe the new approach for reaching arcminute scale resolution in polarization and after detailing the new model, we thoroughly validate the generated maps from various perspectives.

Finally, in the Conclusions, we summarize the main results of this thesis, which include

the development of new foreground models and open a new area of research for the actual simulation of the CMB contaminants in polarization and reaching the arcminute resolution. We also discuss the potential applications in the context of cosmological inference from CMB observations.

1

ΛCDM **Cosmology**

Let us talk about the universe!

The current standard model of cosmology is the ΛCDM model, which we describe in extreme synthesis here in this first Chapter: as we discuss below, the universe today is expanding and dominated by **dark energy** (Λ) and **cold dark matter** (CDM), and it assumes that Einstein's general relativity (GR) is the correct theory of gravity on cosmological scales, where the geometry of space is almost flat. We now briefly address these main features.

- Λ, the cosmological constant, is the simplest form of the dark energy, which is the component responsible for cosmic acceleration (Riess et al., 1998; Perlmutter et al., 1999). It was first introduced by Einstein (Einstein, 1917) in his field equations to counterbalance the effect of gravity and achieve a **static** universe, which was the accepted view at that time. Later, it has been recognized as capable of causing cosmic acceleration, interpreted as the energy density of empty space, or vacuum energy, supported by current cosmological measurements.

- Cold dark matter, the matter interacting at most weakly with light proposed to explain the the stability and growth of structure in the universe (Zwicky, 2009; Rubin & Ford, 1970). It is thought to be non-baryonic (matter other than protons, neutrons and electrons[1]), does not interact with ordinary baryonic matter and radiation except

[1] Although electrons are not baryons, they are interestingly classified as *baryons* by the cosmol-

through gravity and possibly weak interactions which makes it difficult to detect, hence the name "dark", and has negligible energy momentum compared to mass, hence "cold" (Bertone & Hooper, 2018).

- Ordinary matter, observed as atoms, chemical elements, gas and plasma.

Besides the the inclusion of the main components in the universe, ΛCDM also implies a dynamical thermal history starting from a **big bang**, which is an extremely hot and dense state in the early stages of the cosmological evolution, which lasts for about 13.8 billions years (Planck Collaboration VI, 2020). At early times all particles are constantly colliding with each other and are thus in a thermal equilibrium state. Then particles fall out of thermal equilibrium when their interaction rate drops below the expansion rate of the universe. When the universe is at the age of $t \approx 1$ second, neutrinos decouple from the thermal bath constituting the **cosmic neutrino background**. After that, light elements, mostly hydrogen, helium and lithium, begin to form within $t \approx 3$ minutes (Weinberg, 1977) and this process is called **Big Bang nucleosynthesis** (BBN). At around $t \approx 380000$ years, the universe has cooled enough for the decoupling between photons and electrons which leads to the formation of the first *stable* neutral hydrogen atoms, a process which is known as **recombination**, producing the **cosmic microwave background** (CMB) which we observe. After recombination the universe remains in a neutral state and this epoch is usually known as Dark ages because there are no light sources other than the gradually diluting cosmic background radiation[2], and the gas clouds begin to collapse, silently in the dark environment with no visible light. The first stars—called **population III stars**—form when $t \approx 100$ million years, and emit ultraviolet light to heat and ionize the surrounding gas, leading the universe to a **reionization** state. The first galaxies start to appear nearly at $t \approx 1$ billion years. Recently when $t \approx 9$ billion years, dark energy starts to dominate the universe causing an accelerating expansion until now.

As the standard model of modern cosmology, ΛCDM is supported by modern cosmological observations, and described by a small number of parameters, as we will see later in this chapter. The observational data include the Hubble diagram that describes the accelerating expansion of the universe observed in the light from distant galaxies and supernovae (Riess et al., 1998; Perlmutter et al., 1999); light element abundances from BBN (Cooke et al., 2018); temperature and polarization information in the CMB that agree well with theory (Planck Collaboration V, 2020); and multiple probes of large-scale structure in the distribution of galaxies (e.g., Anderson et al. (2012)). We will now have a detailed look of ΛCDM model from a mathematical perspective.

---

ogists.

[2]There are also small amount of photons occasionally released by neutral hydrogen atoms, known as the 21 cm line emission, which is produced by the spin-flip transition of the electron in the hydrogen atom.

1.1 Expanding Universe

We know the universe is expanding, which means that the physical distance between galaxies increases with time. It is conventional to introduce the **scale factor,** a, and **comoving distance,** χ. The comoving distance is defined in a coordinate system which follows the expansion of the universe. The scale factor describes the expansion (or contraction, if possible) of the universe. Therefore the physical distance has the form of $x = a\chi$.

A direct effect of the expansion is that the physical wavelength of a photon emitted from a distant galaxy will be stretched out proportionally to the scale factor, which is called **cosmological redshift**. And it is convenient to define the stretching effect as redshift z through the ratio between the emitted and observed wavelengths:

$$1 + z \equiv \frac{\lambda_{\rm obs}}{\lambda_{\rm emit}} = \frac{a_{\rm obs}}{a_{\rm emit}} = \frac{1}{a_{\rm emit}}, \tag{1.1}$$

where in the last equality the scale factor today is assumed to be 1 by convention. The scale factor, cosmological time, and redshift are equivalently used as markers of the cosmological expansion and thermal history.

1.1.1 Friedmann-Lemaître-Robertson-Walker metric

Non-relativistic classical mechanics treats *time* as a universal quantity of measurement which is uniform throughout *space*, and separate from space. In the context of special relativity (SR), time cannot be separated from the three dimensions of space, because the observed rate at which time passes for an object depends on the object's velocity relative to the observer. GR generalizes SR and modifies Newton's law of universal gravitation, providing a unified description of gravity as a geometric property of space and time, the four-dimensional **spacetime**.

Spacetime has its own geometry. The appearance of objects at cosmological distances is affected by the curvature of spacetime through which light travels. In GR, the fundamental quantity is the **metric** which describes the geometry of spacetime. For example, in three-dimensional Euclidean space, the physical distance between two points separated by the infinitesimal coordinate distances $\mathrm{d}x$, $\mathrm{d}y$ and $\mathrm{d}z$ is

$$\mathrm{d}\ell^2 = \mathrm{d}x^2 + \mathrm{d}y^2 + \mathrm{d}z^2 = \sum_{i,j=1}^{3} g_{ij}\ \mathrm{d}x^i\ \mathrm{d}x^j, \tag{1.2}$$

where $g_{ij} = \mathrm{diag}(1,1,1)$ and $\left(x^1, x^2, x^3\right) = (x, y, z)$. In spherical polar coordinates, the physical distance can be written as

$$\mathrm{d}\ell^2 = \mathrm{d}r^2 + r^2(\ \mathrm{d}\theta^2 + \sin^2\theta \mathrm{d}\phi^2) = \sum_{i,j=1}^{3} g_{ij}\ \mathrm{d}x^i\ \mathrm{d}x^j, \tag{1.3}$$

where in this case $g_{ij} = \mathrm{diag}(1, r^2, r^2 \sin^2\theta)$ and $\left(x^1, x^2, x^3\right) = (r, \theta, \phi)$. In these two cases $\mathrm{d}\ell^2$ is invariant so the metric plays a role that turns coordinate distances which may vary with coordinates into the physical distances. We can write distances in spacetime as

$$ds^2 = \sum_{\mu,\nu=0}^{3} g_{\mu\nu} dx^\mu dx^\nu, \tag{1.4}$$

where the indices μ and ν range from 0 to 3, with the first one reserved for the time-like coordinate (e.g., $x^0 = t$) and the last three for spatial coordinates. In SR the spacetime is Minkowski, where the metric is simply $g_{\mu\nu} = \mathrm{diag}(\text{-}1,\ 1,\ 1,\ 1)$ and the associated spacetime curvature vanishes. For GR, on the other hand, the metric will depend on the position and incorporate the effects of gravity as spacetime curvature. We now want to derive the form of metric in the expanding universe with a smooth background.

Cosmological Principles state that the universe, on scales much larger than galaxies, has the following basic features:

- Homogeneity: any physical quantity does not depend on the spatial coordinate.
- Isotropy: any physical quantity does not depend on directions.

The spatial homogeneity and isotropy of the universe mean that it can be represented by a time-ordered sequence of three-dimensional spatial slices, each of which is homogeneous and isotropic and evolve in time. The metric now has the form

$$\mathrm{d}s^2 = -c^2\ \mathrm{d}t^2 + a^2(t)\mathrm{d}\ell^2, \tag{1.5}$$

where $\mathrm{d}\ell^2$ encodes the spatial metric on each slice and $a(t)$ is the scale factor.

Homogeneous and isotropic three-spaces must have constant intrinsic curvature (Weinberg, 2008). There are then only three options: the curvature of the spatial slices can be zero, positive or negative for flat, spherical and hyperbolic spaces, respectively, and $\mathrm{d}\ell^2$ can be written in spherical polar coordinates as (see proof in Weinberg (2008); Baumann (2022))

$$\mathrm{d}\ell^2 = \frac{\mathrm{d}r^2}{1 - kr^2} + r^2(\ \mathrm{d}\theta^2 + \sin^2\theta \mathrm{d}\phi^2), \tag{1.6}$$

where k can have three possible values for different geometries:

$$k = \begin{cases} > 0 & \text{Spherical ,} \\ < 0 & \text{Hyperbolic ,} \\ 0 & \text{Flat .} \end{cases} \tag{1.7}$$

It reduces to Eq.1.3 in the flat, Euclidean space case. Combing Eq.1.5 and 1.6, the complete form for the metric is

$$\mathrm{d}s^2 = -c^2\mathrm{d}t^2 + a^2(t)\left[\frac{\mathrm{d}r^2}{1 - kr^2} + r^2(\ \mathrm{d}\theta^2 + \sin^2\theta \mathrm{d}\phi^2)\right], \tag{1.8}$$

which is called the **Friedmann-Lemaître-Robertson-Walker** (FLRW, Friedmann (1922); Lemaître (1931); Robertson (1935); Walker (1937)) metric of cosmology.

In a flat universe with above symmetries and using Euclidean coordinates instead, the metric has a simple form

$$g_{\mu\nu} = \begin{pmatrix} -c^2 & 0 & 0 & 0 \\ 0 & a^2(t) & 0 & 0 \\ 0 & 0 & a^2(t) & 0 \\ 0 & 0 & 0 & a^2(t) \end{pmatrix}, \tag{1.9}$$

which is only a function of time.

1.1.2 Einstein equations

In order to determine how the function $a(t)$ evolves with time, we need to know the composition of the constituents in the universe, and the Einstein field equations. We will discuss the constituents in the next Section and here we focus on the Einstein equations, which relate the Einstein tensor describing the geometry, to the energy-momentum tensor describing energy:

$$G_{\mu\nu} + \Lambda g_{\mu\nu} = \frac{8\pi G}{c^4} T_{\mu\nu}, \tag{1.10}$$

where $G_{\mu\nu}$ is the Einstein tensor which depends only on the metric and its derivatives, Λ is the cosmological constant, G is the Newton's constant, and $T_{\mu\nu}$ is the energy-momentum tensor, a function of the constituents of the universe. More detailed descriptions of Einstein equations can be found in any book/lecture notes on GR, such as Blau (2022).

Homogeneity and isotropy impose constraints not only on the geometry of the space-time, but also on the distribution of matter and energy, leaving us with a energy-momentum tensor being that of a perfect fluid, which is parameterized only by its global energy density $\rho(t)$ and pressure $P(t)$ as

$$T^{\mu}{}_{\nu} = g^{\mu\lambda} T_{\lambda\nu} = \begin{pmatrix} -\rho c^2 & 0 & 0 & 0 \\ 0 & P & 0 & 0 \\ 0 & 0 & P & 0 \\ 0 & 0 & 0 & P \end{pmatrix}, \tag{1.11}$$

where ρc^2 and P are the energy density and pressure in the rest frame of the fluid.

By using he FLRW metric (Eq.1.8) and the Einstein equations (Eq.1.10) along with the expression of the energy-momentum tensor (Eq.1.11) we can derive the Friedmann equations which determine the cosmological expansion, which take the form

$$\begin{aligned} H^2 \equiv \left(\frac{\dot{a}}{a}\right)^2 &= \frac{8\pi G}{3}\rho - \frac{kc^2}{a^2}, \\ \dot{H} + H^2 = \frac{\ddot{a}}{a} &= -\frac{4\pi G}{3}\left(\rho + \frac{3P}{c^2}\right), \end{aligned} \tag{1.12}$$

where we have also defined the **Hubble parameter**, $H \equiv \dot{a}/a$. We note that the above equations are not independent. The first one is known as Friedmann Equation, while the second one is the Ray Choudhury equation, which can be obtained through the Einstein equations and conservation of the energy-momentum tensor. These are the fundamental equations describing the expansion in a homogeneous and isotropic universe (i.e., a FLRW universe with the metric in Eq.1.8), which establish the relationship between the time-dependent scale factor and the time-dependent pressure and energy density of the cosmic fluid.

We now focus on the description of the cosmological constituents that we have anticipated in the current context. Before that, we conclude this Sub-Section with the definition of the **comoving horizon** as

$$\eta(t) \equiv \int_0^t \frac{cdt'}{a\left(t'\right)}. \tag{1.13}$$

No information could have propagated further on the coordinate grid than η since the beginning of time. Therefore, regions separated by distances greater than η are not causally connected. The comoving horizon can also be written as

$$\eta(a) = \int_0^a d\ln a' \frac{c}{a'H\left(a'\right)}. \tag{1.14}$$

Therefore the **comoving Hubble radius**, $1/aH$, is the approximate distance over which light can travel in the course of one expansion time, i.e., the time in which the scale factor increases by a factor of e.

1.1.3 Cosmic constituents

The ρc^2 in Eq.1.12, coming from the energy-momentum tensor (Eq.1.11), should be understood as the sum of all kinds of cosmological energy densities. We can first obtain the evolution of total energy density and momentum with time by utilizing the continuity equation for energy conservation and Euler equation for momentum conservation in the covariant form of GR:

$$\nabla_\mu T^\mu{}_\nu = 0. \tag{1.15}$$

Solving the time-time component of these equations leads to the energy conservation in the cosmological context:

$$\dot{\rho} + 3\frac{\dot{a}}{a}\left(\rho + \frac{P}{c^2}\right) = 0. \tag{1.16}$$

Most of the cosmological constituents can be parameterized in terms of a constant **equation of state**, $\omega = P/(\rho c^2)$, which allows to integrate directly Eq.1.16 and obtain

$$\rho \propto a^{-3(1+\omega)}. \tag{1.17}$$

We can distinguish three kinds of cosmological constituents through the different values of the equation of state.

- Radiation. This component is used to denote anything having a pressure equal to 1/3 of the energy density which includes relativistic particles such as photons. Eq.1.17 gives $\rho \sim a^{-4}$, showing that the dilution receives effects from both the expanding volume and the redshifting of the particle energies.

- Matter. In this case the pressure is much smaller than the energy density, $P \ll \rho c^2$. Assuming $\omega = 0$, Eq.1.17 gives us $\rho \sim a^{-3}$, which corresponds to the dilution of the energy density simply because the expansion of the volume. Matter includes ordinary matter and dark matter, as we mentioned at the beginning of this chapter.

- Dark Energy. This component has a negative pressure $P = -\rho c^2$ and does not dilute with the expansion of the space, having a constant energy density, $\rho \sim a^0$.

We now have the evolution of ρ of each single fluid as a function of the scale factor, and therefore we can solve the time-dependence of the scale factor treating the cosmic fluid as a mixture of each component and rewrite the equations in Eq.1.12:

$$\begin{aligned} \left(\frac{\dot{a}}{a}\right)^2 &= \frac{8\pi G}{3}\sum_i \rho_i - \frac{kc^2}{a^2}, \\ \frac{\ddot{a}}{a} &= -\frac{4\pi G}{3}\sum_i \rho_i \left(1 + 3w_i\right). \end{aligned} \tag{1.18}$$

It is convenient to work with the dimensionless **fractional density parameters** of each component, Ω_i, which is defined as the ratio of physical density relative to the **critical density**, $\rho_{crit,0}$[3]:

$$\Omega_i \equiv \frac{\rho_{i,0}}{\rho_{\text{crit },0}}, \quad i = r, m, \Lambda, ... \tag{1.19}$$

where $\rho_{crit,0}$ is the total energy density of universe when the universe is flat and is defined via $\rho_{crit,0} = 3H_0^2/(8\pi G)$ by setting $k = 0$ (flat) in the first equation of Eq.1.12. H_0 is the Hubble constant, the Hubble parameter evaluated at today, $t = t_0$. r and m refer to radiation and matter component respectively. With these fractional densities defined, the first equation of Eq.1.18 can now be written as

$$\frac{H^2}{H_0^2} = \Omega_r a^{-4} + \Omega_m a^{-3} + \Omega_k a^{-2} + \Omega_\Lambda, \tag{1.20}$$

where we also introduce curvature density parameter, $\Omega_k \equiv -kc^2/H_0^2$. If $\Omega_k = 0$, i.e., the universe is flat, the total density is equal to the critical one. It is one of the central

[3]We will use the subscript '0' to indicate quantities observed today from now on, unless stated otherwise.

tasks in modern cosmology to measure these density parameters and hence determine the composition of the universe.

For simplicity, here we focus on the case where there is only one dominating component, which is a valid approximation for most of the cosmological time since different components have different scalings with expansion, except at the epochs where two or more components are comparable (Baumann, 2022). Also, assuming flatness, by combining Eq.1.20 with Eq.1.17 we can get time dependence of the scale factor for different eras dominated by different component:

$$a(t) \propto \begin{cases} t^{2/3(1+w_i)} & w_i = 1/3 \quad t^{1/2} \quad \text{RD}, \quad \text{Early Universe} > \text{z} \gtrsim 3000, \\ & w_i = 0 \quad\;\; t^{2/3} \quad \text{MD}, \quad 3000 \gtrsim \text{z} \gtrsim 0.5, \\ e^{H_0\sqrt{\Omega_\Lambda}t} & w_i = -1 \qquad\;\; \Lambda\text{D}, \quad 0.5 \gtrsim \text{z}. \end{cases} \tag{1.21}$$

RD, MD and ΛD stand for radiation dominated, matter dominated and dark energy dominated areas, which are three periods in the cosmic history (specified by the redshift z) when the specific component dominates the energy density. For each period the scale factor has a different dependence with time, recording the expansion/contraction history of the universe. The indicated redshift intervals in Eq.1.21 are determined by the measured abundances of cosmological components, anticipating the subject of the next Sub-Section.

1.1.4 Cosmological Abundances

A number of cosmological observations determine the observed abundances of cosmological components. Most of these are based on the dynamics and behavior of cosmological perturbations, which are the subject of the next Section. Here we just conclude the current one by quoting the constraints deriving from the *Planck* satellite, which is a full-sky survey with multi-frequency bands to measure CMB and other astrophysical signals, giving observed values as[4] (Planck Collaboration VI, 2020)

$$\begin{aligned} H_0 &= (67.66 \pm 0.42)\text{km/s/Mpc}, \\ \Omega_\Lambda &= 0.6889 \pm 0.0056, \\ \Omega_m &= 0.3111 \pm 0.0056, \\ \Omega_K &= 0.001 \pm 0.002, \\ \Omega_r &= 9.2364 \times 10^{-5}. \end{aligned} \tag{1.22}$$

at 68% confidence level (CL). The matter density can be divided into two components as $\Omega_b h^2 = 0.02233 \pm 0.00015, \Omega_c h^2 = 0.1198 \pm 0.0012$, where b and c stand for baryons and cold dark matter. h is defined via $H_0 = 100h$ for mathematical convenience. The fractional density for radiation is derived using results in (Planck Collaboration VI, 2020), since this

[4] 1Mpc = 10^6pc, where pc is a distance unit in astronomy and short for parsec and 1pc ≈ 3.09×10^{16} m.

paper does not give the estimated values directly, and it is negligible compared to the other abundances at present.

We see that the dominant species are the dark energy and dark matter which consists of around 95% of the total energy density hence the name of ΛCDM model, while the normal matter only contributes to 5%. The contribution from cosmological curvature is zero within errors.

1.2 Linear Perturbations

In this Section we go beyond the assumptions of Homogeneity and Isotropy, describing linear cosmological perturbations.

We separate metric and energy-momentum tensors in background and linear perturbations, depending on both space and time, writing

$$\begin{aligned} g_{\mu\nu}(t,\mathbf{x}) &= \bar{g}_{\mu\nu} + \delta g_{\mu\nu}(t,\mathbf{x}), \\ T_{\mu\nu}(t,\mathbf{x}) &= \bar{T}_{\mu\nu} + \delta T_{\mu\nu}(t,\mathbf{x}), \end{aligned} \tag{1.23}$$

where barred quantities are from the smooth background and terms starting with δ are the perturbations upon the background values.

The assumption of linearity relies on the approximation of evolution equations (Boltzmann, Einstein and conservation equations) to first order in the perturbations, ignoring higher orders and backreaction of the perturbations onto the background. We now proceed to the classification of linear cosmological perturbations, focusing on the quantities which are relevant in this Thesis, and pointing the reader for a full treatment and more details to Baumann (2022); Weinberg (2008); Dodelson & Schmidt (2020).

1.2.1 Scalar-Vector-Tensor decomposition

From now on we define units in which the speed of light is one. We first perturb the FLRW metric (1.9) by a small amount and define

$$\begin{aligned} g_{00}(t,\boldsymbol{x}) &= -1 + h_{00}(t,\boldsymbol{x}), \\ g_{0i}(t,\boldsymbol{x}) &= a(t)h_{0i}(t,\boldsymbol{x}) = a(t)h_{i0}(t,\boldsymbol{x}), \\ g_{ij}(t,\boldsymbol{x}) &= a^2(t)\left[\delta_{ij} + h_{ij}(t,\boldsymbol{x})\right], \end{aligned} \tag{1.24}$$

where h_{00}, h_{0i}, h_{ij} are metric perturbations as functions of space and time to the first order.

It will be useful to perform a scalar-vector-tensor (SVT) decomposition of the perturbations following the **decomposition theorem**, which states that perturbations of each type—scalar, vector, and tensor—behave differently under spatial rotations and evolve independently at linear order. Therefore Einstein equations for scalars, vectors and tensors also do not mix at linear order and can be solved separately. We are most interested in scalar perturbations to the metric since these couple to the density of matter and radiation

and ultimately are responsible for most of the structures we observe in the universe. Vector perturbations are usually associated to rotational velocity fields that are usually not interesting since they decay due to expansion. Tensor fluctuations in the metric, that are, **gravitational waves** (GWs) which distort the spacetime as they pass by, are not coupled to the density and thus are not responsible for the large-scale structure of the universe, but they do induce anisotropies in the CMB which turn out to be a unique signature of processes in the early universe, which is the focus of next Section and next Chapter.

We now discuss how to do perform the SVT decomposition to the perturbations in Eq.1.24. h_{00} in Eq.1.24 is a three-scalar since it does not have a spatial index and remains unchanged under spatial rotations. Therefore we parametrize it with a scalar function

$$h_{00} = -2Z. \tag{1.25}$$

The time-space perturbation $h_{0,i}$ is a 3-vector which can be decomposed into the gradient of a scalar function and a divergence-less vector function

$$h_{0i} = \underbrace{\partial_i A}_{\text{scalar}} + \underbrace{\hat{B}_i}_{\text{vector}} . \tag{1.26}$$

where we define the scalar and vector contributions respectively.

The space-space component, h_{ij}, is a symmetric 3-tensor and be be written as a combination of three parts

$$h_{ij} = \underbrace{C\delta_{ij} + \partial_{\langle i}\partial_{j\rangle} D}_{\text{scalar}} + \underbrace{\partial_{(i}\hat{E}_{j)}}_{\text{vector}} + \underbrace{\hat{H}_{ij}}_{\text{tensor}} , \tag{1.27}$$

where

$$\begin{aligned} \partial_{\langle i}\partial_{j\rangle} D &\equiv \left(\partial_i\partial_j - \frac{1}{3}\delta_{ij}\nabla^2\right) D, \\ \partial_{(i}\hat{E}_{j)} &\equiv \frac{1}{2}\left(\partial_i\hat{E}_j + \partial_j\hat{E}_i\right). \end{aligned} \tag{1.28}$$

The hatted quantities are divergence-less, $\partial^i\hat{B}_i = \partial^i\hat{E}_i = \partial^i\hat{H}_{ij} = 0$ and the tensor perturbations is also traceless, $\hat{H}^i_i = 0$.

Until now, we have identified four scalar functions (Z, A, C, D), two transverse vectors ($\hat{B}$, $\hat{E}$) and one tensor ($\hat{H}$) which in total makes 10 degrees of freedoms (D.O.F.) for the symmetric 4-tensor (one for each scalar, two for each vector with divergence-less constraint, two for the tensor with divergence-less and traceless constraint). In the next Sub-Section we show that not all of them have independent physical meaning, and focus on the relevant degrees of freedom.

1.2.2 Gauge choice

Gauges in cosmology are simply reference frames which are close to the comoving one, so that coordinate shifts contribute to cosmological perturbations at linear level. The simplest example is the h_{00}, i.e. the time shift, which can be set to zero if all observers adopt the same cosmological time as their time coordinate. We do not derive the necessary algebra here, referring to original works (Bardeen, 1980) for a complete treatment. We limit ourselves to define the **gauge-invariant** variables, and the one adopted in the gauge that, historically, have been used most, i.e. the **conformal-Newtonian** one. With this limit we can say that physically independent quantities are two for scalars, one for vectors (which we do not define as we're not focusing on them in this Thesis), while tensors, being unaffected by gauges by construction, are automatically gauge invariant. The most popular choice is the **Bardeen variables** (Bardeen, 1980):

$$\begin{aligned} \Phi_A &\equiv Z + \frac{1}{a}\frac{\partial}{\partial\eta}\left[a\left(A - D'\right)\right], \\ \Phi_H &\equiv -C + \frac{1}{3}\nabla^2 D - aH\left(A - D'\right), \end{aligned} \tag{1.29}$$

where η is the conformal time defined as $\mathrm{d}\eta = \mathrm{d}t/a(t)$ and the prime represents the derivative with respect to η.

In the conformal-Newtonian gauge, where $D = A = 0$, we have $\Phi_A = \Psi$ and $\Phi_H = -\Phi$. Then the *scalar* part of the metric with perturbations in Eq.1.24 reads

$$\begin{aligned} g_{00}(\boldsymbol{x}, t) &= -1 - 2\Psi(\boldsymbol{x}, t), \\ g_{0i}(\boldsymbol{x}, t) &= 0, \\ g_{ij}(\boldsymbol{x}, t) &= a^2(t)\delta_{ij}[1 + 2\Phi(\boldsymbol{x}, t)], \end{aligned} \tag{1.30}$$

where Ψ and Φ are two gauge-invariant variables, the so-called **Bardeen potentials**, representing the two D.O.F for scalar perturbations. They correspond to Newtonian potential and spatial curvature respectively. The *tensor* part of the metric perturbations is gauge-invariant and has the form of

$$g_{ij}(\boldsymbol{x}, t) = a^2(t)[\delta_{ij} + H_{ij}(\boldsymbol{x}, t)], \quad H_{ij} = \begin{pmatrix} h_+ & h_\times & 0 \\ h_\times & -h_+ & 0 \\ 0 & 0 & 0 \end{pmatrix}, \tag{1.31}$$

where h_+ and $h_\times$ are the two components of the divergence-less, traceless, symmetric tensor, which corresponds GWs in GR.

This reasoning is extended similarly to the energy-momentum tensor $T_{\mu\nu}$, which will include perturbations to the density, pressure, velocities and so on (see e.g., Baumann (2022)). One important gauge-invariant variable which is a linear combination of perturbations both in the metric and matter (i.e., all species including radiation), can be defined

as

$$\mathcal{R} \equiv -C + \frac{1}{3}\nabla^2 E - aH(v + A), \tag{1.32}$$

where v is the scalar part of the perturbations to the velocity in the energy-momentum tensor and $\mathcal{R}$ is called **curvature perturbation** since it reduces to the intrinsic curvature of the spatial slices in the comoving gauges. We will see in next Section that $\mathcal{R}$ is useful when describing initial conditions.

1.3 Inflation

In this Section we introduce the most important process concerning the very early universe, which is currently under active investigation in cosmology, responsible for the growth of the initial size of the universe to the present. Since the dynamics corresponds to an initial and transient phase of accelerated expansion, the process is known as Inflation. We will briefly review the problems which Inflation might solve, and then define the inflationary quantities concerning initial conditions for perturbations, which are relevant for this Thesis.

1.3.1 Problems of the pre-inflationary cosmology

Inflation is capable of providing a framework where at least two well-known problems that affect a cosmology based on radiation and matter only. We briefly describe them here and refer to Baumann (2009) for a more detailed description.

- **Horizon problem**. We have a precise measurement of the temperature of the CMB photons which are observed to be nearly isotropic, with the fluctuations at different directions only at the level of 10^{-5}. However the information travels only with a limited speed, which define a causal horizon beyond which there is no way to communicate. After the decoupling, photons travel freely in the universe so the only chance for them to synchronize their temperature is before decoupling, but constrained in the horizon. The horizon at decoupling corresponding to an angular scale of about one degree, which means that photons with separation larger than one degree have no chance to interact and the probability for them to have the same temperature is almost zero, which however happens in our real universe.

- **Flatness problem**. It arises from the observation that the current density of the universe is extremely close to the critical value, or the universe is very close to flat, as we explained in Sec.1.1.2. Given that any deviation of the total density from the critical value would increase rapidly over cosmic time, this implies that the early universe must have been even closer to flatness, with a deviation of one part in 10^{62} or less. Cosmologists are puzzled by how the initial density became so finely tuned to this 'special' value.

The **Inflation** model is a theoretical framework (Guth, 1981; Sato, 1981; Starobinsky, 1982; Linde, 1982; Albrecht & Steinhardt, 1982) proposed to solve these problems, which

describes a quasi-exponential expansion of space in the early universe, thus serving as an modification to the ΛCDM model at early times. The inflationary epoch is believed to have lasted from 10^{-36} seconds to between 10^{-33} and 10^{-32} seconds after the Big Bang, during which the universe expands roughly 27 orders of magnitude. This offers an explanation to the horizon problem: before inflation physical interactions can happen within the horizon at that time, then after inflation the scales are stretched to be much larger than the horizon. At the same time inflation solve the Flatness problem by stretching the universe.

Within the inflation framework, a wide variety of mathematical models have been studied in the literature (for a extremely comprehensive review of inflation models see Martin et al. (2014), see also Baumann (2009)) and in fact many of them can fit the observations.

The simplest and most popular ones are the **single-field slow-roll** inflation (Linde, 1982; Albrecht & Steinhardt, 1982), based on the assumption that inflation is driven by a single scalar field, ϕ, slowly rolling down a potential well toward its true ground state, although such kind of scalar field is unknown. We typically define two **slow-roll parameters** to quantify slow roll, ϵ_{sr} and δ_{sr}, although different forms exist. Inflation ends when the scalar field reaches the potential minimum and and no longer slowly rolling. At this point, the field has significant kinetic energy so it oscillates around the minimum then finally the scalar field decays into lighter particles, which eventually leads to a homogeneous, radiation-dominated universe. All the discussions below are within the framework of single-field slow-roll inflation models.

Besides providing a solution to the above problems, after its initial proposal, inflation was soon realized to be able to provide a natural mechanism for generating the perturbations which are the seeds for the formation of the cosmological structures (Bardeen et al., 1983). Within inflation theory, quantum fluctuations are first generated in the very early Universe when the relevant scales are causally connected. Then they are stretched outside the horizon by inflation and are frozen all the way to the moment when they re-enter the horizon and finally serve as initial conditions for the growth of structures in the universe. As we discussed in the Section 1.2.1, the most significant kinds of perturbations produced during inflation are scalar and tensor ones because their dynamics allows them to be observable at the present epoch.

1.3.2 Fourier transform and power spectra

In cosmology, we always focus on the statistical properties of the observables since all the theories can only predict the ensemble average of a physical quantity. The choice is the **power spectrum**—the two-point correlation in Fourier space. Mathematically, we enter into the Fourier space with a Fourier transform

$$f(t, \boldsymbol{k}) \equiv \int \mathrm{d}^3 x f(t, \boldsymbol{x}) e^{-i\boldsymbol{k}\cdot\boldsymbol{x}}, \tag{1.33}$$

with the advantage that different k modes evolve independently in linear theories, where k corresponds to a physical wavelength of $\lambda = 2\pi/k$. Statistical homogeneity, which means translation invariance, implies that power spectrum is nonzero only if two scales considered $\mathbf{k}$ and $\mathbf{k}'$ have $\mathbf{k} = \mathbf{k}'$. Further assuming statistical isotropy which means rotational invariance, we can reduce the dependence of the power spectrum of $\mathbf{k}$ to k, where $k = |\mathbf{k}|$. Therefore the power spectrum can be defined as

$$\left\langle f(\mathbf{k}) f\left(\mathbf{k}'\right)^* \right\rangle = (2\pi)^3 \delta^3\left(\mathbf{k} - \mathbf{k}'\right) P(k), \tag{1.34}$$

where <> is the ensemble average of different realizations of the field. δ^3 is the Dirac delta function which constrains $\mathbf{k} = \mathbf{k}'$. Physically speaking, the amplitude of $P(k)$ offers a measurement of the possibility to find two particles (galaxy, photon, ...) at the characteristic distance $\lambda = 2\pi/k$, i.e., the particles are more likely to cluster at the distance of λ. Thus $P(k)$ provides a quantitative way to describe the distribution of the particles in a field.

1.3.3 Scalar perturbations

In principle, we should specify the initial density and velocity perturbations for each kind of species. However in single-field inflation theories all known particles derive from the decay of a single entity, the inflation scalar field, which generates **adiabatic** perturbations: the fractional density perturbations are the same for all species,

$$\frac{\delta\rho_s}{\rho_s} = \frac{\delta\rho}{\rho}. \tag{1.35}$$

Using Einstein field equations, it is sufficient to specify the initial conditions in terms of Ψ defined in Eq.1.30, then derive the perturbations for all species from Ψ.

We have defined the gauge-invariant curvature perturbation $\mathcal{R}$ in Equation 1.32. A critical feature of this variable is that it is conserved when the perturbations moves outside the horizon, transferring the perturbations in the scalar field ϕ during inflation to the perturbations in the Bardeen potentials Ψ and Φ.

The scalar perturbations generated during inflation are commonly parameterized in terms of the power spectrum of $\mathcal{R}$:

$$P_{\mathcal{R}}(k) \equiv 2\pi^2 \mathcal{A}_s k^{-3} \left(\frac{k}{k_p}\right)^{n_s - 1}, \quad \Delta^2_{\mathcal{R}}(k) \equiv \frac{k^3}{2\pi^2} P_{\mathcal{R}}(k) = \mathcal{A}_s \left(\frac{k}{k_p}\right)^{n_s - 1}, \tag{1.36}$$

where $\mathcal{A}_s$ is the power spectrum amplitude of scalar fluctuations at the pivot scale k_p, which is determined as the scale best constrained by the particular experiment (e.g., for CMB observations the *Planck* team adopts $k_p = 0.05\text{Mpc}^{-1}$), and n_s is the scalar power spectral index. We also introduce the **dimensionless power spectrum**, $\Delta^2_{\mathcal{R}}$, which gives the variance in a logarithmic wavenumber interval. Both $\mathcal{A}_s$ and n_s are related to the slow-roll parameters in the inflation models.

Before inflation was proposed, in 1970s, it was argued by Harrison, Zel'dovich and Peebles that the initial perturbations of our universe are likely to have taken a power law form with spectral index $n_s \sim 1$ (Harrison, 1970; Zeldovich, 1972; Peebles & Yu, 1970), which means that $\Delta^2_{\mathcal{R}}(k)$ is **scale-invariant** from Equation 1.36. It is now called the Harrison-Zel'dovich-Peebles spectrum for $n_s = 1$. Inflation also predicts the n_s to be close to but *not equal to* 1. The phenomenology behind this occurrence is simple. Since each perturbation at a given wavenumber k exits the horizon at different times during inflation, it records the different dynamics in the inflationary process. Since the inflation had to slow down reaching the minimum of the potential modes with smaller wavelengths, i.e. larger ks, recorded a smaller expansion rate, and therefore, a smaller perturbation, making the spectrum tilted towards n_s less than 1. Constraints from CMB experiments of these two parameters are $\mathcal{A}_s = (2.098 \pm 0.023) \times 10^{-9}$ and $n_s = 0.965 \pm 0.004$ (at $k_p = 0.05\text{Mpc}^{-1}$, Planck Collaboration VI (2020)). The observed percent-level difference from the Harrison-Zel'dovich-Peebles spectrum is precisely what is expected for fluctuations generated by inflation.

1.3.4 Tensor perturbations

The most intriguing and robust prediction of inflation is a stochastic background of GWs, or the tensor metric perturbations, $\delta g_{ij} = a^2 H_{ij}$. These tensor modes from inflation are called **Primordial Gravitational Waves (PGW)** since there are astrophysical processes in the late universe like the merging of compact objects which can also produce GWs. Similar to the curvature perturbations $\mathcal{R}$, we can define power spectrum of H_{ij} as

$$P_H(k) \equiv 2\pi^2 \mathcal{A}_T k^{-3} \left(\frac{k}{k_\mathrm{p}}\right)^{n_\mathrm{T}}, \quad \Delta^2_H(k) \equiv \frac{k^3}{2\pi^2} P_H(k) = \mathcal{A}_T \left(\frac{k}{k_p}\right)^{n_T - 1}, \tag{1.37}$$

with the amplitude $\mathcal{A}_T$ and the spectral index n_T defined for tensor perturbations. $n_T = 0$ corresponds to a scale-invariant tensor power spectrum (which is different for the case of scalar perturbations with $n_s = 1$, for convention). In practice, the tensor amplitude is usually expressed in terms of **tensor-to-scalar ratio** r:

$$r(k) \equiv \frac{P_T(k)}{P_{\mathcal{R}}(k)} \overset{k=k_p}{=} \frac{\mathcal{A}_T}{\mathcal{A}_s}, \tag{1.38}$$

which is also depending on the slow-roll parameters, especially sensitively on the energy scale of inflation. Various inflation models have different predictions for r, and therefore, even in case of a non-detection of PGWs, the latter occurrence will provide insight into the inflationary process. The best constraints for r comes from the observations of CMB polarization data, which will be our topic for next chapter, reaching at the upper limit $r < 0.032$ (Tristram et al., 2022), at a 95% confidence level, which is still within the predictions of a few popular slow-roll models.

In the following chapter we will describe how the scalar and tensor perturbations generated during inflation leave their imprints on the distribution of CMB photons, especially

to the CMB temperature and polarization power spectra. These perturbations will definitely have similar effects to the distribution to the matter field (including normal and dark matter) and for those we refer the interested readers to any cosmology book (eg. Dodelson & Schmidt (2020); Baumann (2022)).

1.3.5 Primordial Non-Gaussianity

Before concluding this Chapter, we briefly mention the area of research concerning deviations of the inflationary perturbations from a pure Gaussian field, i.e. the description and quantification of the PNG.

Even in the simplest inflationary models, involving a single slowly rolling scalar field, a small and yet calculable amount of non-Gaussianity[5] is predicted (Maldacena, 2003). On the other hand, a wide range of inflationary models, based on varying assumptions about the nature of scalar field(s), can produce significant PNG (Lyth et al., 2003; Bartolo et al., 2004). A robust detection or strong constraints on PNG can distinguish between competing mechanisms responsible for generating cosmological perturbations in the early Universe. Different inflationary scenarios predict distinct amplitudes, shapes, and scale dependencies of non-Gaussianity. Consequently, PNG provides complementary information to the scalar spectral index of curvature perturbations and the tensor-to-scalar ratio, helping to differentiate between inflationary models (Komatsu, 2010).

A way to phenomenologically parametrize the level of non-Gaussianity in the cosmological perturbations is to introduce a non-linearity parameter $f_{\rm NL}$ through Bardeen's gravitational potential defined in Eq.1.30 (e.g., Komatsu & Spergel, 2001), writing

$$\Phi(\mathbf{x}) = \Phi_{\rm L}(\mathbf{x}) + f_{\rm NL}\left(\Phi_{\rm L}^2(\mathbf{x}) - \left\langle\Phi_{\rm L}^2(\mathbf{x})\right\rangle\right) , \tag{1.39}$$

where $\Phi_{\rm L}(\mathbf{x})$ denotes the linear Gaussian part of the perturbation. $f_{\rm NL}$ quantifies the strength of the PNG signal, and therefore is considered one of the cosmological parameters which is suited to distinguish various inflationary models (Planck Collaboration IX, 2020).

Mathematically speaking, if the primordial fluctuations follow a Gaussian distribution, they are fully described by their two-point correlation function, or equivalently, their power spectrum (Coil, 2013). However, if the fluctuations are non-Gaussian, higher-order correlation functions contain additional statistical information that the two-point correlation function cannot capture. Specifically, the three-point correlation function, or its Fourier transform known as the bispectrum, is particularly important as it is the lowest-order statistic capable of differentiating between Gaussian and non-Gaussian perturbations. The primordial bispectrum is defined by:

$$\langle\Phi\left(\boldsymbol{k}_1\right)\Phi\left(\boldsymbol{k}_2\right)\Phi\left(\boldsymbol{k}_3\right)\rangle = (2\pi)^3\delta^{(3)}\left(\boldsymbol{k}_1+\boldsymbol{k}_2+\boldsymbol{k}_3\right)B_\Phi\left(k_1,k_2,k_3\right) . \tag{1.40}$$

The bispectrum $B_\Phi\left(k_1,k_2,k_3\right)$ samples triangles formed by the three wave-vectors in the Fourier space. The shapes of the triangles encode information about the physical mech-

[5] Any deviation from a Gaussian distribution is called non-Gaussianity.

anisms that can generate such non-Gaussian fingerprints in the early Universe. Different types of non-Gaussianity are defined for the following distinct configurations of the k-modes involved (Planck Collaboration XXIV, 2014).

- Local. This is characterized by a signal that is maximal for squeezed triangles with $k_1 \ll k_2 \simeq k_3$ (or permutations) and in general occurs when PNG is generated on very large scales .
- Equilateral. This peaks for a equilateral triangle with $k_1 \approx k_2 \approx k_3$.
- Folded. This is due to enhanced correlation for $k_1 + k_2 \approx k_3$.

As a valuable complement to the bispectrum, Minkowski Functionals (Hadwiger, 1957; Hikage et al., 2006) work in real space which makes them useful to handle complexities in the analysis, such as masks. They are also used to describe the properties of signals which are markedly non-Gaussian, such as the diffuse Galactic emissions, which will be subject of the following Chapters. Other statistical methods for measuring non-Gaussianity include wavelet scattering transform (Regaldo-Saint Blancard et al., 2020; Delouis et al., 2022; Mousset et al., 2024) and skewness and kurtosis (Ben-David et al., 2015).

Non-Gaussian information in the initial conditions is transferred to observable quantities such as CMB anisotropies that we are going to introduce in the next Chapter, making the CMB an excellent tracer of PNG (Komatsu, 2002; Planck Collaboration IX, 2020), also incorporating non-linear mechanisms, such as gravitational lensing from large scale structure, which also induce a deviation from a pure Gaussian field. Indeed, in the rest of the Thesis, when discussing non-Gaussianity, we shall focus on the latter effect from the point of view of CMB anisotropies, and the diffuse Galactic emissions, which, as we shall see in Chapter 3, are markedly non-Gaussian.

2

Cosmic Microwave Background

Let the universe shine for us!

In the previous Chapter, we have introduced the basic properties of ΛCDM cosmology. Here we focus on CMB, which is constituted by photons decoupled from electrons at the end of the recombination, which happened approximately 380000 years after the Big Bang ($z \approx 1100$, with a thickness of about $\Delta z = 90$), as we discussed in the previous Chapter. The spacetime region of the recombination is known as Last Scattering Surface (LSS) and carries the oldest record of cosmic structure via electro-magnetic radiation, when the matter dominated era in cosmology have already started (Eq.1.21).

We are interested in the angular distribution of the properties of CMB photons, both total intensity and polarization, i.e., the **anisotropies**, as a function of the line of sight ($\hat{\mathbf{n}}$). The average temperature of CMB is about $\bar{T} = 2.7$K with the fluctuations $\sigma(T)$ at the level of 10^{-5}, which we indicate as $\delta T(\hat{\mathbf{n}})/\bar{T}$. Anisotropies in the linear polarization are a few percent of these, as we shall wee.

The anisotropies we see today have two main contributions, an *intrinsic* component originated in the LSS and another one due to perturbative effects collected along the line of sight to us, writing here just total intensity for simplicity, as

$$\left.\frac{\delta T}{\bar{T}}\right|_{\text{today},0} = \left.\frac{\delta T}{\bar{T}}\right|_{\text{LSS},*} + \left.\frac{\delta T}{\bar{T}}\right|_{\text{journey},\sim}, \tag{2.1}$$

and hereafter we will use 0, * and $\sim$ to represent today, LSS (recombination) and the time

during the journey to us, respectively.

In Sec.2.2, after the definition of the statistics of interest in Sec.2.1, we will give an overview of the physics of CMB, explaining the two terms in the right hand side of Eq.2.1. In Sec.2.3, we shall focus on the linear polarization of CMB photons, which, thank to the anisotropic response of the electro-magnetic scatter, is able to record local inhomogeneities through the linear polarization of the outgoing CMB photon. Moreover, in Sec.2.4, we will have a review of the achievements of current and past observations, and the science goals of future ones.

The purpose of the content in this Chapter is to give a phenomenological overview of CMB physics, along the main relevant equations describing this cosmological constituent. For a full description, we refer the readers to pedagogical reviews and books on CMB, e.g., Hu & Dodelson (2002); Hu & White (1997) and Dodelson & Schmidt (2020).

2.1 Angular power spectrum for total intensity anisotropies

In this Section we define the angular decomposition of CMB anisotropies, focusing on total intensity, leaving the part concerning polarization to Sec.2.3.

Analogously to the Fourier transformation (Eq.1.33) for fields in three-dimensional space, we can apply the spherical harmonic transformation to the CMB temperature perturbations on a two-dimensional sphere. This allows us to decompose the perturbations into a linear combination of harmonic functions across different angular scales, writing

$$\Theta(\hat{\mathbf{n}},t) \equiv \frac{\delta T}{\bar{T}}(\hat{\mathbf{n}},t) = \sum_{l=1}^{\infty}\sum_{m=-l}^{l} a_{lm}(t)Y_{lm}(\hat{\mathbf{n}}),$$
$$a_{lm}^{T}(t) = \int d\Omega Y_{lm}^{\star}(\hat{\mathbf{n}})\Theta(\hat{\mathbf{n}},t)\,,$$

where T stands for temperature and we rename $\Theta(\mathbf{n}) \equiv \frac{\delta T}{\bar{T}}(\hat{\mathbf{n}})$. The subscripts ℓ, m are conjugate to the real-space direction vector $\hat{\mathbf{n}}$, just like the variable $\boldsymbol{k}$ is conjugate to the three-dimensional position $\boldsymbol{x}$ in Eq.1.33. The coefficients ℓ and m mark the angular scale of the expansion. In particular, ℓ describes the equivalent of the wavelength in the Fourier space, being related to the typical scale of variation in the angular domain as ℓ approximately $180/\ell$ degrees, while m varies from $-\ell$ to ℓ, denoting different angular distributions at that scale. The complete set of eigenfunctions is $Y_{lm}(\hat{\mathbf{n}})$, while the complete set of eigenfunctions for the 3D Fourier transform is $e^{i\boldsymbol{k}\cdot\boldsymbol{x}}$. All of the information encoded in the temperature field is also contained in the (x,t)-dependent amplitudes a_{lm}s.

Similar to density perturbations, theories cannot predict the individual value of a_{lm} but can only make statistical predictions. In the same way as the definition of power spectrum for the 3-D field in Eq.1.34, we can also define the variance of perturbations for each $\ell-$mode as **angular power spectrum**

$$\left\langle a^T_{lm} a^{T*}_{l'm'} \right\rangle = \delta_{ll'} \delta_{mm'} C_l^{TT} \,, \tag{2.2}$$

where <> is the ensemble average of different realizations of a_{lm}s. There is no m-dependence due to rotational invariance. We have access to only one realization of CMB for observations, which is the one in our Universe. Thus for a given ℓ, there are $2\ell+1$ a_{lm}s with m varying, from which we can have an estimation of C_ℓ as

$$\hat{C}_l^{\,TT} = \frac{1}{2l+1} \sum_m a_{lm} a^*_{l'm'} \,, \tag{2.3}$$

where $\hat{C}_l^{\,TT}$ is our estimator for the theoretical C_ℓ^{TT}. Therefore there is an intrinsic uncertainty in the estimation of C_ℓ^{TT} from the observed CMB temperature map, just like estimating the variances from its limited samples, which is the well-known **cosmic variance** (Gawiser & Silk, 2000) and reads

$$\left(\frac{\Delta C_l^{TT}}{C_l^{TT}} \right)_{\text{cosmic variance}} = \sqrt{\frac{2}{2l+1}} \,. \tag{2.4}$$

As expected, the uncertainty is proportional to the inverse of the square root of the number of samples and restrict our ability to measure the properties with infinite precision. This uncertainty decreases for small scales (large ℓ) and the large variance at small ℓ makes large scales difficult to measure.

The angular power spectra C_ℓs encode all the statistical information of a Gaussian field, which is the case for the fluctuations in the temperature of CMB photons, if we assume perfect Gaussianity in the inflationary perturbations and this is the case according to the measurements from *Planck* (Planck Collaboration IX, 2020).

Before concluding this Section, we wish to introduce a basic phenomenological quantity in cosmology, corresponding to the cosmological effective horizon, or, in the common jargon of cosmologists, horizon. In the previous Chapter we introduced the concept of causal horizon, namely the ones associated to pure geometry, without any other interaction. The effective horizon, corresponding to a typical distance where interactions can occur, is another quantity, corresponding to the inverse of the Hubble expansion rate, H^{-1}. No quantitative demonstration of this statement exists, but its validity can be understood by looking at the evolution equations in cosmology, where the spacetime dynamics of background and perturbations is set by the Hubble expansion rate.

Perturbations obey just the dynamics caused by expansion on super-horizon scale, i.e. $k \ll aH$, while they can interact and modify their shape if they are on sub-horizon scales, i.e. k comparable or $\gg$ with respect to aH. The moment in which their scale is comparable to the horizon, $k = aH$, is called horizon crossing. For CMB anisotropies, since ℓ marks scales on the LSS, i.e. their coefficients on $l \ll l_H$, where the latter is the multiple corresponding to the angle subtended by the horizon at the LSS, are on super-horizon

scales; while, vice versa, anisotropies at $l \gg l_H$ record perturbations on sub-horizon scales. The value of l_H, determined by cosmological abundances, expansion, etc., is approximately 200, i.e. one degree on the sky.

2.2 Observed CMB temperature power spectra

The main sources of anisotropies on the LSS due to the actual distribution of photons are represented by density and velocity of the photon-electron system undergoing the scattering towards observations. The first one simply descends from the Bose-Einstein statistics and the Stephen-Boltzmann law, $\rho_\gamma \propto T^4$, meaning that denser zones are also hotter, and vice-versa. The second one is just a Doppler effect caused by peculiar velocity of the scatterer along the line of sight. These two effects have the form

$$\left.\frac{\delta T}{\bar{T}}\right|_* = \left(\frac{1}{4}\delta_\gamma - \hat{\mathbf{n}}\cdot\mathbf{v}_e\right)_* , \tag{2.5}$$

where δ_γ is the energy density contrast defined as $(\rho_\gamma - \bar{\rho_\gamma})/\bar{\rho_\gamma}$, $\hat{\mathbf{n}}$ is the direction of our observation and $\mathbf{v}_e$ is the bulk velocity of the electrons.

After recombination, the photons travel through the inhomogeneous universe and gain (blueshift) or lose energy (redshift) when they fall in or climb out the gravitational potential wells from evolving structures along the path (which is a null geodesic), which do imprint anisotropies if the energy loss or gain when crossing an evolving structure do not balance. Therefore the fluctuations from the time of recombination to now is an integration of the gravitational redshift effect. Using geodesic equation and the metric (with scalar type perturbations) in Eq.1.30, we can have the form of δT during the free streaming of photons, which can be written as

$$\begin{aligned}\left.\frac{\delta T}{\bar{T}}\right|_\sim &= -\int_{t_*}^{t_0} \mathrm{d}\Psi + \int_{t_*}^{t_0}\left(\dot{\Psi}+\dot{\Phi}\right)\,\mathrm{d}t \\ &= \Psi_* + \int_{t_*}^{t_0}\left(\dot{\Psi}+\dot{\Phi}\right)\,\mathrm{d}t\,,\end{aligned} \tag{2.6}$$

where Ψ and Φ are the Bardeen potentials defined in last Chapter and we ignore the Ψ_0 term since it is the same for all the photons observed by us thus only contributes to overall shift, not the anisotropies.

By combining the two equations above, we derive the anisotropies of the CMB photons that can be observed today as:

$$\Theta(\mathbf{n})\Big|_0 = \underbrace{\left(\frac{1}{4}\delta_\gamma + \Psi\right)_*}_{\text{SW}} - \underbrace{\left(\hat{\mathbf{n}}\cdot\mathbf{v}_b\right)_*}_{\text{Doppler effect}} + \underbrace{\int_{t_*}^{t_0}\mathrm{d}t\left(\dot{\Psi}+\dot{\Phi}\right)}_{\text{ISW}} . \tag{2.7}$$

The latter can be separated into the following three contributions.

- **Sachs-Wolfe term** (Sachs & Wolfe, 1967). It combines the intrinsic temperature fluctuations coming from the density fluctuations of photons with the induced one from the gravitational redshift at the time of recombination.
- **Doppler term**. The Doppler effect from the electrons bulk velocity, as we have mentioned above.
- **ISW**. It describes additional gravitational redshift due to the evolution of potential in the universe that photons travel through, which would disappear if the potential is constant. From Eq.1.21, we know that for most of the history the universe was matter-dominated and the potential was indeed constant. But at early times, the residual radiation made it varying and contributed to the **early ISW effect**. At late times, dark energy comes into existence, causing Φ to evolve again and leads to the **late ISW effect**.

The physical quantities, δ_γ, Ψ, Φ and the associated derivatives in Eq.2.7 all depend on the initial conditions set by inflation and some approximations can be made at different scales to make the equations of these variables easier to solve. We refer to Dodelson & Schmidt (2020) for a complete treatment and only present the qualitative results here.

At large scales, i.e., at low ℓ multipoles, where $\ell \ll \ell_H$, the fluctuations of CMB photons were created by the super-horizon perturbations at recombination and Eq.2.7 becomes

$$\Theta(\mathbf{n}) \approx \left(\frac{1}{4}\delta_\gamma + \Psi\right)_* , \tag{2.8}$$

which is the SW effect. From adiabatic conditions (Eq.1.35) which is valid for super-horizon scales, we can relate δ_γ to matter perturbations. In this hypothesis that the power spectra are scale-invariant along with the primordial scalar power spectrum, $\Delta_\mathcal{R}$, it can be shown (Dodelson & Schmidt, 2020) that the CMB power spectra take the approximate and simple form

$$\frac{l(l+1)}{2\pi} C_l^{\mathrm{SW}} = \frac{A_\mathrm{s}}{25} , \tag{2.9}$$

where A_s is amplitude defined in Eq.1.36.

For scales with $\ell \gg \ell_H$, which are sub-horizon at decoupling, The approximations adopted so far are not valid, as effects from the radiation pressure cannot be neglected in the **photon-baryon fluid**, where photons are **tightly coupled** to electrons and protons. The over or under density in the cosmological constituents cause gravitational inflow or outflows of CMB photons, which is counterbalanced by radiation pressure, causing oscillations which, in CMB physics, are normally known as **acoustic oscillations**. Peaks and

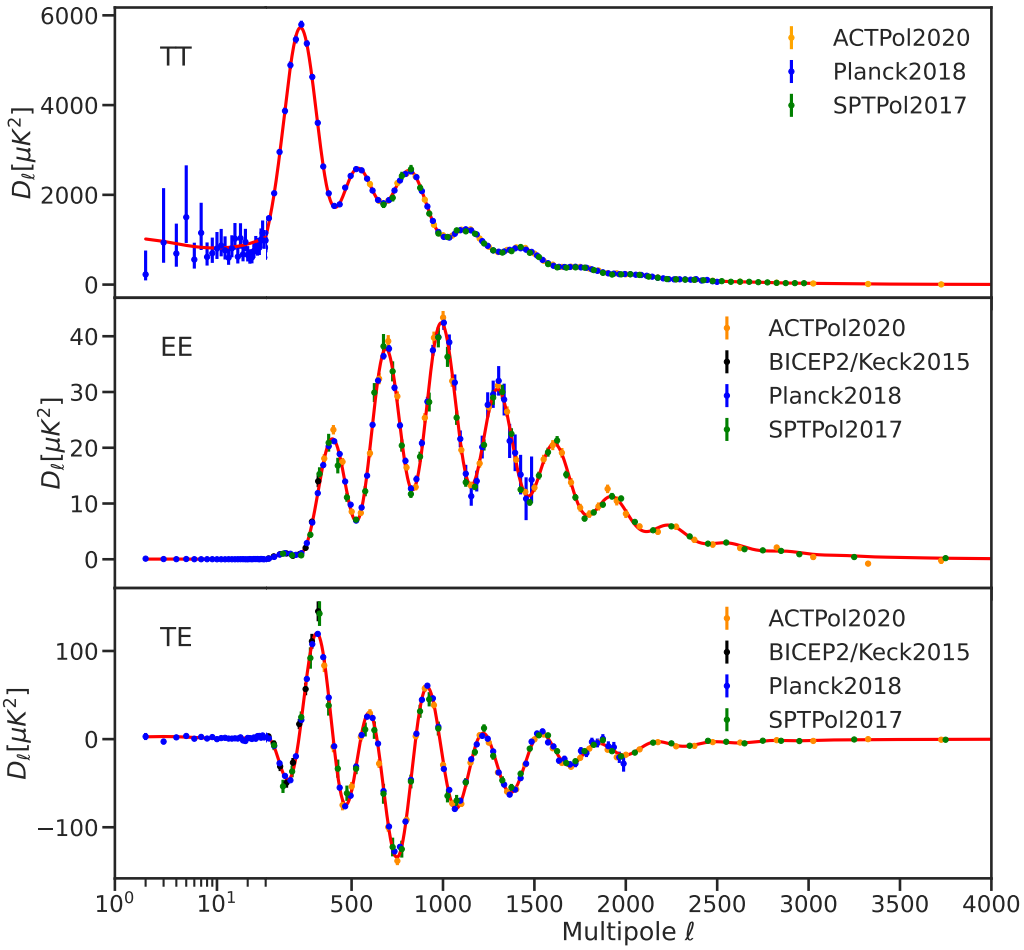

Figure 2.1: CMB TT, EE and TE power spectra. Solid red lines are the theoretical predictions from ΛCDM model assuming *Planck* 2018 cosmology (Planck Collaboration VI, 2020). Blues dots are the results for the bandpower of *Planck* 2018, while other data points are results from experiments showing in the legends. Notice at small multipoles ($\ell < 30$) x-axis are shown in logarithmic scale while at large multipoles ($\ell > 30$) in linear scale. All the data points come from the NASA Lambda website[1], including ACTPol (Choi et al., 2020), SPTPol (Henning et al., 2018), BICEP2/Keck (BICEP2 Collaboration et al., 2016).

valleys in the overall distributions of them, projected onto the LSS, give rise to an oscillatory pattern in CMB anisotropies, at predictable multipoles given the initial conditions and the adiabaticity assumption (Dodelson & Schmidt, 2020).

As it is intuitive, the corresponding pattern also imprints on baryons and creates characteristic scales at which the galaxies have a high correlation. This feature is known as **baryon acoustic oscillations** (BAO, Bassett & Hlozek, 2010) and manifests itself into the power spectrum of density perturbations at later times.

Finally, on smaller angular scales, two separate effects contribute to the cut-off of anisotropies. One is represented by the diffusion, or Silk, damping (Silk, 1968), simply caused by the diffusion of radiation spending more time on sub-horizon regime. The second, and more severe one, is caused by the thickness of the LSS, which prevents to distinguish details on angular scales smaller than the one it subtends in the sky.

In the upper panel of Fig. 2.1, the best-fit CMB total intensity spectrum in solid red line from the ΛCDM cosmology, along with the data in points from the quoted experiments, is shown. Given a cosmology, the theoretical CMB power spectra can be calculated by the standard numerical Boltzmann solvers, such as CAMB[2] (Lewis et al., 2000; Lewis & Bridle, 2002) and CLASS[3] (Lesgourgues, 2011). The predicted spectra then can be utilized to fit the cosmological parameters through the comparison with observations. Being extremely close to each other, the predicted and observed power spectra both present the features we discussed, the large scale SW plateau, the acoustic oscillations, and the damping. Also, the error bars well represent the achieved precision on these measurements, becoming larger on large scales due to the cosmic variance.

Primary anisotropies are the ones generated by effects on the LSS. The ISW is therefore the first example of secondary anisotropy, as it is injected on the CMB along the line of sight. Before concluding this Section, we describe two more examples of important sources of secondary CMB anisotropies acting, in particular, on CMB total intensity. For a complete treatment, we refer to Hu & Dodelson (2002).

As we mentioned previously, light from forming structure sets the end of the Dark Ages, and hits the inter-galactic medium, causing a fraction of electrons to be set free again. This happens around z=6. The electrons could scatter with the photons again during their propagation, partially smearing out the structure of primary anisotropies. The magnitude of this effect is set by the optical depth τ_{rei}, which is an integration of the evolution of the free electron density from reionization to today. It can be shown that the primordial anisotropies produced at $z \approx 1100$ are suppressed by a factor of $e^{-2\tau_{rei}}$, approximately, due to reionization. The optical depth is much less than 1 ($\tau_{rei} = 0.058$ from latest *Planck* results (Tristram et al., 2024), thus roughly 6% of CMB photons were re-scattered at the reionization epoch), due to the overall reionization efficiency, and therefore the

[1] https://lambda.gsfc.nasa.gov/education/lambda_graphics/cmb_power_spectra.html
[2] http://camb.info
[3] https://lesgourg.github.io/class_public/class.html

effect, although very important and measured with high precision, does not alter primary anisotropies substantially. What's more, this scattering only affects those perturbations within the horizon at the time of reionization, i.e., large multipoles, leaving the very large scales unaffected. Reionization brings more prominent features to the spectra of CMB polarization, as we will see in the next Section.

CMB lensing is caused by deflection of photons caused by geodesics deviation around evolving cosmological structures along the line of sight. It results in a blurring of total intensity CMB anisotropies on scales where the deflection is relevant. It can be shown that the typical rms of gravitational lensing deviations on CMB photons is about 2 arcminutes for typical ΛCDM cosmology, so that, also in this case, the modification to primary anisotropies is not substantial. Also, in this case, the most prominent features of gravitational lensing are on the CMB polarization anisotropies, which is the subject of the next Section. For more details on CMB lensing, we refer the reader to (Hu, 2000).

2.3 CMB polarization

Due to the anisotropic properties of the Thomson scattering, an incident quadrupolar distribution in the intensity surrounding a last scatterer particle is recorded as linear polarization in the outgoing wave, as shown in Fig. 2.2.

The polarization of the any electromagnetic wave can be fully described by the **Stokes parameters** (Rybicki & Lightman, 1985)

$$\begin{aligned} I &= E_x^2 + E_y^2 \,, \\ Q &= E_x^2 - E_y^2 \,, \\ U &= 2E_x E_y \cos\left(\phi_x - \phi_y\right) \,, \\ V &= 2E_x E_y \sin\left(\phi_x - \phi_y\right) 1 \,. \end{aligned} \tag{2.10}$$

where E_x and E_y are the amplitudes along x- and y- axis for the electric field and ϕ_x and ϕ_y are the initial phase angles. I measures the total intensity of the radiation, while Q, U describe its linear polarization and V is related to circular polarization. Eq.2.10 describes a fully polarized radiation with $I^2 = Q^2 + U^2 + V^2$, and corresponds, for the CMB blackbody, to the total flux of radiation, parameterized by its temperature. As it is well known, the scattering process in Fig. 2.2 is incapable of generating circular polarization, and therefore we neglect V in the following.

From Eq.2.10 we see that Q parameter is the difference between the intensity along the x-axis and that along the y-axis, while U is the difference between the intensity along x'-axis and y'-axis, where x' and y' are rotated clockwise by 45° with respect to the original x- and y-axis. It can be shown that the Stokes parameters, under rotation of the x- and y-axis by an angle ϕ transform like

$$Q' \pm iU' = e^{\mp 2i\phi}(Q \pm iU) \,. \tag{2.11}$$

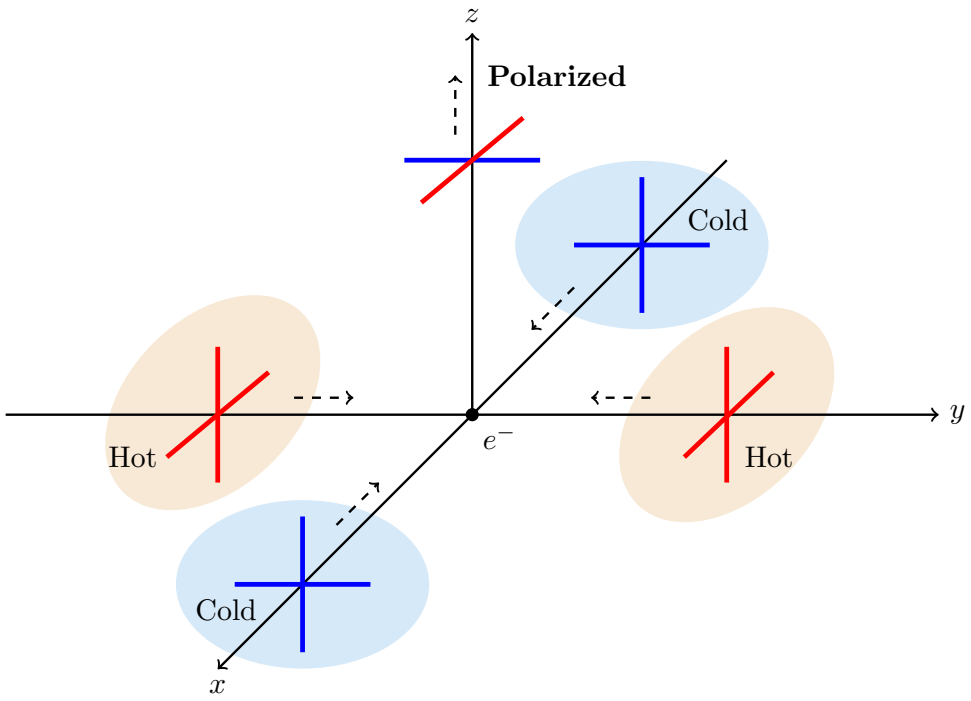

Figure 2.2: Generation of CMB polarization from the Compton scattering with a quadrupole photon distribution. Lines depict the intensity of photons along different axes and hot clouds are shown in red, cold in blue. The dashed arrows represent the directions of the propagation of photons. The solid black dot in the center is the electron. Figure has been adapted from Dodelson & Schmidt (2020).

Q and U are explicitly coordinate dependent. In cosmology it is convenient to adopt another basis, which is the subject of the next Sub-Section.

2.3.1 E-B decomposition

The expansion in the angular domain of the quantity defined above needs to be performed using spin 2 tensor spherical harmonics, due to the tensor nature of CMB polarization:

$$(Q \pm iU)(\hat{n}) = \sum_{lm} a_{\pm 2,lm} \; {}_{\pm 2}Y_{lm}(\hat{\mathbf{n}}) \,. \tag{2.12}$$

It is convenient to decompose the polarization field in two components, even and odd with respect to parity, corresponding to the gradient (E) and curl (B) mode of a tensor field (Zaldarriaga & Seljak, 1997; Kamionkowski et al., 1997). The latter can be re-arranged in maps as follows

$$E(\hat{\mathbf{n}}) = \sum_{lm} a_{E,lm} Y_{lm}(\hat{\mathbf{n}}), \quad B(\hat{\mathbf{n}}) \;\; = \sum_{lm} a_{B,lm} Y_{lm}(\hat{\mathbf{n}}) \,, \tag{2.13}$$

where $a_{E,lm}$ and $a_{B,lm}$ are the multipole coefficients of the E- and B-modes and can be defined from linear combinations of the harmonic coefficients in Eq.2.12,

$$a^E_{\ell m} \equiv -\frac{1}{2}[a_{2,\ell m} + a_{-2,\ell m}], \quad a^B_{\ell m} \equiv -\frac{1}{2i}[a_{2,\ell m} - a_{-2,\ell m}] \,. \tag{2.14}$$

It can be shown that the E and B-modes couple differently, because of their geometrical properties, to cosmological perturbations defined in the previous Chapter (Hu & White, 1997). Specifically, the E modes are excited by all kinds of cosmological perturbations, while B modes are excited only by vector and tensor modes. Since vector modes are damped by the cosmological expansion, as we already mentioned, the B modes would be then a proof of the existence of cosmological gravitational waves produced during inflation.

Similar to the definition of C_l^{TT} we can also have power spectrum for the polarization signal, written as

$$\left\langle a^X_{lm} a^{Y*}_{l'm'} \right\rangle = \delta_{ll'} \delta_{mm'} C_l^{XY} \,, \tag{2.15}$$

where X, Y can be T, E, B modes.

2.3.2 Observed EE and TE power spectra

In the middle and bottom panels of Fig. 2.1, we show the power spectra for EE and TE, respectively, also presenting best-fit and observed ones simultaneously.

We can identify several distinct features in EE spectrum compared with TT one. First, due to the facts that polarization is sourced by CMB quadrupole and the quadrupole is suppressed before recombination due to Compton scattering, the amplitude of polarization spectra is smaller than that of total intensity. Second, like with temperature, the polarization C_ℓs also exhibit a series of acoustic peaks because the quadrupole in the fluid also

undergoes acoustic oscillations. More quantitatively, EE power spectrum has peaks that are out of phase with those in the TT spectrum since in the tight-coupling approximation the quadrupole is related to the dipole, which is out of phase with the monopole, which is the dominant contribution to the TT spectrum. Finally, the dipole is less affected by photon diffusion so that the EE spectrum is less damped at small scales.

The TE spectrum combined and closely follows the feature of T and E-modes, following the correlation between density and velocity perturbations on the LSS. It can be both positive and negative, and is of larger amplitude than the EE signal.

Although not visible in Fig. 2.1, which is plotted in linear scale, a power in EE, TE power spectra at $\ell < 10$ is caused by cosmic reionization, i.e. the boost of anisotropies due to re-scattering of CMB photons onto the population of free electrons generated by the occurrence of electro-magnetic processes in structure formation. As we anticipated, the effect is active on angular scales subtended by the horizon at the corresponding epoch, and larger. We shall come back to this point in the next sub-Section.

2.3.3 CMB BB spectrum

In Fig. 2.3, we show the CMB BB spectrum in red lines, along with a collection of current data. Two dashed lines correspond to the tensor perturbations generated during inflation with different amplitudes, quantified by the tensor-to-scalar ratio $r \equiv A_T/A_S$. The signal is much weaker than other spectra we see in Fig. 2.1. Two significant bumps at large scales are the definite characteristics of primordial BB spectra. The reionization bump at $\ell < 10$, comes from the re-scattering process at reionization epoch, as mentioned earlier. The recombination bump, peaking at $\ell \sim 100$, goes back to the last scattering at recombination epoch. On smaller angular scales, the contribution is suppressed because oscillations, although present and visible in the Figure, are not supported by gravitational potentials, as in the case of the temperature anisotropies. These bumps provide us a potential window to detect the existence of PGWs, which many on-going and future experiments are after, as we will see in next Sub-Section.

The observed BB signal can also receive contributions from scalar perturbations through CMB lensing effect. The latter is a second order effect in cosmology, made by forming structure acting on CMB anisotropies, and therefore in general it is capable of mixing E and B, and in particular converting a small portion of E into B-modes (Hu & Okamoto, 2002). The effect is dominating with respect to the tensor contribution on the arcminute scale, while, marginally, the latter dominates on the degree scale or more, if the tensor amplitude is high enough (Hu, 2000; Planck Collaboration VIII, 2020), as the solid red line in Fig. 2.3 shows. The lensing peak is centered around the arcminute scale, subtended by most dark

[4] http://bicepkeck.org/BK18_datarelease/BK18_components_20210607.txt

[5] https://lambda.gsfc.nasa.gov/product/act/act_dr4_spectra_info.html

[6] https://lambda.gsfc.nasa.gov/education/lambda_graphics/more/bb_upperlimits_source.html

matter lenses, still in linear regime, when the lensing deflection is most relevant for CMB photons, roughly between redshift 1 and 3. The dotted red line is the total BB signal from both lensing and tensor B-modes (for $r = 0.03$), which matches the latest results from the joint constraints from BICEP/Keck, *Planck* and WMAP data (Bicep/Keck Collaboration XIII, 2021). This is the most evident effect of lensing on CMB anisotropies. Other effects, which are not central for the current discussion, are represented by the smearing of acoustic peaks, as well as the reprojection of anisotropies on arcminute and degree scale onto smaller ones, where the contribution is actually relevant because of the fading of CMB anisotropies due to the thickness of the LSS.

2.4 CMB measurements

In this Section, we review the achievements, the challenges, and future projects from the observational side to detect CMB power spectra and understand the cosmological parameters, with a particular emphasis on the quest of primordial B-mode signal. The number of CMB observations is actually high, and we apologize in advance if some of the efforts have been omitted here, where we focus on the measurements which are more relevant in this work.

2.4.1 Brief history of CMB measurements

The first ever recognized detection of CMB radiation was achieved by Arno Penzias and Robert Wilson in 1964 (Penzias & Wilson, 1965), as a form of unexpected access in the signal received by a horn antenna. With the help from theorists of nearby universities, the latter excess was actually identified as the CMB (Dicke et al., 1965). The temperature anisotropy was first detected by the COBE satellite in 1992 (Smoot et al., 1992), as shown in Fig. 2.4[7], which mapped the whole sky in three microwave frequencies and provided the definite evidence for the black-body spectrum of CMB (Mather et al., 1994), although with a poor angular resolution, around 7°. Improved observations came up with the WMAP satellite, which made observations from 2001 to 2010 at five frequencies between 23 and 90 GHz at a resolution smaller than one degree (Bennett et al., 2013). WMAP also conducted the first full-sky measurement of the polarization signal of CMB and Galactic foregrounds at five microwave frequencies. Moving forward, the best full-sky CMB anisotropy data to date has been provided by the *Planck* satellite, operating from 2009 and 2014, reaching arcminute angular resolution, and improving sensitivity by a factor of about 10 with respect to WMAP. Planck and WMAP have also observed diffuse Galactic foregrounds, in total intensity and polarization, at the same frequencies, as well as extra-Galactic point sources. The latest and final major release of *Planck* results was in 2018-2019 (Planck Collaboration VI, 2020), with a recent update from Tristram et al. (2024).

Sub-orbital telescopes also provide a substantial contribution to the scientific commu-

[7] https://photojournal.jpl.nasa.gov/jpegMod/PIA16874_modest.jpg

nity. The first direct detection of the E-modes had been achieved with DASI (Kovac et al., 2002). The first detection of the gravitational lensing of the CMB was accomplished by ACT (Das et al., 2011) through a measurement of the four-point correlation function in the temperature maps. The B-mode lensing signal has been first detected by the SPTPol receiver on the SPT, in cross-correlation with CIB (Hanson et al., 2013).

Concerning the primordial-B modes, the BICEP/Keck project located at the South Pole at an altitude of 2800 meters first reported the detection of an excess over the lensing B-mode expectation at 150 GHz (BICEP2 Collaboration et al., 2014), corresponding to $r \sim 0.2$, which turned out to be consistent with polarized Galactic dust emission in a joint analysis combing multi-frequency data from *Planck* (BICEP2/Keck Collaboration et al., 2015). Using data from BICEP2, Keck Array and BICEP3 projects, their 2021 science results included measurements of the polarized microwave sky in 95/150/220 GHz on a patch of 400-600 square degrees centered around the south celestial pole, with a resolution at 20-30 arcminute. With this configuration, BICEP/Keck measures the polarized sky at angular scales $50 < \ell < 200$, which are minimally affected by lensing B-modes, and combine data with foreground-dominated channels from WMAP and *Planck* to better quantify the signal of polarized Galactic foregrounds. The detected B-modes are shown in black dots in Fig. 2.3, representing the tightest constraint up to date. Other datasets in Fig. 2.3 come from ongoing efforts at the quest of CMB B-modes including PolarBear (POLARBEAR Collaboration, 2022), SPT (SPT Collaboration, 2023) and ACT (Madhavacheril et al., 2024), all of which are consistently upgrading their detectors to improving their sensitivity.

Fig. 2.5[8] shows the most recent constraints of r from different dataset and the tightest constraint is $r < 0.032$ (Tristram et al., 2022), at a 95% confidence level, combining data from BICEP/Keck 2018, last *Planck* PR4 release and BAO measurement.

Most relevant results exist concerning balloon-borne probes as well. We quote one of the earliest evidences for the first three acoustic peaks and the flatness of the Universe, by BOOMERANG (Masi, 2002) and MAXIMA (Hanany et al., 2000). More recent probes, such as SPIDER (Spider Collaboration, 2022), have focused on polarization measurements.

2.4.2 Challenges of measuring CMB B-modes

The deployment of a number of observations briefly reviewed above requires the development of a robust data analysis pipeline, in terms of original study of algorithms, simulations, validation and actual data reduction. It is beyond of the scope in this Thesis to detail each of the corresponding layer of analysis, and in this Sub-Section we give just a brief description of the various analysis phases. We leave more details to more comprehensive work like (Partridge, 1995; Tristram & Ganga, 2007).

1. **Instrumental systematics**. Detectors transform the physical signal into electricity, tens of times per seconds, for months, or year, in TODs, requiring an explicit and

[8] https://lambda.gsfc.nasa.gov/education/lambda_graphics/r_upper_limits.html

most accurate knowledge of the detectors, such as noise properties, beam pattern, response to the temperature variation and so on, as well as a reliable pipeline for calibrating the voltage into physical units.

2. **Pointing and Map-making**. As we specified, TOD record the detected value for the specific pixels, corresponding to a specific direction in the sky, and associated time when the detectors. An accurate control of the pointing of the focal plane is necessary in order to properly reconstruct the distribution of the sky of the signal. Moreover, pixels are observed many times to control the noise level. It is necessary to compress the time information and make a sky map which has one value for each pixel on the sky, using techniques called map-making. The latter is not just a coaddition because, in particular, it needs to take into account the noise properties, in particular the time constants, which correlate noise properties on smaller time intervals.

3. **Component Separation**. The maps consist of CMB, diffuse foregrounds, Galactic and extra-Galactic sources. The sky maps at various frequencies can be seen as a linear combination of different components. In order to extract most of the CMB, which contains the cosmological information, component separation methods are required in order to separate other components out. We will return to this topic in a more detailed manner in the next Chapter.

4. **Power spectra Estimation**. With CMB maps which are extracted from a multi-frequency dataset through component separation, we can perform the estimation of the parameters. The information is usually compressed into power spectra, as mentioned in Sec.2.1, which are the objects that are interfaced with parameter estimation, also characterizing the noise in the angular domain, as well as taking care of the existence of areas of the sky which are not observed. The latter effect, in particular, causes **mode-coupling** as well as EB mixing problems if represented through harmonics defined on the sphere, which make C_ℓ at different multipoles and between different observables, correlated. The correlation can be inferred through the same geometry of the observation, and therefore, it can be treated and controlled.

5. **Parameter Constraints**. Statistical tools are needed to find which of the intervals of cosmological parameters can be compatible with observed spectra. MCMCs represent the most used methodology in order to get the posterior distribution of each parameter given our cosmological model, such as energy density of different species and the tensor-to-scalar ratio r, while marginalizing nuisance parameters such as foreground signals. Obtaining the constraints on the parameters is not the end of the analysis framework, on the contrary it provides the basic recipes for theorists to consolidate our cosmological models or tend to search for new alternatives.

2.4.3 Future CMB experiments

Tab.2.1[9] summarizes the basic configurations of the past, on-going and future CMB experiments. In this Sub-Section we focus on the future projects trying to pursuit the PGWs.

Table 2.1: Completed, ongoing and planned CMB signal detection experiments, including the name of the experiment, the duration, the angular scale range that can be detected, the detection frequency and the type of experiment. The Table has been adapted from the NASA LAMBDA website.

Project	Time	ℓ_{min}	ℓ_{max}	Frequency(GHz)	Type
BOOMERanG	1997-2003	25	1025	90-420	Balloon
COBE/DMR	1989-1993	2	40	31.5, 53, 90	Satellite
WMAP	2001-2010	2	1200	23, 33, 41, 61, 94	Satellite
BICEP2	2010-2012	21	335	150	Ground
Planck	2009-2014	2	2500	30, 44, 70, 95, 150, 217,353,545,857	Satellite
Keck Array	2012-2020	21	335	95,150,220,270	Ground
POLARBEAR	2012-	50	2000	150	Ground
SPTPOL	2012-	50	8000	95,150	Ground
ACTPOL	2013-	225	8725	90,146	Ground
SPIDER	2015-	10	300	90,150,280	Balloon
BICEP3	2016-	21	335	95	Ground
Advanced ACTPol	2016-	225	8725	28,41,90,150,230	Ground
SPT-3G	2018-	50	11000	95,150,220	Ground
BICEP Array	2020-	21	335	30, 40, 95, 150, 220, 270	Ground
Simons Observatory	2024-	30	8000	27, 39, 90, 150, 220, 270	Ground
Simons Array	Future	30	3000	90, 150, 220, 270	Ground
AliCPT	Future	20	900	90, 150	Ground
LiteBIRD	Future	2	200	40, 50, 60, 68, 78, 89, 100, 119, 140, 166, 195, 235, 280, 337, 402	Satellite
CMB-S4	Future	21	11000	20, 30, 40, 90, 150, 220, 270	Ground

With the start of observations this year (2024), SO (Ade et al., 2019), located in the Atacama desert, Chile, at about 5200 meters altitude, consists of three 42cm-diameter SATs to measure intermediate to large scales for about 10% of the sky, and one 6m-diameter LAT to measure small scales on about 40% of the sky, at frequencies between 27 and 280 GHz. Exploiting three highly sensitive low-resolution SATs is crucial for constraining degree-scale B-modes at the necessary low noise levels, while the LAT observes small-scale lensing B-modes in order to enable de-lensing of data from the SATs. The baseline program will have a precision of $\sigma(r) = 0.003$ (at 68% CL), after the nominal five years of observation

[9] https://lambda.gsfc.nasa.gov/product/expt/

(Ade et al., 2019). SO will also contribute to the science of neutrino mass, the reionization epoch, and late-time physics such as galaxy evolution.

AliCPT (Li et al., 2018) is located in Tibet, China, at 5250-meter altitude, and will observe at 90 and 150 GHz in order to provide the best ground measurement of CMB polarization from northern sky, which will be useful for cross check with those observing at south hemisphere. AliCPT will present sensitivity at $\sigma(r) = 0.02$ for its first phase (Ghosh et al., 2022).

As a next-generation satellite project, LiteBIRD (LiteBIRD Collaboration et al., 2023) is expected to perform a three-year full-sky survey in 15 frequency bands between 34 and 448 GHz, starting from late 2020s. By constraining large-scale B-modes LiteBIRD can measure r at a precision of $\sigma(r) = 0.001$.

In the same next decade, the next-generation ground-based experiment, CMB-S4 (Abazajian et al., 2016, 2019) will rely on 21 telescopes located at the South Pole and in the Chilean Atacama desert to measure sky at centimeter to millimeter wavelength, beginning at early 2030s. Similar to SO, CMB-S4 has also planned SAT and LAT to focus on large and small scales separately, but at unprecedented sensitivity, keeping a frequency range similar to the SO one, ranging from 30 to 270 GHz. One of the main science goals of CMB-S4 is to constrain the primordial tensor-to-scalar ratio at a precision of $\sigma(r) \sim 5 \times 10^{-4}$ (Abazajian et al., 2019).

As we can see in Tab.2.1, all the CMB experiments equip with detectors at around 150 GHz, where is the peak of CMB blackbody spectrum. Most of them also include low frequencies down to 20 GHz, and high frequency up to 400 GHz, with the main functions being quantifying the Galactic synchrotron emission and thermal dust emission at low and high frequencies, respectively. In the next Chapter, we discuss physical characterization of these foregrounds.

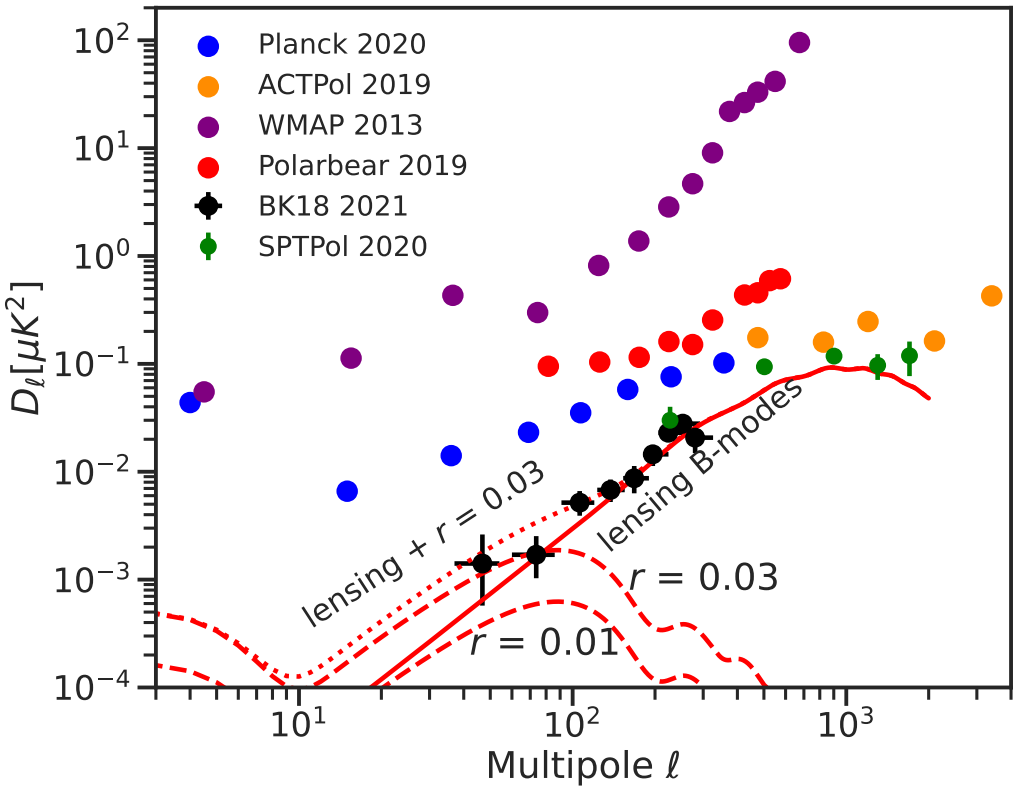

Figure 2.3: CMB BB power spectra from observational data (points) and theoretical prediction in solid red lines from ΛCDM model assuming *Planck* 2018 cosmology. Blues dots are the results for the bandpower of *Planck* 2018, while other data points are results from experiments showing in the legends. Data comes from the paper of BICEP2/Keck 2018[4] (Bicep/Keck Collaboration XIII, 2021), ACTPol[5] (Choi et al., 2020). Other data points are from NASA Lambda website[6], which includes *Planck* (Planck Collaboration V, 2020), WMAP (Larson et al., 2011), SPTPol (Sayre et al., 2020), Polarbear (POLARBEAR Collaboration, 2017).

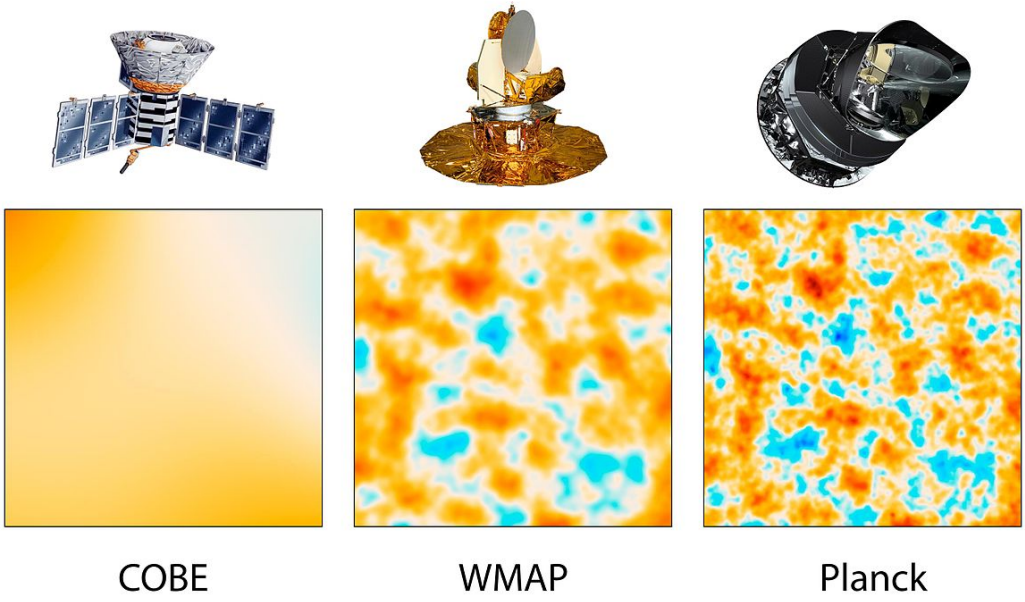

Figure 2.4: Cartoon illustrating three generations of satellite experiments of CMB since the 1990s: COBE, WMAP and *Planck* from left to right respectively. The upper part are the pictures of these three satellites, and the lower part is the detection results of the corresponding satellites in 10 square degree sky area. It can be clearly seen that the resolution is rapidly improving, and the *Planck* satellite is by far the most accurate measurement,which has brought us into the era of precision cosmology. Figure credit: NASA/JPL-Caltech/ESA.

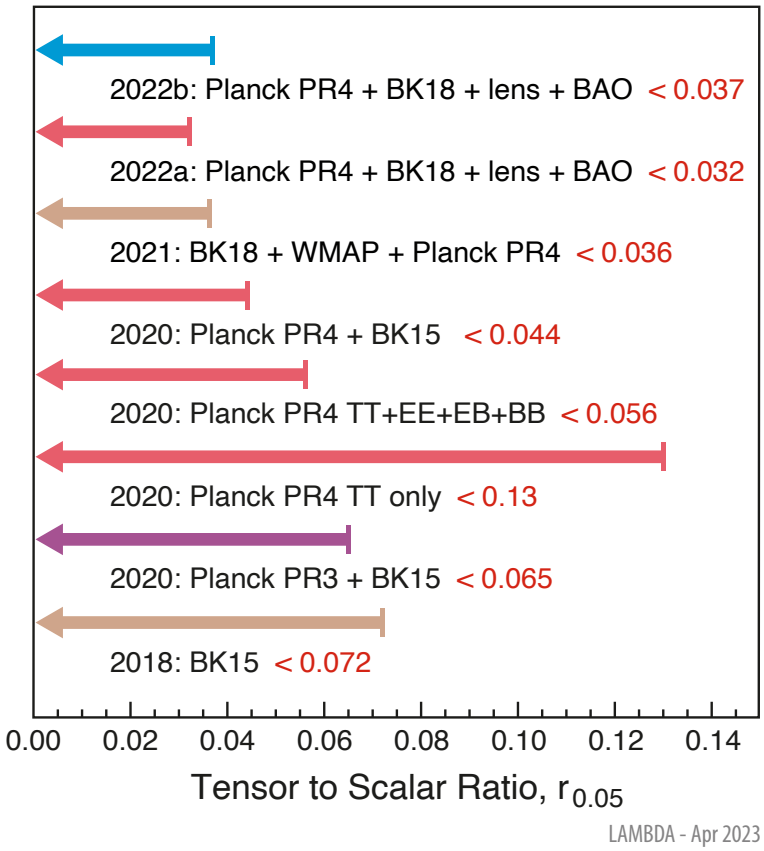

Figure 2.5: Constraints of the tensor-to-scalar ratio, r, from different combination of existing datasets. Figure adapted from NASA LAMBDA website.

3

CMB Foregrounds

Let us talk about the foregrounds!

Astrophysical emissions from our own Galaxy, as well as extra-Galactic sources, exhibit a variety of emission processes which contaminate CMB measurements. The CMB can be separated out of the other astrophysical contaminants by means of multi-frequency observations, since foregrounds possess a markedly different behavior in frequency with respect to a black body. This occurrence is very well known in cosmology, and is the subject of an entire layer of data analysis, represented by the component separation, see, e.g., Planck Collaboration XI (2020). Diffuse foreground emissions from our own galaxies, in particular, are polarized, and therefore contaminate CMB polarization as well. The contamination is particularly relevant for the B-modes, due to their weakness with respect to the other component, and cannot be neglected ay any frequency, and any position in the sky (Krachmalnicoff et al., 2016, 2018). In this Chapter we review the basic physics of diffuse Galactic foregrounds, and their expected contamination to CMB B-modes. We will limit our text to the information which is needed in the following Chapters, which focus in particular on the modeling of Galactic foregrounds. The latter is common to several probes, including in particular B-mode probes, such as SO, S4, LiteBIRD.

In Sec.3.1 we describe the physical mechanism, phenomenological modeling and current measurement of the foregrounds, mainly in polarization. In Sec.3.2 we describe the current assessment of their contamination to CMB B-modes and impact from their non-Gaussianity in Sec.3.3. After that, we describe the current methodologies for component separation in

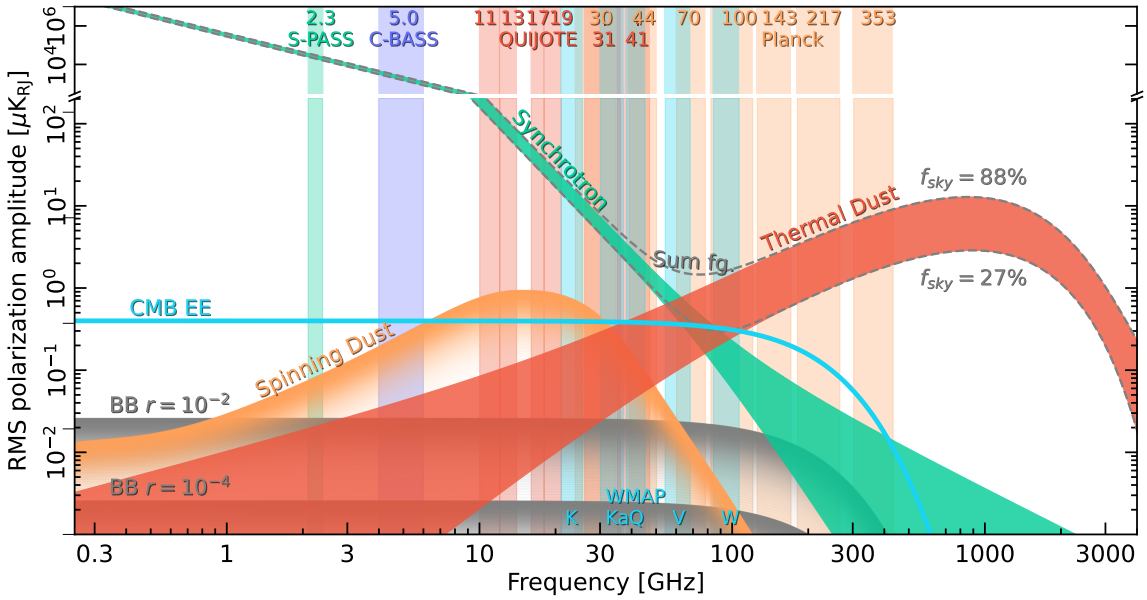

Figure 3.1: Spectrum in polarization of each physical component from observational data at frequencies in the range of [300 MHz, 3000GHz]. The AME (Spinning Dust in the figure, orange curve) represents current upper limit, rather than a detection. The lower and upper bound of each component come from two different masks with sky fractions of 88 and 27 %. Vertical bands indicate the band coverage of each experiment. Figure adapted from (BeyondPlanck Collaboration I, 2023)

Sec.3.4. Finally, in Sec.3.5, we discuss the latest developments for foreground modeling, which will be the subject of following Chapters.

3.1 Mechanism, modeling and measurements of foregrounds

The primary source of contamination to CMB B-modes arises from astrophysical processes causing diffuse emissions within our own Galaxy. The spectral behavior of each foreground component is shown in Fig.3.1, which we discuss about with more details in the following, specializing the discussion for most of the components highlighted in the figure.

3.1.1 Thermal dust

In our Galaxy, emission from dust grains is the dominant component at high frequencies ($\gtrsim 70$ GHz) in both temperature and polarization (Planck Collaboration XII, 2020). Dust consists mainly of carbonaceous particles, silicate compounds and polycyclic aromatic hy-

drocarbons. These particles produce radiation by reacting with the ISM in which they are heated by absorbing starlight in the optical band from newly formed stars and cooled by radiating in the far infrared (e.g., Draine (2011)). Moreover, the non-spherical dust grains tend to align their minor axis with the local magnetic field and the radiation tends to be stronger along the major axis of the grains which is perpendicular to the direction of the magnetic field, i.e., the signal from thermal dust emission is polarized. Observation shows that dust can have up to 20% polarization fraction at intermediate and high Galactic latitudes (Planck Collaboration XII, 2020).

The observed dust emissivity is the result of radiation by all emitting dust grains along the line of sight. For the frequencies of interest to CMB experiments, the final emission spectrum on the sky can be well described by the blackbody radiation with power-law spectral corrections, shown in Fig.3.1 in red band, which can be modeled as a function of the sky direction $\hat{\mathbf{n}}$ and frequency ν, as

$$\begin{aligned} I_\nu^{\rm d}(\hat{\mathbf{n}}) =& A_{I,\nu_I}(\hat{\mathbf{n}})\,(\nu/\nu_I)^{\beta_d(\hat{\mathbf{n}})}\,B_\nu\left(T_d(\hat{\mathbf{n}})\right)\,, \\ \left\{Q_\nu^{\rm d}(\hat{\mathbf{n}}), U_\nu^{\rm d}(\hat{\mathbf{n}})\right\} =& \{A_{Q,\nu_P}(\hat{\mathbf{n}}), A_{U,\nu_P}(\hat{\mathbf{n}})\}\times \\ & (\nu/\nu_P)^{\beta_d(\hat{\mathbf{n}})}\,B_\nu\left(T_d(\hat{\mathbf{n}})\right)\,, \end{aligned} \tag{3.1}$$

where $A_\nu(\hat{\mathbf{n}})$ are the intensity (I) and polarization (Q, U) templates at the reference frequencies ν_I and ν_P, which are basically the frequencies of the observational templates. For example, *Planck* observations at 545 GHz in intensity and 353 GHz in polarization are utilized to be the templates of dust emission in `PySM`. B_ν is the Planck function. β_d and T_d in Eq.3.1 are the spectral index in the power law and temperature parameter in the Planck function, respectively, which should also be functions of sky position and different for temperature and polarization.

Moreover, T_d depends on the interstellar radiation field (heating process) and efficiency of emitting far-infrared light (cooling process) of the dust grains, thus the complexity of the environments and distinct shapes of dust grains both across the sky and along the line of sight may lead to multiple temperatures of various dust components. While single-component models can fit observational data well, two or even more components are in some case needed to jointly describe the dust emission for a more accurate description (Finkbeiner et al., 1999).

Given the complicated physics of dust, various choices can be made when constructing simulations considering different level of complexity (Thorne et al., 2017; Zonca et al., 2021) (which also applies for other foreground components discussed below). The simplest dust model in `PySM3`[1] assumes that these two spectra parameters are fixed constants across the sky, with $(\beta_d^I, \beta_d^P) = (1.48, 1.53)$ and $T_d = 19.6$K (Planck Collaboration Int. XXII, 2015; Planck Collaboration XI, 2020).

[1] `https://pysm3.readthedocs.io/en/latest/models.html`

Another consequence of multiple population of dust grains is **decorrelation**, the phenomenon that the dust SEDs do not scale rigidly with frequency (which is the case of fully correlation). Planck Collaboration XI (2020) found no evidence of decorrelation using four polarized channels from 100 to 353 GHz.

At the power spectra level, thermal dust emission at a specific frequency can also be fitted with a power law of the form

$$\mathcal{D}_\ell{}^{XY} \equiv \frac{\ell(\ell+1)C_\ell^{XY}}{2\pi} = A^{XY}(\ell/80)^{\alpha_{XY}+2}\,, \tag{3.2}$$

where $X, Y \in \{T, E, B\}$, A and α are the amplitudes and exponents evaluated at the pivot scale, $\ell = 80$, which corresponds to the angular scale where the maximum of the contribution from theoretical PGWs is located. These parameters have statistically significant variations over sky regions. *Planck* data for the `LR71` region gives fitted values $\alpha^{EE} = -2.42 \pm 0.02$ and $\alpha^{BB} = -2.54 \pm 0.02$, respectively (Planck Collaboration XI, 2020). Notably, there exists a E/B power asymmetry, namely $A^{BB}/A^{EE} \approx 0.5$ (also see Planck Collaboration Int. XXX (2016)), which has been considered as statistical signature of turbulence in the magnetized ISM from magnetohydrodynamic simulations (Kritsuk et al., 2018), or due to the correlation between the filaments in dust distribution and the magnetic field orientations (Planck Collaboration Int. XXXVIII, 2016), although still under debate. A significant TE correlation is also observed, which can be explained by the alignment of density structures with the magnetic field as well (Planck Collaboration XI, 2020).

3.1.2 Synchrotron

As the dominant component at low ($\lesssim 70$ GHz) frequencies, synchrotron emission originates from relativistic cosmic ray electrons spiraling (accelerating) around the GMF and it is polarized perpendicular to the magnetic field lines, with mean polarization fraction having different values and morphology across the sky (Planck Collaboration IV, 2020).

The intensity and spectrum of synchrotron radiation depends on the cosmic ray energy and the strength of the magnetic field in the direction perpendicular to the line of sight. For electrons with a power-law energy distribution $N_e(E) = E^{-\mathrm{p}}$, the resulted synchrotron emission also follows a power-law spectrum $I_\nu \propto B^{(p+1)/2}\nu^\beta$ with $\beta_s = -(\mathrm{p}+3)/2$ (Rybicki & Lightman, 1985) where B is the magnitude of the magnetic field strength.

The simplest form of the synchrotron emission thus can be parameterized as (which is also utilized in `PySM3`):

$$I_\nu^{\mathrm{Synch}}(\hat{\mathbf{n}}) = A_{\nu_0}(\hat{\mathbf{n}})\left(\frac{\nu}{\nu_0}\right)^{\beta_s(\hat{\mathbf{n}})}\,, \tag{3.3}$$

where A_{ν_0} is the synchrotron emission template, which is commonly taken as reprocessed Haslam 408 MHz data (Remazeilles et al., 2015) for intensity and the WMAP Q/U maps at 23 GHz (Bennett et al., 2013) for polarization. Results from S-PASS polarization map

combining *Planck* and WMAP data recovered an average value $\beta_s = -3.22 \pm 0.08$ for EE and BB power spectra from different sky regions (Krachmalnicoff et al., 2018), which are consistent with the results found in Martire et al. (2022) dealing with *Planck* and WMAP data only.

Similar to dust emission, multiple components of electrons can result in spatially varying spectra index β_s. Besides that, the superposition of multiple components can also lead to the flattening of β_s. On the other hand, as synchrotron sources age their SED steepens, since high frequency radiation corresponds to higher energy particles which radiate energy away most rapidly. The potential steepening and flattening can be described by introducing an additional **curvature** parameter in model of Eq.3.3 which can be generalized as

$$I_\nu^{\rm Synch}(\hat{\mathbf{n}}) = A_{\nu_0}(\hat{\mathbf{n}}) \left(\frac{\nu}{\nu_0}\right)^{\beta_s(\hat{\mathbf{n}})+C\ln\left(\frac{\nu}{\nu_c}\right)}, \tag{3.4}$$

where positive C corresponds to flattening and negative C to steepening.

At the power spectrum level, the power-law described in Eq. 3.2 provides a good fit to synchrotron data as well. The S-PASS experiment constrains the synchrotron spectral index, α_s, to approximately -3.15 within an iso-latitude mask for Galactic latitudes $|b| > 30°$. Additionally, the data also reveals an asymmetry of $A^{BB}/A^{EE} \approx 0.5$ for $|b| > 35°$ (Krachmalnicoff et al., 2018).

Another interesting manifestation, also known as **depolarization effect**, happens for the observations of synchrotron emission, especially at low frequencies and low Galactic latitude due to the **Faraday rotation** (Ichiki Kiyotomo, 2014; Krachmalnicoff et al., 2018). Faraday rotation effect changes the polarization angles of electromagnetic waves propagating through the ionized Galactic medium in the presence of the magnetic field and leads to emission regions with different polarization angles across the entire Galactic disk. The superposition of these emissions then results in the observed decline of polarization degree.

We have seen that both polarized thermal dust emission and synchrotron are related the GMF, therefore these two components are expected to have some degree of correlation, which brings more complexity into the modeling of foregrounds with the aim of detecting the primordial CMB B modes (Bicep/Keck Collaboration XIII, 2021). Planck Collaboration XI (2020) detected this correlation which decreases with increasing multipole and is detected with high confidence only for $\ell < 40$, through the computation of cross angular power spectra between WMAP low frequency channels, which are sensitive to synchrotron emission and *Planck* high frequency channels, which are dominated by thermal dust emission. A similar correlation is also found by comparing S-PASS data at 2.3 GHz with *Planck* data at intermediate and high latitudes (Krachmalnicoff et al., 2018).

Thermal dust and synchrotron emissions are the two main signals in the polarization maps, while other foregrounds only have power in temperature or only exhibit small degree of polarization, which we will discuss in the following Sections.

3.1.3 Free-free

Free-free emission, also known as thermal bremsstrahlung, arises from the scattering process between electrons and ions in interstellar plasma (Rybicki & Lightman, 1985). This emission is expected to be intrinsically unpolarized due to the randomness of the Coulomb interactions between electrons and ions. Upper limits on the polarization fraction over the sky have been obtained to be about 1% (Macellari et al., 2011). Nevertheless, at the edges of bright ionized clouds, additional scattering of electrons can result in higher polarization fractions of about 10% (Fraisse et al., 2009).

The frequency scaling of free-free emission is determined by the number of free protons and electrons along the line of sight, which is commonly quantified in terms of *emission measure*, i.e., the integrated, squared electron density along the line of sight, assuming the number densities of free protons and electrons are equal (Draine, 2011). It is very close to a power law of -2.14 at frequencies greater than 1 GHz, while at low frequencies, the medium for free-free emission becomes optically thick, leading to a break in the power-law frequency scaling (Planck Collaboration X, 2016).

3.1.4 AME

AME is a prominent Galactic emission in the frequency range 20-40 GHz, which is spatial correlated with dust on degree scales, with peak brightness roughly four orders of magnitude less than that of thermal dust emission, and having little polarization (see a recent review Dickinson et al. (2018)).

As the name tells, the physical mechanism responsible for AME is not clearly understood yet, which is only known for less than 30 years (Kogut et al., 1996). A widely-accepted model states that the ultra-small, rapidly spinning dust grains with electric dipole are responsible for AME (Draine & Lazarian, 1998), partly due to the strong spatial correlation between AME and thermal dust emission in the range 300-3000 GHz(e.g., Poidevin et al. (2023)). A magnetic dipole emission from dust grains may also plausibly explain the anomalous emission (Draine & Hensley, 2013). Its polarization properties are also not well understood yet, with recent results on large angular scales using *Planck* and WMAP data indicating that its polarization fraction varying from 0.6% to 2.5%, depending on the prior on β_s, i.e., the spectral index of synchrotron (Herman et al., 2023).

Not only detected in our Galaxy, there is also evidence of AME in other galaxies such as the Andromeda Galaxy (M31), which is the largest galaxy in the Local Groupe (see a recent measurement from QUIJOTE-MFI[2] (Fernández-Torreiro et al., 2024)).

The SED of AME can be described by a log-normal distribution (Stevenson, 2014) which have the form

$$I_\nu^{\rm AME}(\hat{\mathbf{n}}) = A_{\rm AME}(\hat{\mathbf{n}}) \exp\left[-\frac{1}{2W_{\rm AME}^2} \ln^2\left(\frac{\nu}{\nu_{\rm AME}}\right)\right] , \tag{3.5}$$

[2]Q-U-I JOint Tenerife Experiment Multi Frequency Instrument

where $A_{\rm AME}$, $\nu_{\rm AME}$ and $W_{\rm AME}$ are the AME peak flux density, frequency and width.

3.1.5 Other Galactic foregrounds and Extra-galactic emission

In addition to the above diffuse Galactic foregrounds which are commonly discussed in the literature, there are also other kinds of foregrounds in the Galaxy like CO line emission and zodiacal light in our Solar System. Several extra-Galactic effects are also important for CMB frequencies, including the SZ effect. They are not central for our discussion, as the dominant contaminations to the CMB B-modes are represented by the ones we already discussed, and especially dust and synchrotron, as we shall see in the following Sections.

- CO lines. When electrons in a molecule move from one energy level to a lower energy level, there will be molecular transition emission at a certain frequency, determined by *Planck*'s energy-frequency relation. CO resides in the dense molecular clouds distributed in ISM and emits line emission due to the rotational transition. Especially, three lines at 115, 230 and 345 GHz from $J = 0 \to 1$, $J = 1 \to 2$, $J = 2 \to 3$ respectively, contribute significantly in the *Planck* intensity maps (Planck Collaboration XIII, 2014).

- Zodiacal light. In our Solar System, dust particles and grains in the ecliptic plane generate ZE which is a source of radiation observable from the optical to the sub/millimeter regimes. In CMB studies, the ZE is a local foreground whose structure varies significantly based on the observer's location within the Solar System. Consequently, each experiment detects a unique ZE signal due to variations in scanning strategies and telescope positions. This means that, unlike most Galactic foregrounds which can be described using a single template, the ZE must be specifically modeled for each specific experiment (San et al., 2022).

- SZ effect. Hot electrons in ionized gas interact with incoming photons through inverse Compton scattering and shift the energy of the photons. In particular, background CMB photons are scattered by hot gas in clusters of galaxies in the universe and result a variation in temperature, which is called SZ effect (Sunyaev & Zeldovich, 1972). There are two kinds of SZ effects: the tSZ effect referring to the interaction of the CMB photons with a hot, thermalized electron gas, and kSZ corresponding to interaction with electrons having a net ensemble peculiar velocity along the line of sight. An important difference between these two effects is that tSZ has a different frequency dependency with CMB anisotropies while kSZ exhibits the same dependence which makes kSZ more difficult to detect through CMB observations. Moreover, different with diffuse emission we have mentioned, SZ effects are localized to happen around galaxy clusters, which act like point sources in the observed CMB maps.

- Extra-Galactic point sources. They appear as unresolved, point-like objects in CMB measurements at microwave frequencies due to the limited resolution of CMB experiments, while the bright, resolved ones are fitted and removed from maps using suitable filters (Puglisi et al., 2018; Diego-Palazuelos et al., 2021). These sources are primarily associated with synchrotron radiation from active galactic nuclei and dusty, star-forming galaxies, becoming significant contaminants in the CMB at very small scales and therefore impacting CMB lensing reconstruction and the detection of low values of r.

3.2 Contamination to CMB B-modes

Let us now turn to examine the foreground contamination to the CMB polarization, in the EE and BB modes and power spectra, expressed as $D_\ell \equiv \ell(\ell+1)C_\ell/2\pi$. The foreseen levels of the main polarized foregrounds, dust and synchrotron, are shown in the left and right plots of Fig.3.2, respectively for EE and BB. The colored bands represent the various levels which are expected when different sky fractions are considered. Foregrounds are highly non-stationary in their variations and statistics across the sky. The main variable affecting the level of contamination is represented by the Galactic latitudes which are considered: the higher is the signal, the closer is the boundary of the region which is considered to the Galactic plane. The theoretical CMB EE and primordial BB signal for different r values, together with lensing, assuming *Planck* 2015 ΛCDM parameters (Planck Collaboration XIII, 2016), are also shown.

Still focusing on the power spectra, we add another layer of information to the previous figure. In Fig.3.3, the quantity

$$\begin{aligned} f(\ell,\nu) &= \sqrt{\frac{D_\ell^{\rm s}(\nu)+D_\ell^{\rm d}(\nu)}{D_\ell^{\rm CMB}}} \\ &= \sqrt{\frac{A_{\rm s}\left(\frac{\ell}{80}\right)^{\alpha_{\rm s}}\frac{s_{\rm s}(v)}{s_{\rm s}(30{\rm GHz})}+A_{\rm d}\left(\frac{\ell}{80}\right)^{\alpha_{\rm d}}\frac{s_{\rm d}(v)}{s_{\rm d}(353{\rm GHz})}}{D_\ell^{\rm CMB}}}\,, \end{aligned} \tag{3.6}$$

where subscripts 'd' and 's' refer to thermal dust and synchrotron, is shown, representing the ratio of the foregrounds and CMB BB power across the ℓ and frequency spaces. The dependence of this ratio across frequency follows the scalings $s_{\rm s}(v)$ and $s_{\rm d}(v)$ which are defined for synchrotron in Eq.3.3 and dust in Eq.3.1, respectively. The multipole dependence is described by Eq.3.2 with spectral indices α_s and α_d. The numerical values of parameters are obtained in (Planck Collaboration IV, 2020) which is the work where the Figure has been produced. As for CMB B-modes, the signals are derived from ΛCDM model including lensing-induced ones, shown in red and black contours in Fig.3.3 with and without contribution from PGWs.

By combining the information in Fig.3.1, 3.2, 3.3, we can clearly see that, with the possible exception of frequencies around 100 GHz, and $\ell \sim 1000$ where lensing B-modes

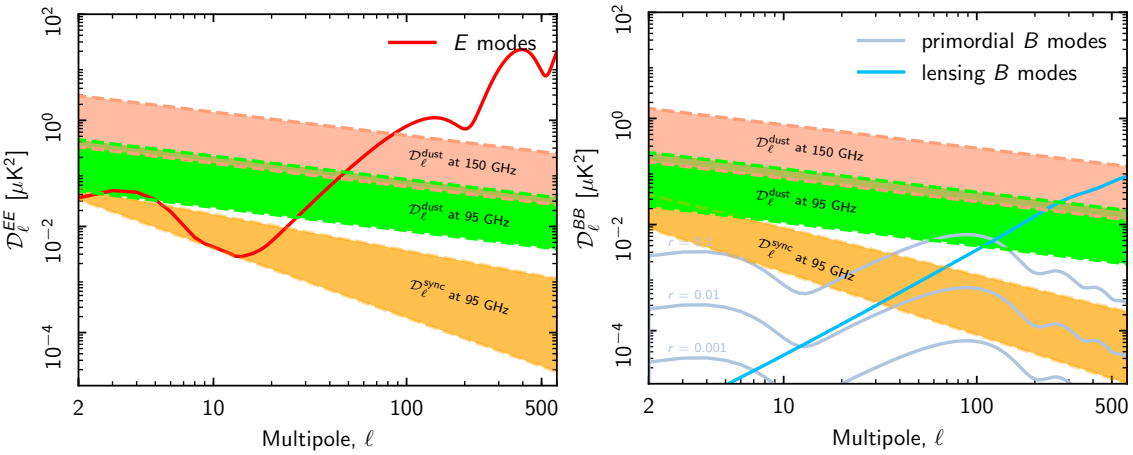

Figure 3.2: EE (left) and BB (right) power spectra of thermal dust and synchrotron emission, at 95 and 150 GHz. Colors covers the expected range of the amplitudes for different sky fractions. CMB EE and BB spectra are also shown. Figure adapted from (Planck Collaboration XI, 2020).

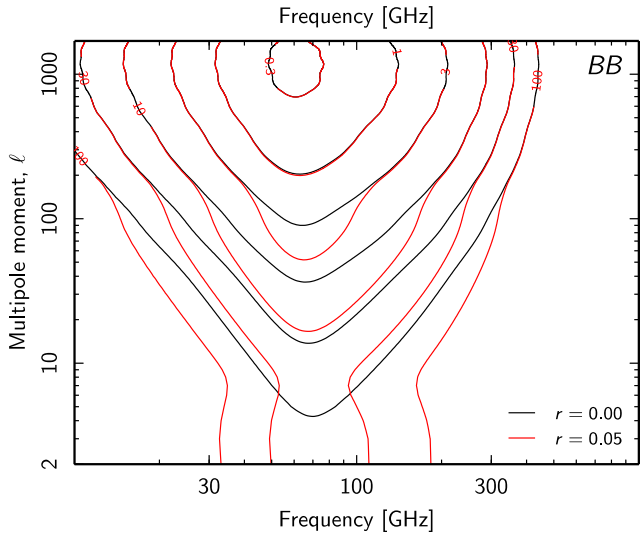

Figure 3.3: Iso-contour of the expected ratio between BB power spectra of total polarized foregrounds, defined as $f(\ell,\nu) = \left[D_\ell^{\rm fg}(\nu)/D_\ell^{\rm CMB}\right]^{1/2}$. Black and red curves correspond to the CMB B-modes of $r = 0.0$ and 0.05, including lensing signal. Figure adapted from Planck Collaboration IV (2020).

dominate, the foregrounds are comparable or dominating with respect to the CMB B-modes in the entire $\nu - \ell$ space. This evidence does not come as a surprise. Early analyses already indicated this occurrence (Baccigalupi, 2003), confirmed by WMAP (Page et al., 2007), and later using *Planck* and radio surveys (Planck Collaboration IV, 2020). Krachmalnicoff et al. (2018) further conclude that foregrounds cannot be neglected at any place or any frequency if the primordial B-modes are originating from PGWs with r comparable or smaller than 10^{-2}.

3.3 Foreground non-Gaussianity

As we anticipated, diffuse foregrounds generally exhibit a large degree of non-Gaussianity. This evidence comes primarily from large-scale observations both in total intensity and polarization (Miville-Deschênes et al., 2007; Ben-David et al., 2015; Coulton & Spergel, 2019; Allys et al., 2019) and is expected to also be true at smaller scales, since dust grains are highly locally distributed and the magnetic field in the diffuse ISM is highly turbulent.

The foreground non-Gaussianity introduces couplings between different modes in the angular power spectra, which determine non-diagonal terms in the covariance matrices of the observed signal. On the other hand, covariance matrices are usually treated as diagonal under the assumption that all the sky components behave like Gaussian random fields (e.g., Planck Collaboration VIII, 2020). This occurrence may introduce systematics errors, if the foregrounds are treated as Gaussian signals in analysis framework, or also an advantage, if new methodologies are designed to remove the foregrounds based on their statistics of order larger than the two point correlation signal, where the CMB contribution is negligible.

In the case of B-modes from PGWs, Abril-Cabezas et al. (2024) claim that the constraints on r are robust using the polarized dust at the power spectra level, but they only focus on $30 \leq \ell \leq 300$, the angular scales at which the PGWs cause a maximum B-mode contribution. At smaller scales where lensing dominates and produce non-Gaussianity into the CMB maps, the residual non-Gaussian foreground will possibly cause bias to lensing reconstruction (Beck et al., 2020) and de-lensing.

Moreover, non-Gaussianity of foregrounds also affects PNG measurements (Planck Collaboration IX, 2020) (see Sec.1.3.5). Cabella et al. (2010) used a bispectrum estimator based on needlets in order to constrain $f_{\rm NL}$ and found that foreground residuals in WMAP 5-year data can lead to bias. In Jung et al. (2018), the authors used the binned bispectrum estimator to calculate the bispectra of various Galactic foreground components derived by `Commander` from *Planck* 2015 data and assessed their impact on PNG.

In summary, foregrounds are non-Gaussian, non-stationary, non-linear at all angular scales, and their power spectra, down at least to the degree scale, is comparable or higher than cosmological B modes at any frequency, any angular scale. Current observations of polarized foregrounds are limited to degree scales over a large sky fraction and can only reach a higher resolution at sub-degree or arcminute scales for portions of the sky (Planck Collaboration XI, 2020; Bernardi et al., 2004; Remazeilles et al., 2015). Apparatuses which

are capable of simulating polarized emissions, and in particular at the arcminute scale where data are lacking is strategically important for CMB B-mode measurements, and we will mention the latest progress in Sec.3.5, while in the next Section we focus on the class of algorithms, known up to date, which are able to separate background and foreground diffuse emissions in CMB observations.

3.4 Component Separation

The set of data analysis methods capable of extracting the CMB anisotropies out of a multi-frequency dataset is known as Component Separation. Several implementations exist, exploiting the different properties that CMB and foregrounds have, such as frequency dependency and spatial distribution. Depending on the assumptions made about the foregrounds, these methods can generally be classified into blind (Yao et al., 2018; Delabrouille et al., 2009) and parametric ones (Stompor et al., 2009; Planck Collaboration IV, 2020; BeyondPlanck Collaboration I, 2023). Blind methods come from the blindness to the nuisance components and focus only on the signal of interest, when performing the foreground removal. On the other hand, parametric methods usually build a detailed physical models to represent the observed data with numerous parameters, including cosmological, astrophysical and instrumental ones. In this Section we will introduce the methods which are most known and developed by the CMB community. For reviews we refer to Delabrouille & Cardoso (2007); Leach et al. (2008); Planck Collaboration IV (2020).

We note that, in practice, datasets from CMB experiments are usually expressed in **thermodynamic units** since in this way the CMB anisotropies, which are derivatives of a blackbody spectrum, become constant at different frequencies. That is, the frequency dependence of CMB can be described with a simple vector which is filled with 1.

3.4.1 ILC

The ILC method was first casted in the harmonic domain by Tegmark & Efstathiou (1996) and has many variations with different improvements (e.g., Delabrouille et al. (2009); Remazeilles et al. (2011); Carones & Remazeilles (2024)). As the name tells, it constructs the estimator of the $a_{\ell m}$s in the harmonic or spatial domain, which has the aim to minimize the contamination from Galactic and extra-Galactic foregrounds and instrumental noise. Specifically, in the harmonic ILC case, the estimator $\hat{s}_{\ell m}$ is a linear combination of the observed $x^i_{\ell m}$ at frequency i which can be written as

$$\hat{s}_{\ell m} = \sum_i w^i_\ell x^i_{\ell m}\,, \tag{3.7}$$

where w^i_ℓ are the weights at frequency i and multipole ℓ, which are determined by the constraint that the estimator should have minimum variance among the possible estimators,

that is, the weighted power spectrum is minimized through

$$\arg\min_{\boldsymbol{w}_\ell} \left\langle |\hat{s}_{\ell m}|^2 \right\rangle = \boldsymbol{w}_\ell^T \boldsymbol{C}_\ell \boldsymbol{w}_\ell, \quad s.t. \sum_i w_\ell^i = 1\,, \tag{3.8}$$

where $\boldsymbol{w}_\ell$ is the vector consisting of w_ℓ^i and $C_\ell^{ij} = \left\langle \left(x_{\ell m}^i\right)^\dagger x_{\ell m}^j \right\rangle$. In the implementations the $\boldsymbol{C}_\ell$ is estimated by $\hat{\boldsymbol{C}}_\ell$:

$$\hat{\boldsymbol{C}}_\ell \equiv \frac{1}{2\ell+1} \sum_m \mathbf{x}_{\ell m} \mathbf{x}_{\ell m}^\dagger\,, \tag{3.9}$$

where $\mathbf{x}_{\ell m}$ represents data vector of all the frequency channels. The constraint in Eq.3.8 makes it explicit that the CMB signal is lossless in the recovered map. The weights can be obtained with the *Lagrange multiplier* method, which gives

$$\boldsymbol{w}_\ell = \frac{\boldsymbol{C}_\ell^{-1}\boldsymbol{e}}{\boldsymbol{e}^T \boldsymbol{C}_\ell^{-1} \boldsymbol{e}}\,, \tag{3.10}$$

where $\boldsymbol{e}$ is a vector filled with 1, which is the frequency dependence of CMB component.

As a blind method, ILC makes no assumption about the foregrounds and only assumes that the component of interest, CMB, is independent with foregrounds, which is valid for most of the scales (multipoles). At large scales, however, there may be chance correlation between CMB and foregrounds, leading to the well-known *ILC bias* in the final reconstructed CMB power spectrum (Delabrouille et al., 2009; Saha et al., 2008).

ILC also makes an implicit assumption that the spectral scaling of foregrounds is spatially uniform, which is not the case since foregrounds differs a lot across sky. Improvements exist by working in *needlet* space, known as NILC (Delabrouille et al., 2009; Planck Collaboration IV, 2020). Needlets enable localized filtering in both pixel and harmonic spaces. This localization in pixel space allows the weights in the linear combination to adapt to the local conditions of foreground contamination and noise. Meanwhile, localization in harmonic space enables the method to prioritize foreground rejection on large scales and noise exclusion on small scales.

NILC was further generalized to be GNILC in Remazeilles et al. (2011) to allow for the estimation of foreground components, and was applied to construct maps of the thermal dust emission from *Planck* data (Planck Collaboration Int. XLVIII, 2016a), with the advantage that the recovered thermal dust maps are free of cosmic infrared background anisotropies.

3.4.2 ICA

Similar to ILC, ICA depends on the prerequisite that CMB and foregrounds are statistically independent and constructs the estimator that is also a linear combination of frequency maps. ICA further assumes that the observed signal is a linear combination of several physical components, which means that ICA relies on a mathematical model for

each component. SMICA is a well-developed algorithm to do the component separation (Delabrouille et al., 2003; Delabrouille & Cardoso, 2007; Cardoso et al., 2008), which is based on *spectral* statistics, that is, starting from Eq.3.9, although, originally, ICA methods were used to exploited the non-Gaussianity of foregrounds in the real space, by means of machine learning (Baccigalupi et al., 2000).

Different from ILC, SMICA does not substitute $\hat{\boldsymbol{C}}_\ell$ to be the $\boldsymbol{C}_\ell$. On the contrary, it constructs a model for the data power spectra which is parameterized by a set of parameters θ, written as

$$\boldsymbol{C}_\ell(\theta) = \left[\begin{array}{cc} \boldsymbol{a} & \boldsymbol{F} \end{array} \right] \left[\begin{array}{cc} C_\ell^{\rm CMB} & 0 \\ 0 & \boldsymbol{P}_\ell \end{array} \right] [\boldsymbol{a} \quad \boldsymbol{F}]^\dagger + \boldsymbol{N}_\ell \,, \tag{3.11}$$

where $C_\ell^{\rm CMB}$ is the CMB power spectrum at multipole ℓ and $\boldsymbol{a}$ is a $\mathrm{N_{fre}}\times$ 1 column vector denoting the frequency dependence of the CMB signal, and $\mathrm{N_{fre}}$ indicates the total number of bands of the experiment. $\boldsymbol{F}$ is a $\mathrm{N_{fre}} \times \mathrm{N_{fg}}$ matrix representing the frequency dependence corresponding to the $\mathrm{N_{fg}}$ kinds of foreground components, which can be ℓ dependent. $\boldsymbol{P}_\ell$ is a positive definite $\mathrm{N_{fg}} \times \mathrm{N_{fg}}$ foreground covariance matrix and $\boldsymbol{N}_\ell$ is the diagonal noise matrix.

The best fit values of these parameters are obtained by minimizing the "spectral mismatch" between $\boldsymbol{C}_\ell$ and $\hat{\boldsymbol{C}}_\ell$, which is identical to maximizing the likelihood of the data in a model where all components are Gaussian distributed, stationary and independent:

$$\hat{\theta} = \arg\min_\theta \sum_\ell (2\ell+1) \left[\mathrm{Tr}\left(\hat{\boldsymbol{C}}_\ell \boldsymbol{C}_\ell^{-1}(\theta) \right) + \log\det \boldsymbol{C}_\ell(\theta) \right] . \tag{3.12}$$

The parameters of $C_\ell(\theta)$ include $C_\ell^{\rm CMB}$, $\boldsymbol{P}_\ell$, $\boldsymbol{a}$, $\boldsymbol{F}$ and the diagonal elements of the matrix N_ℓ. A key point for the parameter fitting process is the optimization. How to find the most suitable algorithm so that the formula Eq.3.12 can converge quickly and stably requires a combination of mathematical, physical and computer knowledge. Commonly used algorithms include Expectation-Maximization (Delabrouille et al., 2003) and Conjugate Gradient (Cardoso et al., 2008).

3.4.3 Parametric methods

Parametric component separation methods construct an explicit model to represent the experimental data, taking all the possible physical signals and complete instrumental systematics into account and assuming that the functional forms of the frequency scaling for all relevant components are known. The basic equation for this approach is

$$d_v(p) = g_v \sum_{c=1}^{N_c} \mathrm{F}_v\left(\beta_c\right) s_c + n_v(p) \,, \tag{3.13}$$

where $d_v(p)$ indicates the observed data at frequency ν and pixel p. The sum runs over N_c modeled physical components, such as CMB and foregrounds mentioned in Sec.3.1,

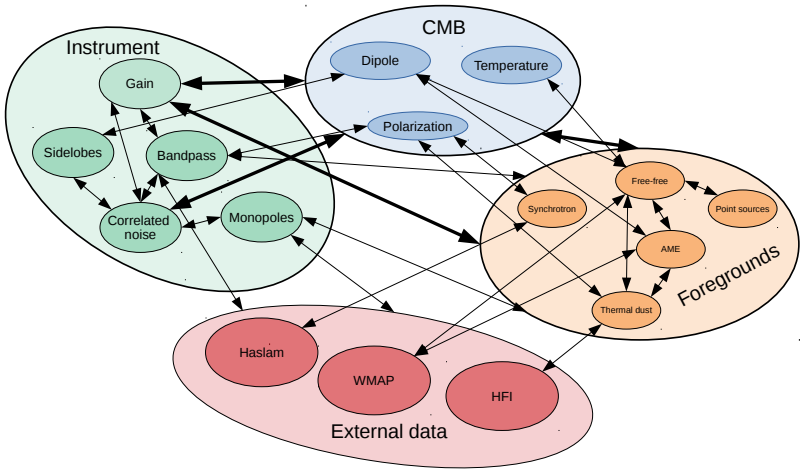

Figure 3.4: Typical parameters needed to model the observed data for a CMB experiment, where the arrows show the interdependencies of each kind of parameters. Parameters considered include the most interested ones describing CMB, those for foregrounds and instrument configuration, and possibly extra parameters for external data when performing a joint analysis. Figure adapted from BeyondPlanck Collaboration I (2023).

each with an amplitude vector s_c, and frequency scaling function $\mathrm{F}_v\left(\beta_c\right)$ that depends on astrophysical spectral parameters β_c. The quantity $g(\nu)$ denotes an overall instrumental calibration factor per frequency channel, and $n_\nu(p)$ indicates instrumental noise. Fig.3.4 shows the schematic overview of the typical parameters considered to model the observed data of modern CMB experiments. Eq.3.13 can be written in a more compact form:

$$\boldsymbol{d}_p = \boldsymbol{A}_p \boldsymbol{s}_p + \boldsymbol{n}_p \,. \tag{3.14}$$

Generally speaking, Eq.3.13 is the starting point for all the parametric methods to do component separation. `Commander` (Eriksen et al., 2004, 2008; Seljebotn et al., 2019; BeyondPlanck Collaboration I, 2023) works in the well-established Bayesian framework to estimate the posterior distribution, $p(\Theta \mid \boldsymbol{d})$, where $\boldsymbol{d}$ indicates all available data and Θ is the combined set of all free parameters. Bayes' theorem reads

$$p(\Theta \mid \boldsymbol{d}) = \frac{p(\boldsymbol{d} \mid \Theta) p(\Theta)}{p(\boldsymbol{d})} \,, \tag{3.15}$$

where $p(\Theta)$ is our prior knowledge for the parameters and $p(\boldsymbol{d} \mid \Theta)$ is called the likelihood.

For a simple model with small number of parameters, the best fit value of each parameter can be obtained through analytical calculation or grid-based, brute-force way.

Nevertheless, this quickly becomes computationally unfeasible since the number of grid points grows exponentially with the number of parameters. For a complicated model such us the one defined in Eq.3.13, we have to resort to smart analysis methods such as Gibbs sampling, which is a powerful variation of traditional MCMC algorithm (BeyondPlanck Collaboration I, 2023). The primary advantage of these techniques is that they invest most of the computing resources around the peak of the posterior, the critical region in parameter space for determining final parameter estimates. In contrast, gridding techniques waste plenty of their time assessing probability densities that are practically zero, which is much less efficient.

Similar to `Commander`, the Maximum Likelihood Estimator (Stompor et al., 2009; Errard et al., 2011; Stompor et al., 2016)starts from Eq.3.14 and estimates $\boldsymbol{s}_p$ from the maximization of the likelihood:

$$-2\log\mathcal{L} = -\sum_p \left(d_p - \mathbf{A}_p s_p\right)^T \mathbf{N}_p^{-1} \left(d_p - \mathbf{A}_p s_p\right) . \tag{3.16}$$

By comparing with `Commander`, the key advantage of this approach lies in their computational efficiency, although at the cost of not achieving the same rigorous propagation of error analysis from performing inference over the full posterior. The most advanced implementation of this method is known as ForeGround BUster (FGBuster) implemented in a Python package[3].

3.4.4 Machine Learning

Besides the traditional component separation methods described above, the application of machine learning techniques to recover the cleaned CMB signals has been proposed in recent years. Wang et al. (2022) built a deep convolutional neural network[4] in order to recover CMB signal from *Planck* temperature data and simulated polarization maps based on the CMB-S4 experiment, which was further tested on the *Planck* polarization data (Yan et al., 2023). As for extra-Galactic foregrounds, Bonjean et al. (2024) performed component separation for the simulated extra-Galactic submillimeter sky, which includes CIB and the SZ effect as the foregrounds for the CMB signal.

3.4.5 Tools to validate the absence of residual foregrounds

It is of great importance to validate that there is no foregrounds present in the cleaned CMB maps. That is why, as we anticipated, any foreground residual is likely to imprinting non-Gaussianity, as the CMB contributes marginally to that. Traditional methods constrain residual foregrounds by leveraging cross-correlations with foreground-dominated maps (e.g., Aluri & Rath, 2016). Measurement of anisotropy are also proposed to characterize the remaining foregrounds (Kamionkowski & Kovetz, 2014; Rotti & Huffenberger, 2016),

[3] `https://fgbuster.github.io/fgbuster/index.html`

[4] The introduction to machine learning terminology will be delivered in Chapter 5.

since the primordial signal is expected to be isotropic, whereas residual foregrounds are not. In Planck Collaboration VII (2020), several additional techniques—including Minkowski functionals, and N-point functions—were adopted to search for deviations from statistical isotropy and homogeneity, which may signal the presence of residual foregrounds. Non-Gaussianity, as we mentioned in Sec.3.3, can also be exploited to trace the foregrounds. For example, von Hausegger et al. (2019) examined how skewness and kurtosis measurements could be employed to constrain residual foreground contamination.

Having now described thoroughly the physical mechanisms of foregrounds, the main aspects of the modeling to simulate them and the methods to do component separation, we are ready now for the discussion about the improvements in foreground modeling that we implemented in this work. In next Chapter, we focus on the newly developed `PySM3` package to simulate foregrounds with improved templates and a new mathematical formalism, while we conclude this Chapter by outlining the latest developments for foreground modeling in the literature.

3.5 Latest Development of Foreground Modeling

In Sec.3.1 we have mentioned the `PySM` setup to simulate foregrounds in principle at any wanted frequency, with further improvements which we will discuss in more details in Chapter 4. There are other methods starting from different perspectives to model the foreground emission in the literature, which we briefly summarize in the rest of this Section.

Clark & Hensley (2019) provides a data driven framework to construct three-dimensional Stokes parameter maps of thermal dust emission in position-position-velocity space using only neutral hydrogen data on the basis that HI is strongly correlated with the dust in the diffuse ISM (Lenz et al., 2017). By integrating over the velocity space, they obtain the polarized dust emission maps over the full sky at a resolution of $16.2'$, corresponding to that of HI data, which are in good agreement with the *Planck* observed 353 GHz dust maps in terms of several physical properties such as the polarization fraction and power spectra, although they do not have a thorough discussion about the non-Gaussianity contained in their maps.

Hervías-Caimapo & Huffenberger (2022) uses a large number of filaments in the distribution of the thermal dust grains together with the large-scale template from data to reproduce the main features of the *Planck* 353 GHz map. These include the power spectrum slopes of intensity and polarization maps, the ratios between EE, BB, and TE power spectra, and the level of non-Gaussianity in the total intensity map, which can be controlled by the density of filaments. When focusing on scales of arcminutes or tens of arcminutes, $\ell = 300-1200$, however, the *Planck* 353 GHz total intensity map has more non-Gaussianity with respect to the generated small scales from the model based on filaments.

Diffuse foreground models are also generated by exploiting magnetohydrodynamic (MHD) simulations. They model the physical processes of the ISM, such as heating and cooling of the gas and the interaction between dust grains and the turbulent magnetic field. The

thermal dust emission can be obtained by integrating the emission of dust grains along the line of sight (Padoan et al., 2001; Planck Collaboration Int. XX, 2015; Kim et al., 2019). The simulated maps are thus non-Gaussian because of the MHD processes and can reach small scales according to the resolution of the MHD simulation itself. However, the MHD simulations can only reproduce the statistical properties of the Galaxy, and thus fail to generate the specific morphology of Galactic foreground emission. Another important limiting factor of MHD simulations is that they are computationally expensive, especially in achieving a high resolution.

An additional technique consists of simulating the foreground by exploiting innovative machine learning algorithms capable of modeling the emission pattern at a high resolution on the basis of the observed one at moderated and low angular scales. We leave more details of this approach to Chapter 5, where we also describe our recent results.

4

Foreground Modeling with PySM3

Let us model the foregrounds!

Starting from this Chapter, we are going to focus on the phenomenological modeling of the foregrounds, trying to extrapolate what we learn from data to the frequencies and angular scales where current data are lacking, with non-Gaussianity being one of the main priority.

Our first step concerns the introduction of the context in which foregrounds are simulated, in terms of the software platform where the modeling is implemented. Since, as it is clear from our previous Chapters, foregrounds are a common challenge to all probes looking at CMB polarization, a single group, with members belonging to most of the collaboration working in the various observations, has been formed in recent years, with the purpose of supporting individual efforts in a centralized and coordinated manner (Zonca et al., 2021; PanEx Collaboration, 2024). The group is known as PanEx GSWG and in this Chapter we describe our contribution to that, culminating in the release of the `PySM3`, which is a public Python package containing the latest developments from `PySM2` (Thorne et al., 2017). The models are implemented in several versions with increasing level of complexity and sophistication, which in `PySM` convention are labeled by numbers following d and s for characterizing the dust and synchrotron, respectively. For instance, `d0` incorporates dust templates from the 2015 *Planck* analysis, applying a fixed spectral index (1.54) and a uniform blackbody temperature (20 Kelvin) across the sky. Nowadays, it is considered as a simplified form for `d1`, which incorporates spatial variations in both temperature and spec-

tral index within the modified blackbody model. Additionally, `d4` extends `d1` by including multiple dust populations, while `d7` accounts for frequency decorrelation of the dust. Similar features characterize the synchrotron models: `s0` features a constant spectral index (-3.1) across the sky, while `s1` incorporates the spectral index large scale modulations as seen by Planck, and `s5` the small scale power identified in radio surveys. For more details of each foreground model in `PySM3` see the related documentation[1].

Our contribution has been focusing on the investigations concerning the levels of non-Gaussianity in the various models, an aspect which will be central also for the next Chapter. After summarizing the new aspects of the `PySM3` package in Sec.4.1, we introduce the basic properties of Minkowski functionals in Sec.4.2 and apply them to measure the non-Gaussianity of dust maps from the new model in `PySM3` in Sec.4.3.

4.1 New aspects comparing with PySM2

In this Section we summarize the new scientific aspects of `PySM3` comparing with `PySM2`. The main aspects concern the generation of templates including simulated data on small, arcminute, angular scales. Specifically, a new formalism, called polarization fraction tensor (PolTens), has been introduced to model Galactic polarization and extrapolate the power to small angular scales up to $\ell_{max} = 16384$. The new procedure is implemented for model `d10` (`s5`) in `PySM3` for dust (synchrotron), respectively. Model `d11` (`s6`) also contain the capability of generating different realizations of foreground obeying the same statistical properties on the fly. A second improvement concerns the study of recent high resolution data products observed at microwaves which are used as new templates, updating those of previous versions. Finally, additional models for different foreground component proposed in the literature are implemented to cover a more complete set of cases, for example `d12` for a 3D model of polarized dust emission with six layers. In the following we give a brief introduction to the first and second points. The `PySM3` also utilizes the latest development in the programming industry for the consideration of faster execution and less CPU memory cost. For more details we refer to PanEx Collaboration (2024).

4.1.1 Polarization Fraction Tensor formalism

The PolTens framework involves the transformation of the Stokes parameters I, Q, and U into their analogues i, q, and u according to

$$\begin{aligned} i &\equiv \frac{1}{2}\ln(I^2 - P^2)\,, \\ q &\equiv \frac{1}{2}\frac{Q}{P}\ln\frac{I+P}{I-P}\,, \\ u &\equiv \frac{1}{2}\frac{U}{P}\ln\frac{I+P}{I-P}\,, \end{aligned} \tag{4.1}$$

[1] https://pysm3.readthedocs.io/en/latest/models.html

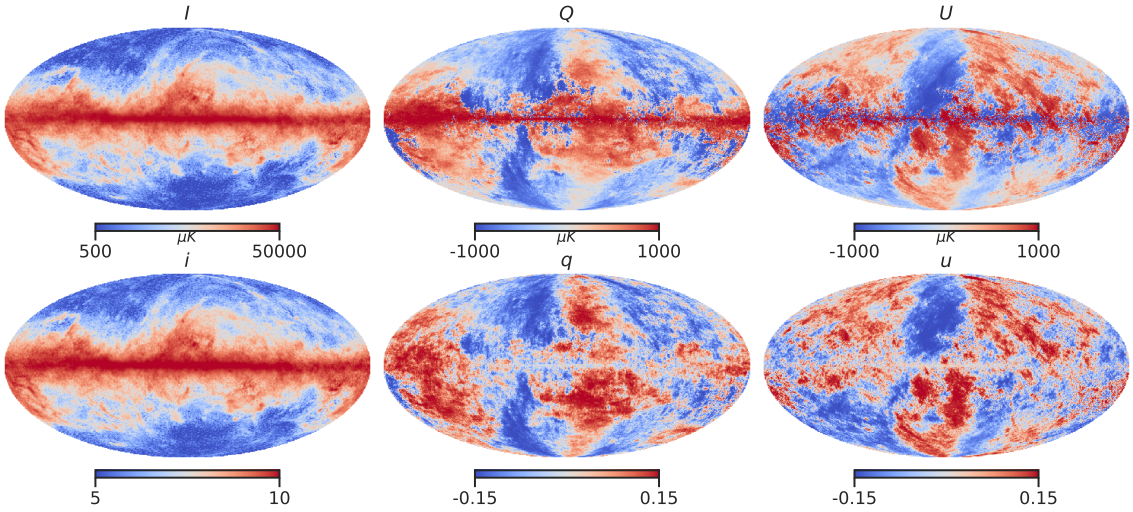

Figure 4.1: Mollview plots of `PySM3 d10` dust maps at 353 GHz in IQU space in the first row and in iqu space in the second row.

where $P \equiv \sqrt{Q^2 + U^2}$ is the commonly defined polarized intensity, independent of coordinate system, and $p \equiv P/I$ is the polarization fraction. For small p, the formulas above reduce to $i \simeq \ln I$, $q \simeq Q/I$, and $u \simeq U/I$ thus motivating the name of this approach. The inverse transformations are

$$\begin{aligned} I &= e^i \cosh \xi \,, \\ Q &= \frac{q}{\xi} e^i \sinh \xi \,, \\ U &= \frac{u}{\xi} e^i \sinh \xi \,, \end{aligned} \tag{4.2}$$

where $\xi \equiv \sqrt{q^2 + u^2}$.

The `PySM3 d10` dust maps in IQU and iqu space are shown in the first and second row of Fig.4.1 respectively. The transformation is clearly non-linear and as we can see the dynamical range of iqu is much smaller than that of IQU maps. Another notable feature is that the Galactic plane of Q and U maps disappear in the qu counterparts, or, we can say intuitively, the maps become "less non-Gaussian" with this transformation. This motivates to generate Gaussian realizations in iqu space which will become non-Gaussian when transformed back into I, Q, and U. That is what the new models (`d9, d10, d11` for dust and `s4, s5 s6` for synchrotron) in `PySM3` actually do in order to generate small-scale fluctuations. We outline the steps applied in these new models as follows.

1. The I, Q, and U templates are transformed into i, q, and u templates via Eq.4.1.

2. These template i, q, and u maps are then low-pass filtered with cut-off multipole $\ell_1 = 100$ in order to yield the large scale maps which are dominated by signal and less affected by instrumental noise.

3. The tt, te, ee, and bb full sky power spectra are calculated from the i, q, and u maps, in analogy with how TT, TE, EE, and BB spectra are computed from I, Q, and U maps.

4. The ℓ-dependence of each spectrum is modeled as a broken power law. To estimate the power spectrum at small scales ($\ell > \ell_1$), a power law is fitted to the spectrum over the range $\ell_0 < \ell < \ell_1$ with a free amplitude and a fixed spectrum index from the literature (Planck Collaboration XI, 2020; Miville-Deschênes et al., 2016). The power is then extrapolated from ℓ_1 to a second pivot scale $\ell_2 = 2000$ using the fitted power law. Finally, for even smaller scales $\ell > \ell_2$, the ee and bb spectra are constructed with the power law index of the tt spectrum, while the te spectrum retains its fit index. This consideration is to ensure the power of polarization is smaller than that of total intensity at small scales. The tb and eb spectra are assumed to be zero for $\ell > \ell_1$.

5. The small-scale i, q, and u maps are synthesized as Gaussian realizations from the constructed tt, te, ee, and bb spectra using the `synfast` routine provided by HEALPix (Górski et al., 2005). and are then high-pass filtered at cut-off multipole ℓ_1.

6. The small scales cannot be added to the large scale maps directly since they do not have the same anisotropy with the large scales. Modulation maps m_i and m_p are constructed for intensity and polarization, respectively, to be multiplied with the small scales to yield the final small-scale maps.

7. Finally, the large-scale and small-scale maps (from Steps 2 and 6, respectively) are summed and transform back to I, Q, and U maps via Eq.4.2.

The methodology allows, in principle, to implement realizations of the signal, which means being capable of getting errors on any application using these templates, from their statistical variation. On the other hand, we notice that, with the exception of the power law inferred from large scales, the generation of Gaussian power on small scales is a pure assumption, which may not account for the right statistics of foregrounds on the corresponding scales.

4.1.2 New templates

`PySM3` also substitutes different data products as templates for the models of dust and synchrotron emissions. For total intensity of dust, *Planck* GNILC 2015 component sep-

arated map at 353 GHz[2] is used, which is free of CIB emission (Planck Collaboration Int. XLVIII, 2016b). For the dust Q and U maps `PySM3` takes the GNILC dust maps[3] from *Planck* Data Release 3 (Planck Collaboration IV, 2020). The reprocessed Haslam 408 MHz map (Remazeilles et al., 2015) is used for total intensity of synchrotron emission, and WMAP K-band (23 GHz) Q and U maps[4] from Data Release 5 is employed as the templates for polarization.

4.2 Minkowski functionals

Minkowski functionals (MFs, Minkowski, 1903) are essential mathematical tools in the analysis of complex spatial structures in digitized images. They provide a quantitative description of the morphology of patterns by characterizing features such as area, boundary length, and topology. In the context of cosmology, these functionals are particularly useful to measure the high-order statistics such as non-Gaussianity (Hikage et al., 2006; Martire et al., 2023; Carones et al., 2024). In the following we give a brief introduction to MFs.

Consider a grey scale image represented by a function $\rho(\mathbf{x})$ on a two-dimensional domain $\Omega \subset \mathbb{R}^2$. The image can be analyzed by considering the excursion sets D_ρ defined as the regions where the image intensity exceeds a certain threshold ρ (see Fig.4.2):

$$D_\rho = \{\mathbf{x} \in \Omega \mid \rho(\mathbf{x}) > \rho\}. \tag{4.3}$$

The set of all the points which have the value of ρ is indicated as ∂D_ρ, which is the boundary of the excursion set.

For an excursion set embedded in d-dimensional Euclidean space, Hadwiger's theorem (Hadwiger, 1957) states that any of its morphological observable is a linear combination of d + 1 MFs, which thus provide a comprehensive set of morphological descriptors for the excursion set. For two-dimensional fields, three kinds of MFs can be built: $\mathcal{V}_0$, $\mathcal{V}_1$, and $\mathcal{V}_2$. They fully describe the statistical properties of the field and represent the covered area ($\mathcal{V}_0$), the boundary length ($\mathcal{V}_1$), and the number difference of connected regions and holes of the image's feature ($\mathcal{V}_2$), as a function of the threshold, ρ (Hadwiger, 1957). Connected regions and holes are topological concepts which can be illustrated in Fig.4.2: in the left image the two white "butterflies" are two connected regions while the central one having two holes inside it. Therefore $\mathcal{V}_0$ and $\mathcal{V}_1$ are geometrical observables while $\mathcal{V}_2$ is a topological observable. We give a more explicit definition of these functionals in the following equation.

[2] http://pla.esac.esa.int/pla/aio/product-action?MAP.MAP_ID=COM_CompMap_Dust-GNILC-F353_2048_R2.00.fits

[3] http://pla.esac.esa.int/pla/aio/product-action?MAP.MAP_ID=COM_CompMap_IQU-thermaldust-gnilc-varres_2048_R3.00.fits

[4] https://lambda.gsfc.nasa.gov/data/map/dr5/skymaps/9yr/raw/wmap_band_iqumap_r9_9yr_K_v5.fits

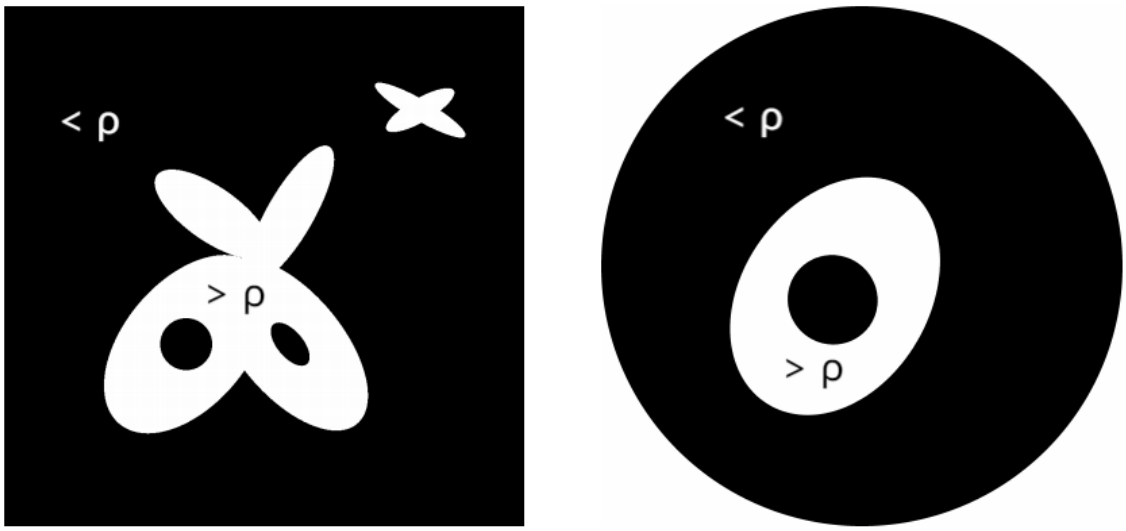

Figure 4.2: Illustration of excursion set, which are the points in the white region, whose values are larger then the threshold, while the black region contains the set of points not belonging the excursion set. Figure adapted from Ganesan (2017).

1. **Area** ($\mathcal{V}_0$): The total area covered by the excursion set is given by

$$\mathcal{V}_0(D_\rho) = \int_{D_\rho} d^2\mathbf{x}\,. \tag{4.4}$$

2. **Boundary Length** ($\mathcal{V}_1$): The boundary total length of the excursion set is defined as

$$\mathcal{V}_1(D_\rho) = \frac{1}{2\pi}\int_{\partial D_\rho} ds\,, \tag{4.5}$$

where ∂D_ρ denotes the boundary of the excursion set, and ds is the line element along this boundary.

3. **Euler Characteristic** ($\mathcal{V}_2$): The Euler characteristic is a topological invariant that provides information about the connectivity of the structure. It is defined as

$$\mathcal{V}_2(D_\rho) = \frac{1}{2\pi}\int_{\partial D_\rho} \kappa(s) ds\,, \tag{4.6}$$

where $\kappa(s)$ is the curvature of the boundary ∂D_ρ. The Euler characteristic counts the number of connected components minus the number of holes in the structure.

Implementation of algorithms in real case to calculate the MFs is a non-trivial task. In practice a further discretization is needed for the already discretized field, like the observed maps on the sky.

For flat 2-D images, Mantz et al. (2008) extended the use of MFs to the analysis of noisy experimental grey-scale images by introducing a novel real-space technique based on these functionals. Their method, based on the *marching square algorithm* (Lorensen & Cline, 1987), allows for accurate computation of MFs in digitized images by exploiting weighted side lengths for pixels. First, squares with different length are used to cover the whole field considered. Then, each corner of the square is adjusted according to the threshold value, depending on whether it is inside the excursion set or not. During this step squares become polygons to further constrain the boundary of the excursion set. Once these polygons are constructed, MFs can be calculated from these polygons by simple geometry. This approach is particularly effective in capturing the true boundary lengths in the images, which is crucial for analyzing surface topologies.

On the sphere with HEALPix pixelization scheme, Grewal et al. (2022a) presented a formalism to efficiently get the MFs, which can be written as

$$\begin{aligned}
\mathcal{V}_0(\rho_j) &= \frac{1}{N}\sum_i \Theta\left(\alpha(\mathbf{x}_i) - \rho_j\right), \\
\mathcal{V}_1(\rho_j) &= \frac{1}{4N}\sum_i \Delta\left(\alpha(\mathbf{x}_i) - \rho_j\right)\sqrt{\alpha_\phi^2 + \alpha_\theta^2}, \\
\mathcal{V}_2(\rho_j) &= \frac{1}{2\pi N}\sum_i \Delta\left(\alpha(\mathrm{x}_i) - \rho_j\right)\left(\frac{2\alpha_\phi\alpha_\theta\alpha_{\phi\theta} - \alpha_\phi^2\alpha_{\theta\theta} - \alpha_\theta^2\alpha_{\phi\phi}}{\alpha_\phi^2 + \alpha_\theta^2}\right),
\end{aligned} \tag{4.7}$$

where Θ is the Heaviside step function, $\alpha(\mathbf{x}_i)$ is the value for pixel $\mathbf{x}_i$, Δ is 1 when $\alpha(\mathbf{x}_i)$ is between ρ_j and ρ_{j+1}, N is the total number of pixels. ϕ and θ are the related polar coordinates and $\alpha_\phi, \alpha_\theta, \alpha_{\phi\theta}, \alpha_{\theta\theta}$, and $\alpha_{\phi\phi}$ are derivatives of the field, which can be calculated using the routine provided by HEALPix (Górski et al., 2005; Zonca et al., 2019).

4.3 Measuring the non-Gaussianity in the new dust maps

In this Section, we quantify the level of non-Gaussianity in the smallscale dust emission generated through PolTens using the simulations from `PySM3` dust model `d10`. The small-scale fluctuations in the new synchrotron emission maps from `PySM3` are constructed following the same algorithm, we expect those maps to show similar levels of non-Gaussianity on the scales where the pattern is simulated with the same procedure.

We use MFs to compare the small-scale structure in `d10` to those of two other sets of maps: (i) maps where the small-scale structures are fully Gaussian and isotropic and (ii) maps where the small-scale structures are Gaussian but modulated across the sky. As

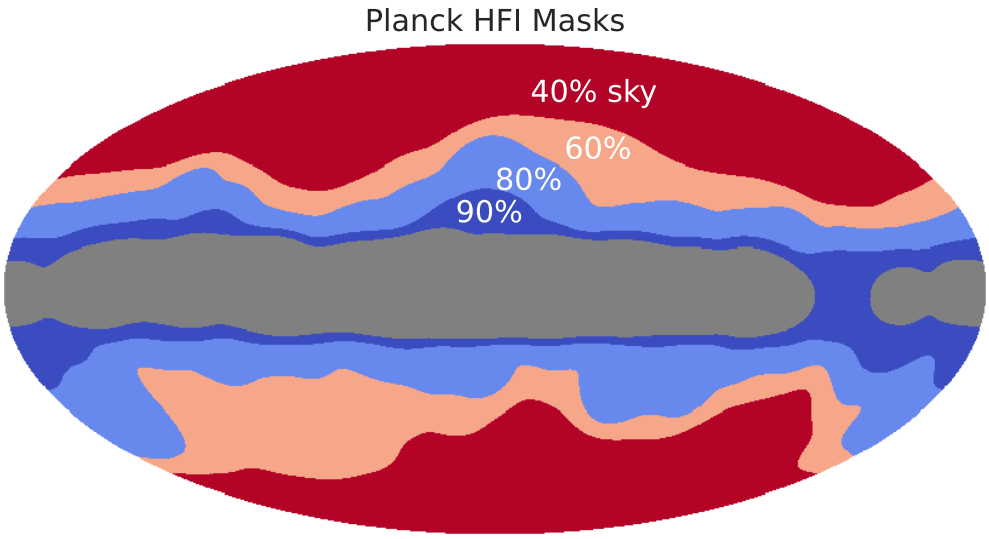

Figure 4.3: *Planck* High Frequency Instrument (HFI) Masks from Planck Legacy Archive for different sky fractions.

described in Section 4.1.1, the small-scale structures in the `d10` model are generated as a Gaussian random field in i, q and u, and are multiplied by m_i and m_p modulation maps before they are coadded to the large scale maps and transformed back into I, Q and U. We want to understand the impact of this effective modulation on the MFs, and therefore construct a set of maps that are modulated versions of Gaussian-random field maps. This allows to disentangle any non-Gaussianity generated through the modulation from the potential non-Gaussianity introduced due to the polarization fraction tensor transformation.

The first set of maps is built according to the following procedure.

1. We first fit power laws to the TT, EE, BB power spectra in the multipole range $[800, 2000]$ calculated from the `d10` maps on the `GAL097` mask.

2. In order to retain only the small scales, we apply a high pass filter to the fitted power law power spectra with $\ell_{cut} = 200$ for intensity and polarization maps, and then generate full sky realizations of these filtered power spectra (with $\ell_{max} = 4096$) with the `synfast` routine.

3. The generated Gaussian isotropic small scales are added to the large-scale dust template to form the first set of maps.

For the second set, we need to mimic the effective modulation of d10 maps in IQU quantities. We use the following procedure.

1. We generate modulation maps in the same way as done in iqu space, except that here we implement them directly in IQU, therefore obtaining m_I and m_P for total intensity and polarization.

2. We multiply these modulation maps with maps of Gaussian isotropic small scales (generated as for the first set of Gaussian isotropic maps, as described in steps 1 and 2 above) and coadd them with the large scale dust template.

3. We compare the power spectra of these maps with those of d10 on four different individual sky-fraction masks: GAL40, 60, 80, 90, as shown in Fig.4.3. We note that these masks are required solely for the generation of the modulation maps, with the exception of GAL80, which is also employed in the subsequent analysis presented in this Section.

4. We fine tune the m_I and m_P modulation maps, through multiplication factors in the sky regions defined by the non-overlapping area among the above five masks. For each non-overlapping area we only consider the part which is not overlapping among masks, such as the green region in Fig.4.3, showing the additional coverage of GAL60 compared with GAL40 which we indicate as GAL60-40. The multiplication factors for the non-overlapping regions are {GAL97-90, GAL90-80, GAL80-60, GAL60-40, GAL40} = {2.32, 1.20, 0.38, 0.78, 2.47}, {6.32, 2.50, 1.46, 1.51, 2.60} for temperature and polarization maps, respectively. These factors are applied to ensure that the power spectra of modulated Gaussian small scales computed on the individual sky-fraction masks are as close as possible to the d10 map, which can be shown in Fig.4.4.

We thus consider three sets of maps with different coadded small scales: PySM3 model d10, a map with purely Gaussian small-scale structure, and a map with modulated Gaussian small-scale structure. We apply a high-pass filter with $[\ell_{min}, \ell_{max}] = [200, 2048]$, to retain only the small scales of these maps, which we will refer to as poltens-ss, Gaussian-ss, and Gaussian-mod-ss, respectively. We calculate the MFs both on the sphere and in several selected regions of the sky projected into a Cartesian projection.

4.3.1 Minkowski Functionals on the sphere

Following the algorithm by Grewal et al. (2022a), we calculate the MFs for the three Q maps on the sphere, i.e., in HEALPix format, with a GAL080 mask, which masks out the Galactic plane. We first normalize the maps by dividing each map by its standard deviation, and compute the MFs for iso-intensity contours in the range $[-3, 3]$ (Figure 4.5). The MFs of the corresponding U maps look very similar to Q maps and are not shown here.

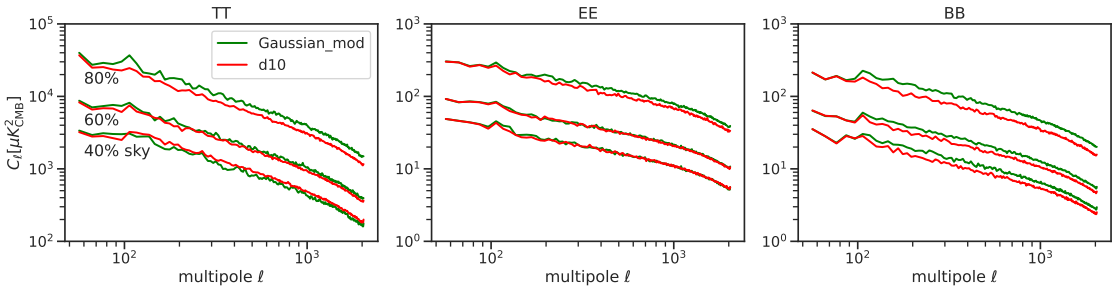

Figure 4.4: Power spectra of `PySM3 d10` map and modulated Gaussian map described as above, in red and green lines respectively. Three masks, namely `GAL040, GAL060, GAL080` are considered. The agreement of these two sets of maps of power spectra on different sky fraction masks indicates that they have similar anisotropies, up to the sky masks considered.

Figure 4.5 shows that when averaging over a large sky area, the MFs of `Gaussian-mod-ss` and `poltens-ss` are almost identical, while the MFs of `Gaussian-ss` differ substantially. The difference in MFs between `poltens-ss` and `Gaussian-ss` indicates the existence of non-Gaussianity in `poltens-ss`, but the similarity between `poltens-ss` and `Gaussian-mod-ss` demonstrates that the non-Gaussianity in `poltens-ss` comes from the anisotropy in the maps, which originates from the modulation, rather than from the polarization fraction tensor transformation. With the exception of the issue which we report in the next sub-Section, this is an important point, showing that, even if PolTens represent a progress towards a comprehensive rendering of foregrounds, including a small-scale power according to the power spectra observed in the large one, the non-Gaussian pattern would have to be evaluated by other methods, bringing to the small scales not only the scaling of power in the angular domain, but also non-Gaussian properties. We come back to this point in the summary, and in the next Chapter.

4.3.2 Minkowski Functionals on small regions

We now consider a region centered at $(l, b) = (-15°, 45°)$ with an extension corresponding to $20° \times 20°$ in order to determine whether significant differences in the MFs between `Gaussian-mod-ss` and `poltens-ss` sets of maps exist in small regions of sky. Those maps are shown in Figure 4.6. We can see by eye that `poltens-ss` contains structure that is not present in the `Gaussian-mod-ss` maps. We calculate the MFs of these small-scale maps, following Mantz et al. (2008) for the calculation of MFs for a square patch. Before the calculation, we also rescale all the small scales linearly to be in the range [-1, 1], using the *minmax* scheme.

Figure 4.7 shows the MFs of the `Gaussian-mod-ss` and `poltens-ss` maps presented

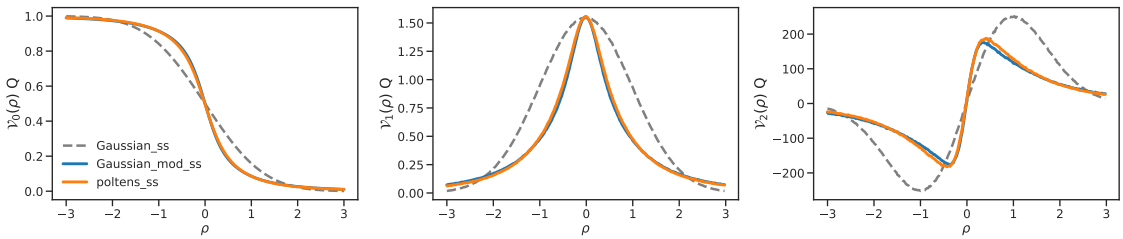

Figure 4.5: MFs for the small scales of three sets of maps on the sphere with `GAL080` mask. The large scales are filtered out by excluding multipoles $\ell < 200$ in the maps, and we choose $\ell_{\rm max} = 2048$ when obtaining the small scales. We show the MFs as a function of threshold ρ, for `Gaussian-mod-ss` in blue, `poltens-ss` in orange and `Gaussian-ss` in dashed gray.

in Figure 4.6. In contrast with the large-area results presented in Figure 4.5, in this case we do measure a departure of the `poltens-ss` MFs from the `Gaussian-mod-ss` ones. This means that the polarization fraction tensor transformation introduced non-Gaussian small-scale structure, distinct from pure modulation effects, that is detectable on small sky regions. This level of non-Gaussianity, however, does not rely on statistical properties of foregrounds, and is sub-dominant with respect to the effect caused by modulation, when larger sky area are examined.

4.4 Summary

Foreground simulations serve as an essential test in the context of CMB observations. Pipelines such as component separation and lensing reconstruction must incorporate foreground simulations as a key prerequisite. `PySM` is a community-driven effort that provides these simulations, which are widely used not only within the CMB community but also by researchers in other fields interested in Galactic foregrounds, such as those working in the 21cm domain.

In this Chapter, we presented the latest development of the package, `PySM3`, which introduces a variety of new models for different foreground components. This includes a novel model based on the polarization fraction tensor framework, as well as several existing models from the literature.

We focused on quantifying the non-Gaussianity in the small-scale structures of the dust maps generated by the `d10` model, using MFs in order to measure the degree of non-Gaussianity both on the full-sky maps with the Galactic plane masked and within a selected sky patch. Since the `d10` model incorporates not only the PolTens framework but also a modulation of small scales in the *iqu* space, we constructed an additional set of

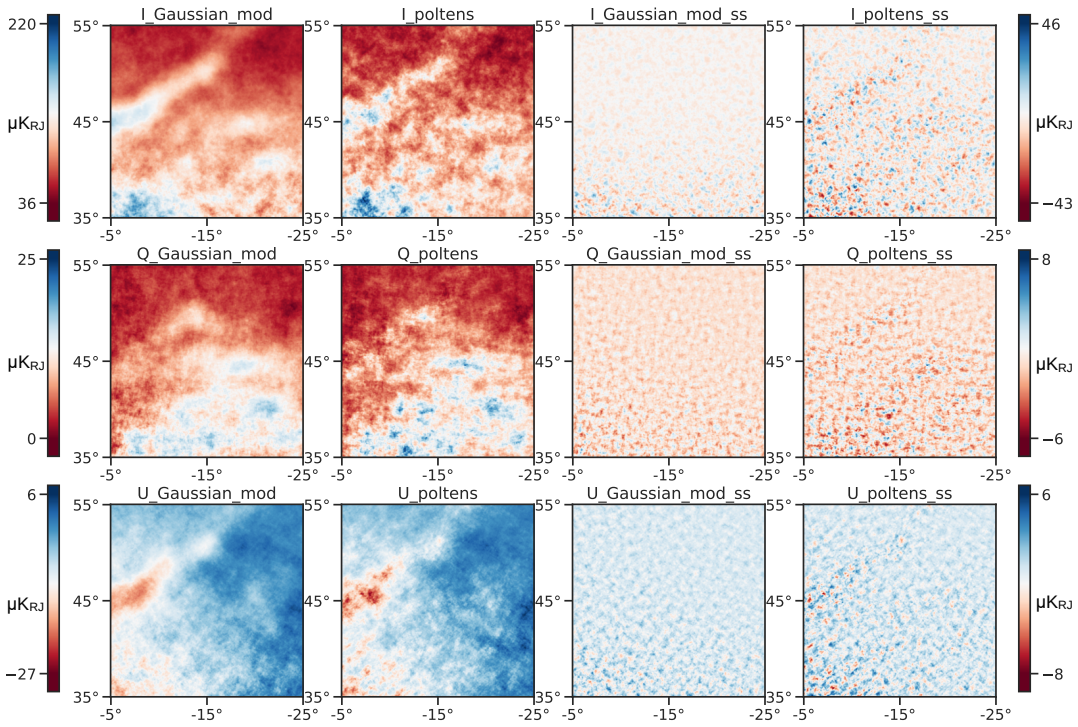

Figure 4.6: We show the detailed plots in the selected patch at the center $(l, b) = (-15°, 45°)$, which are, from left to right, the final map with `Gaussian-mod-ss`, final map with `poltens-ss` (i.e., `d10` map), `Gaussian-mod-ss` only map and `poltens-ss` only map. From top to bottom is for I, Q and U respectively. The color bar on the left indicates the pixel values in the leftmost two columns in the units of μK_{RJ} and the color bar on the right is for the last two columns.

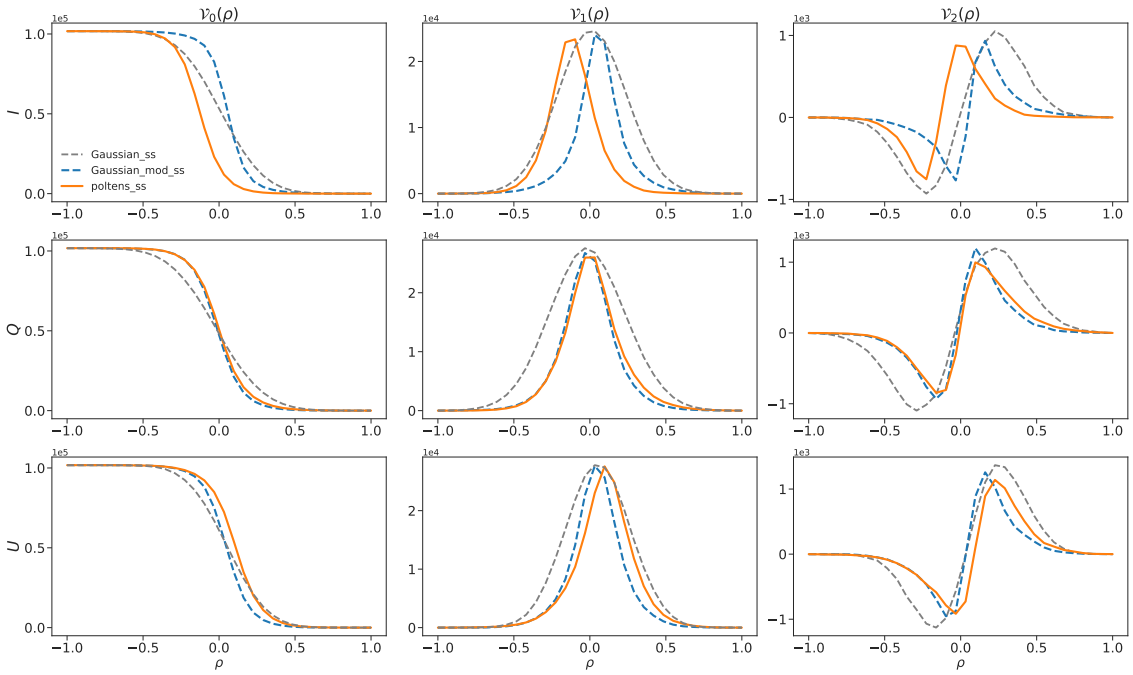

Figure 4.7: MFs as a function of the threshold ρ for the one realization of I, Q and U small scales in the patch with center of $(l, b) = (-15°, 45°)$ in Galactic coordinates. Each row shows three kinds of MFs. The blue dotted one is for `Gaussian-mod-ss` while the orange solid one is from `poltens-ss`. We also show the `Gaussian-ss` in dashed gray line as a comparison.

Gaussian maps with identical modulation to the `d10` maps to isolate the contributions to non-Gaussianity from the PolTens framework and the modulation. Purely Gaussian maps were also generated for comparison.

By comparing these three sets of dust maps, we found that the PolTens framework does introduce non-Gaussianity in small sky patches, with the effect varying across regions. However, when averaged over large sky areas, the level of non-Gaussianity remains insignificant compared with the Gaussian modulated small scales. We leave more discussions about the results in the Conclusions.

5

Simulating Stochastic Non-Gaussian Foregrounds with Machine Learning

Let machine learn the foregrounds!

Recently, machine learning techniques, in particular neural networks, have been exploited to simulate foregrounds with increasing complexity. The ForSE model introduced by Krachmalnicoff & Puglisi (2021) (hereafter KP2021) is able to generate small scales, up to $12'$, starting from the low-resolution polarized dust observations at $80'$. It utilizes a GAN, which is trained to inject small-scale features with statistical properties like the ones observed at a high resolution in the intensity maps.

Neural networks have, in principle, the capability of learning statistics at any order. Therefore, in our context, the perspective is to get high resolution maps where the non-Gaussianity of the large scales is faithfully reproduced. In this Chapter, we focus on the ForSE approach and present the version which we produced, ForSE+, focusing mainly on two perspectives: (i) Producing dust polarization maps at $3'$ resolution, which is vital for achieving foreground maps where the signal is available at all angular scales covered by CMB experiments, necessary in particular for checking the stability of lensing reconstruction and de-lensing algorithms in CMB observations, (ii) Stochastically generating multiple realizations of small-scale features, which is most important in order to estimate

the uncertainty associated with foreground variations.

In Sec.5.1 we introduce some basics of neural networks. After that we summarize the first version of the ForSE algorithm and present the extension and methodology used to achieve the new version operating at arcminute scale in Sec.5.2. In Sec.5.3, we describe the pre-processing, training, and post-processing of the new model and also present our validation procedure. In Section 5.4, full-sky maps are presented and compared with maps from the latest version of `PySM3` package. This Chapter is based on Yao et al. (2024).

Additional uses of deep generative models for dust simulations exist in the literature. For example, GANs are also employed in Aylor et al. (2021) to generate simulated total intensity maps from the observed *Planck* GNILC map at 353 GHz. Irfan (2023) used CNNs to obtain a full-sky high-resolution Galactic synchrotron spectral index map. Other common generative models, such as variational autoencoders (Thorne et al., 2021) or diffusion models (Mudur & Finkbeiner, 2022; Heurtel-Depeiges et al., 2023), are also used.

5.1 Basics of Neural Networks

Belonging to a subset of machine learning, NN dates back to 1940's when neurophysiologist tried to describe how neurons in human brain might work. Rosenblatt (1958) implemented the first NN, called *perceptron* which was invented by McCulloch & Pitts (1943) to study the biological systems. In late 1980s, LeCun et al. (1989) pioneered the implementation of CNNs that automatically learn spatial hierarchies of features, making them particularly effective for image recognition tasks. NN gained significant attention and became a prominent research topic in the past decades, as evidenced by the rapidly growing body of related literature in all kinds of scientific fields, including astronomy. This occurrence in popularity is primarily driven by the ever-increasing availability of data, coupled with advancements in technology and computational power. In particular, DL, which has multiple layers between the input and output layers, has become the fundamental framework for modern networks to solve complicated problems. In 2014, GANs were proposed by (Goodfellow et al., 2014) to generate new data samples that resemble a given dataset and soon brought up numerous applications, including Deep Convolutional GAN, which is used in our work in this Chapter. In 2024, machine learning and NN won the Nobel Prize in Physics 2024 for the pioneers' work to train NN using physics[1].

Simply speaking, NN is a function of input, with numerous free parameters. Applying NN to solve problems can be divided into three parts: preparing data, designing architecture of NN, and fit the NN to the data. While first part is highly case-dependent, the latter two parts usually consist of similar components, like neurons, layers, loss functions, ..., which we introduce in the next two Sub-Sections respectively. There are numerous excellent online lectures on neural networks, such as those by Andrew Ng[2] and Hung-yi

[1] https://www.nobelprize.org/prizes/physics/2024/press-release/
[2] https://www.andrewng.org/courses/

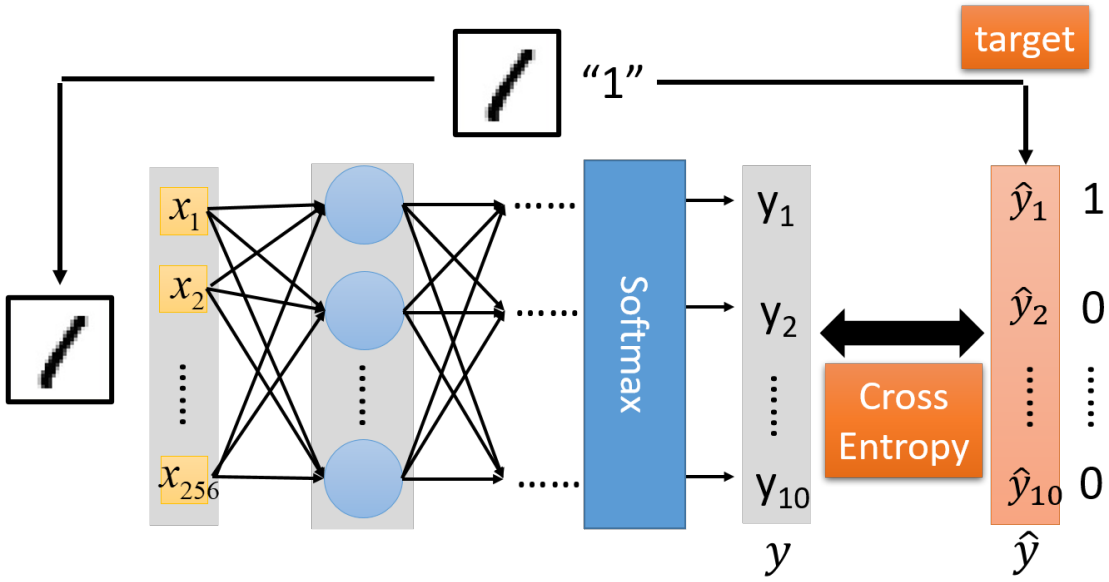

Figure 5.1: Illustration of a neural network architecture used for classification tasks. Each vertical block is called a *layer* of NN. The input image is flattened into feature vectors with 256 pixels and fed into the network. The next layers (hidden layers) consists of neurons (blue circles) that apply activation functions to the weighted sum of inputs, where black arrows represent the *weight* connected to each neuron. The output layer generates raw predictions, which are converted into probabilities using the Softmax function. The Cross Entropy loss function is then used to measure the difference between the predicted probabilities and the target labels, guiding the training process.

Lee[3]. We refer the interested readers to those resources for details, also see reviews like LeCun et al. (2015); Alzubaidi et al. (2021).

5.1.1 Structures of NN

Fig.5.1 shows the basic structure of a fully-connected neural network to classify the number in the input image, which we use as an example to briefly explain each part of NN structures in the following.

1. **Input Layer**: Depending on the design of NN, the input layer can vary for practical cases, such as three dimensions for three RGB channels of a colored image. Here in this example, the leftmost component of the figure shows an image of a handwritten

[3] https://speech.ee.ntu.edu.tw/~hylee/ml/2023-spring.php

digit (e.g., '1'), represented as 256 pixel values. This image is flattened into a vector of features $(x_1, x_2, \ldots, x_{256})$, before given to the neural network.

2. **Neurons (Hidden Layer)**: The hidden layer contains neurons represented by blue circles. Each neuron receives input from the previous layer (input layer) and computes a weighted sum of the inputs, often adding a bias term. The connections between input and hidden neurons are shown as arrows. This network belongs to full-connected ones, since every neuron in one layer connects to every neuron in next layers. Advanced versions of connections exist such as CNN, which share the weights among neurons for a particular feature in the image, thus greatly reduce the total number of parameters needed to fit.

3. **Activation Function**: After computing the weighted sum, each neuron applies an non-linear activation function (not explicitly shown in the figure but implied by the neural structure). Common activation functions include ReLU, sigmoid, or tanh, which introduce non-linearity into the model, allowing it to learn complex patterns.

4. **Output Layer**: The output layer of this example is represented by a set of 10 values, $(y_1, y_2, \ldots, y_{10})$, which are the raw predictions before applying the activation function. These outputs correspond to the probability scores for each class (e.g., digits 0-9 in a digit classification task).

5. **Softmax Function**: The Softmax layer transforms the raw outputs into probabilities by normalizing them, ensuring that the sum of all probabilities is equal to 1 and the ideal output of this NN is $y_1 = 1, y_i = 0$ for i $\neq 1$. This step is crucial in multi-class classification problems, providing interpretable outputs.

6. **Loss Function**: The loss function measures the difference between the predicted probabilities $(\hat{y}_1, \hat{y}_2, \ldots, \hat{y}_{10})$ and the actual target labels. This function is used to quantify the model's prediction error, guiding the optimization process during training by minimizing this error. The choice of loss function depends on the nature of the task and the type of output generated by the network. Common loss functions include Mean Squared Error for regression tasks and Cross Entropy Loss for classification problems.

5.1.2 Training Process of NN

The parameters fitting process, or *training* of NN, involves iteratively adjusting the model's parameters to minimize the error between the predicted outputs and the actual targets. This process relies on key components such as the backpropagation algorithm and the use of training, validation, and testing datasets. Below is a detailed introduction to each of these components and their roles in training NN.

1. **Training, Validation, and Testing Sets**

- **Training Set**: This is the primary dataset used to train the NN. It consists of input-output pairs that the model uses to learn patterns and relationships. The training set allows the network to adjust its weights through multiple iterations to minimize prediction errors.
- **Validation Set**: *During* training, a separate validation set is used to evaluate the model's performance. It helps in tuning hyperparameters (e.g., learning rate, number of layers) and prevents overfitting (where the model performs well on the training data but poorly on unseen data) or underfitting (where the model fails to capture the underlying patterns) by monitoring how well the model generalizes to unseen data.
- **Testing Set**: *After* training is complete, the testing set is used to assess the final model's performance. This set contains data that the model has never seen before and provides an unbiased evaluation of its predictive capabilities.

2. **Backpropagation**

   Backpropagation is a crucial algorithm used for training NN, enabling efficient computation of the gradient of the loss function with respect to each weight in the network. It consists of two main steps:

   - **Forward Pass**: In this step, input data is passed through the network to generate predicted outputs. The loss function then computes the error between the predictions and the actual targets.
   - **Backward Pass (Gradient Computation)**: The error is propagated backward through the network using the chain rule of calculus. This process computes the gradients of the loss function with respect to each weight, indicating how much each weight contributes to the overall error.

3. **Optimization and Model Training**

   The optimization process involves updating the weights of the network iteratively using the gradients computed by backpropagation. Common optimization algorithms are Stochastic Gradient Descent and Adam (Kingma & Ba, 2014), which adjust the weights in the direction that minimizes the loss. This step is repeated over multiple epochs, where each epoch refers to one complete pass through the entire training dataset.

In summary, the training process of NN is a systematic approach involving the adjustment of model parameters to minimize the loss function. By leveraging training, validation, and testing sets, the process ensures that the model learns meaningful patterns while maintaining its ability to generalize to new data. Backpropagation plays a pivotal role in this process by enabling the efficient computation of gradients, which guide the optimization of the model during training.

5.1.3 Generative Adversarial Networks

GANs are a particular family of networks (Goodfellow et al., 2014) whose characteristic feature is to be composed of two sub-networks called Generator (G) and Discriminator (D), which are trained to compete against each other. In practice, the goal of G is to produce new images that are compared by D with a set of real images that are the training set. Once the training of the two sub-networks is done in an adversarial way, G is able to produce images that have the same statistical properties as those belonging to the training set, in such a way that mock and real images are no longer distinguishable by D.

5.2 From ForSE to ForSE+

In this Section, we start by briefly reviewing the basic structure and assumptions of the ForSE algorithm presented in KP2021. We then introduce our new version of the code, ForSE+, which allows one to generate maps of the thermal dust emission with non-Gaussian structures at $3'$ angular resolution, in both a deterministic and a stochastic way.

5.2.1 Review of the ForSE model: From $80'$ to $12'$

As has already been mentioned, the ForSE model is based on GANs and allows one to produce non-Gaussian full-sky maps of polarized thermal dust emission at an angular resolution of $12'$ from low-resolution *Planck* observations at $80'$.

The structure of the GAN that was used in KP2021 and inherited in this work is shown in Fig.5.2. In the ForSE implementation, the input to G are images at a low resolution ($80'$) of the thermal dust emission observed by the *Planck* satellite and processed through the GNILC method[4] (Planck Collaboration IV, 2020). The output of G are small-scale features at $12'$, which are then compared by D with real observations in total intensity at the same angular resolution. We note that different training is performed for total intensity and Stokes Q and U maps, but always having as the training set images of small scales $\tilde{m}_{12'}^{I,20^\circ}$ in total intensity. KP2021 therefore assumed that thermal dust statistical properties of small scales in polarization are the same as for Stokes I maps. We also rely on that assumption in this work.

In KP2021 and in this work, the following definition of "small scales" is used. Let M_{TOT} be a foreground map at a given angular resolution, which can be seen as the sum of two maps containing, respectively, only large- and small-scale structures:

$$M_{TOT} = M_{LS} + M_{SS}\,. \tag{5.1}$$

Assuming that the map encoding small-scale features, M_{SS}, is modulated by the large scales, M_{LS} – that is, $M_{SS} = M_{LS} \cdot m_{ss}$ – we have

$$M_{TOT} = M_{LS} + M_{LS} \cdot m_{ss} = M_{LS} \cdot \tilde{m}_{ss}\,, \tag{5.2}$$

[4] http://pla.esac.esa.int/pla/aio/product-action?MAP.MAP_ID=COM_CompMap_IQU-thermaldust-gnilc-unires_2048_R3.00.fits

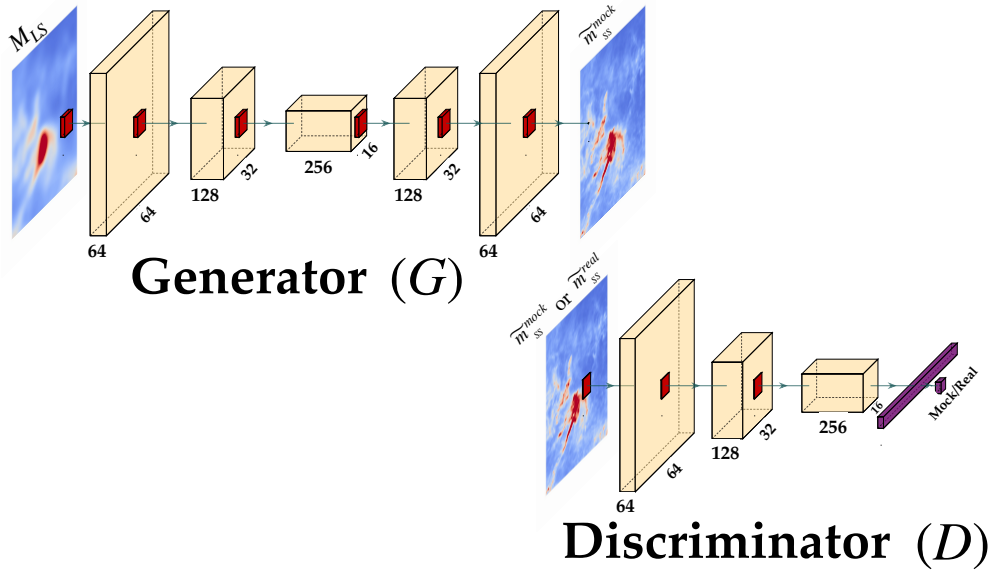

Figure 5.2: GAN architecture used in this work which, composed by two models called Generator and Discriminator. The figure has been adapted from Krachmalnicoff & Puglisi (2021)

where $\tilde{m}_{ss} = m_{ss} + 1$ represents the small-scale map generated by network G, having as an input M_{LS}.

Although there exist NNs designed to work on the sphere (Krachmalnicoff & Tomasi, 2019), our GAN deals with flat two-dimensional images. For this reason, we had to project the input maps onto flat patches, and project output patches back onto the sphere, after the application of the trained GAN model. We used the same projection strategy as that described in the appendix of KP2021, which divides the GNILC thermal dust Stokes Q and U maps at $80'$ with $N_{side} = 2048$ (in the HEALPix format) into 174 square patches that have 320×320 pixels and a physical side length of $20°$. We note that this projection on flat patches and reprojection on the sphere can introduce distortions in the final full-sky map. In order to mitigate this effect, the flat patches overlap each other. We estimate that the final level of distortion induced by our procedure is always less than 7% of the signal (around 2% on average).

From now on we will use $\tilde{m}_{z'}^{X,y^\circ}$ and $M_{z'}^{X,y^\circ}$ to refer to the small-scale (output of the network) and large-scale (input of the network) patches, respectively, where $X = I/Q/U$ defines the Stokes parameters, y° the physical dimension of the patch in degrees, and z' its angular resolution in arcminutes.

The training procedure, input maps, and output validation of the ForSE model are fully described in KP2021.

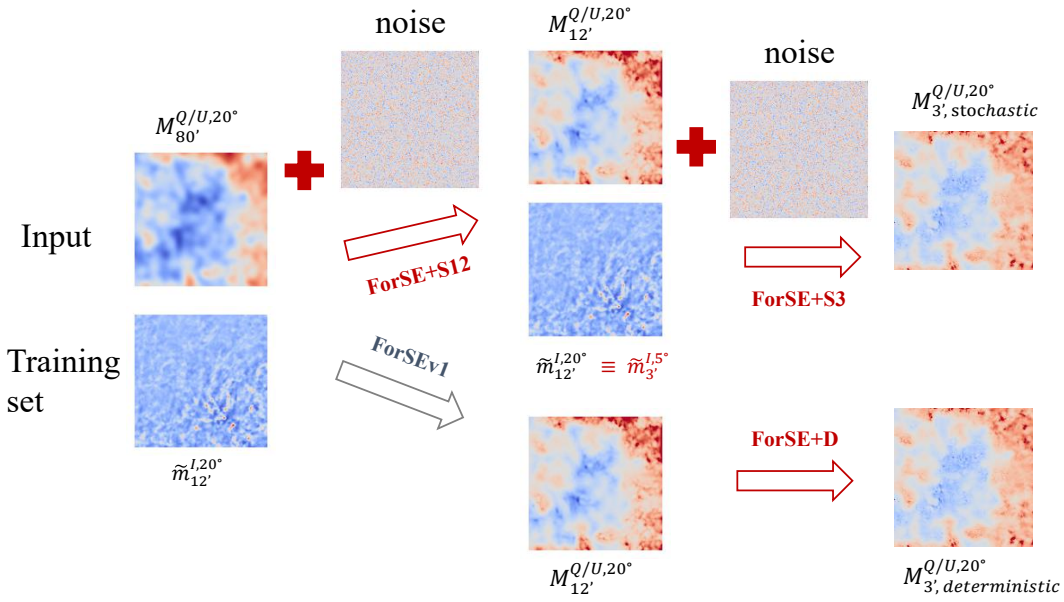

Figure 5.3: Model structures in ForSE (KP2021) and ForSE+ (this work). ForSE is designed to achieve a $12'$ resolution from input large scales at $80'$. We have three kinds of newly trained models here: ForSE+S12 and ForSE+S3 to produce stochastic maps at $12'$ and $3'$, and ForSE+D to generate a deterministic map at $3'$. The output, $M^{Q/U,20^\circ}_{12'}$, from ForSE and ForSE+S12 are the input to ForSE+D and ForSE+S3 to get deterministic and stochastic small scales at $3'$, respectively.

5.2.2 ForSE+: Producing non-Gaussian dust maps at $3'$

In this work, we implement ForSE+, an updated version of the ForSE code and its training procedure, with the following two objectives.

1. Allowing the generation of full sky polarization maps with non-Gaussian features at an enhanced resolution of $3'$.

2. Starting from the same low-resolution maps, to generate multiple realizations of stochastic small scales that still have the correct non-Gaussian statistical properties.

In the Sections below, we explain the assumptions and methodology used to achieve these two goals. Figure 5.3 sketches the input and output of the new ForSE+ models and in Table 5.1 we summarize the new models trained in this work.

In order to incorporate these extensions, we re-implemented the same GAN architecture

Model	Description (Output)	Input
ForSE	KP2021 version to simulate deterministic thermal dust emission maps at $12'$	*Planck* GNILC maps at $80'$ (*map*1)
ForSE+S12	new model to simulate stochastic thermal dust emission at $12'$	*map*1 plus random component
ForSE+D	new model to simulate deterministic thermal dust emission maps at $3'$	Maps at $20'$, smoothed from ForSE $12'$ maps (*map*2)
ForSE+S3	new model to simulate stochastic thermal dust emission maps at $3'$	*map*2 plus random component

Table 5.1: Summary of three newly trained models in this work and the first version of the model proposed in KP2021.

as for the ForSE model using the new Tensorflow[5] framework (version 2.6.0), and we performed additional fine-tuning steps of some hyper parameters of the networks to improve our results.

5.2.2.1 Scale invariance assumption

The first goal of our implementation of ForSE+ is to generate a map of polarized dust emission with non-Gaussian features at arcminute angular scales. As we anticipated, this is crucial to be able to perform component separation with simulated foreground templates where power and non-Gaussianity is distributed on all scales, as realistically as possible, in particular for checking the stability of the extraction of the CMB B-mode lensing signals, which peak at these scales. In order to achieve this, we need to find a way to overcome the current limitation in the observational data. As a matter of fact, in order to train our GANs we can only rely on a training set composed of 350 patches, with dimensions of $20^\circ \times 20^\circ$ and 320×320 pixels, at an angular resolution of $12'$, taken from the total intensity GNILC *Planck* map at 353 GHz, described in KP2021. No other observations of thermal dust emission at a higher angular resolution in a portion of the sky large enough to be used as training set are available.

The idea to circumvent this restriction and still be able to reach a resolution higher than $12'$, even in the absence of a proper training set, is to make a scale-invariance assumption, applying our GAN model in an iterative way. In practice, our set of training squared patches with dimensions of $20^\circ \times 20^\circ$ and a resolution of $12'$ can equally be treated as having dimensions of $5^\circ \times 5^\circ$ and resolution of $3'$, since the network does not have a sense of physical units and is only sensitive to the ratio between the dimension of the patch and

[5] https://www.tensorflow.org

its angular resolution (i.e., $\tilde{m}^{I,20^\circ}_{12'} \equiv \tilde{m}^{I,5^\circ}_{3'}$). In this way, the same dataset used to train the first version of ForSE in KP2021 can be used to train a new GAN model. This model takes the output of the first iteration of the code as input and generates non-Gaussian scales at $3'$. As it has been mentioned, this implies that we are assuming scale invariance for the statistical properties of dust emission; that is, scales at $12'$ have the same properties as those at $3'$. This assumption is justified by the fact that current observations of the dust polarization power spectra shows that they can, at the first order, be approximated as a power law as a function of the angular scales (Planck Collaboration XI, 2020).

Additional pre- and post-processing of the input patches (including upsampling, smoothing, and the sub-division of patches) is needed to train the GAN in the correct way and to be able to restore full-sky maps, as is described in Section 5.3.2.1.

5.2.2.2 Stochasticity

Our second goal is to produce different realizations of the non-Gaussian small-scale structures. This is important in order to estimate the variance of the signal we are simulating as well as the correlation among different angular scales. The way we achieved this was by simply adding a random component to the large-scale maps that are the input of our GANs. We then trained new models on these *signal + random component* maps, always using the 350 $\tilde{m}^{I,20^\circ}_{12'}$ patches as the training set.

The random component that we considered was simply generated as a random realization from a uniform distribution in the range $[-1, 1]$. Since our input maps were always re-scaled to have pixel values ranging in the same interval to be compatible with the input of our NN, we had a signal-to-noise ratio (SNR) of ~ 1. We refer to this as "stochastic training;" in other words, a random component was added to the input signal, ForSE+S, as opposed to the deterministic case (ForSE+D), in which we did not add any random component to the input maps.

5.3 Pre-processing, training, and post-processing of ForSE+

In this section, we describe the training details of ForSE+S and ForSE+D, including the pre-processing and post-processing steps, and present the results on flat-squared patches, including maps and power spectra, before reprojecting them to full-sky maps.

5.3.1 ForSE+S to $12'$

We first describe how we generate stochastic maps with non-Gaussian features at a resolution of $12'$. We also applied a similar procedure to construct maps at $3'$, as is described in Section 5.3.2. For clarity, we will call ForSE+S12 the model that generates stochastic maps at $12'$ and ForSE+S3 the one that goes up to $3'$.

As was mentioned above, we injected stochasticity into our generative process by simply adding a random component to the low-resolution maps that are the input of our GAN. By

doing so, ForSE+S is able to generate non-Gaussian small-scale features that still partially depend on the real observed large-scale structures but will have a different morphology as we change the realization of the random component in the input dataset.

5.3.1.1 Training and post-processing

As in KP2021, we trained two models for Q and U maps separately. The inputs to the generator, G, were the 174 $M_{80'}^{Q/U,20^\circ}$ patches that together cover the full sky, with dust signal plus an additional random component. The training set, which encodes the target statistical distribution of small scales, was the 350 $\tilde{m}_{12'}^{I,20^\circ}$ maps. The weights of the neural works were updated for 2×10^5 epochs and saved every 500 steps. Since we do not want to generalize the exploitation of the trained model (as it only needs to predict the output from the training data) it is not a problem if there is an over-fitting during training. Therefore, there was no consideration of a separate validation set during the training process.

During the GAN training process, the goal is to produce small-scale feature maps with statistical properties as close as possible to the ones of the training set. We quantified the level of agreement by calculating the overlapping fractions between the distributions of MFs (see Section 4.2) of the maps in the training set ($\tilde{m}_{12'}^{I,20^\circ}$) and those of the generated ones ($\tilde{m}_{12'}^{Q/U,20^\circ}$). The distributions of MFs are indicated by the $\pm 1\sigma$ variation among the training set or generated maps and the overlapping fractions were computed as the ratio between the intersection area and the total area spanned by the two distributions. In practice, we calculated the MFs overlapping for each saved epoch of G and selected as the best model the one with the highest score. In doing so, we computed the MFs for the output maps, $\tilde{m}_{12'}^{Q/U,20^\circ}$, by applying G to maps with the realization of a random component different from the one used for training.

The best models are obtained after 5500 epochs and 6000 epochs for Q and U, respectively. Their MFs are shown in Figure 5.4 and compared with the ones from the training set. The overlap among the distributions is at a level of $50\% - 60\%$, comparable with the one obtained in Krachmalnicoff & Puglisi (2023) (that includes corrections to KP2021). In comparison, Gaussian small scales have MFs with obviously different shapes from these two sets of maps, as is illustrated in Fig.7 of KP2021.

We also computed the overlapping fraction of the MFs by considering 100 different realizations of the small-scale maps (obtained by changing the random component in the input). The mean (standard variation) values of the overlapping fraction for $\mathcal{V}_0$, $\mathcal{V}_1$, and $\mathcal{V}_2$ are 59.1%(1.5%), 62.9%(0.6%), and 55.8%(0.7%), respectively, for Stokes Q maps, and 58.8%(2%), 56.3% (1.3%), and 45.5%(1.1%), respectively, for U maps. These numbers show the robustness of ForSE+S in generating stochastic small scales with non-Gaussian high-order statistics.

Since in the training procedure both the input maps and the training sets are normalized in the range of [-1,1], the output maps also have pixel values in this range, and therefore need to be normalized to restore physical units. We achieved this by following the procedure

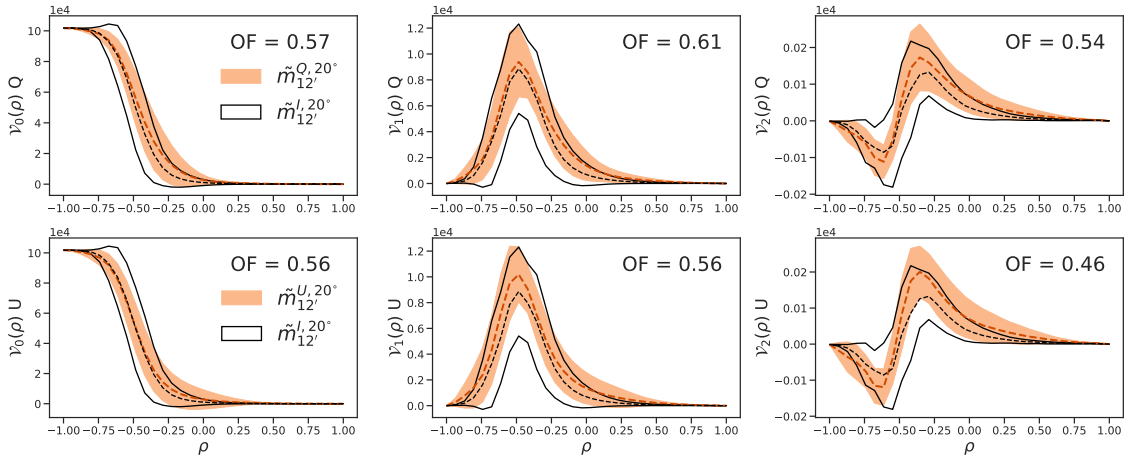

Figure 5.4: MFs of small scales at $12'$ produced by ForSE+S, compared with the ones from the intensity maps in the training set. The overlapping fractions (OFs) of each pair of MFs are also shown. The dashed line represents the mean over the set of different patches and the shaded area is their standard deviation. The distribution of Q maps is shown in the upper panel, and U in the lower panel.

of KP2021, hence ensuring that, for each patch and for both Q and U, the amplitude of the power spectrum of the produced small scales matches the extrapolation at higher multipoles of the power spectrum of the low-resolution input maps at $80'$.

5.3.1.2 Results of ForSE+S at $12'$

Figure 5.5 shows $M^{Q/U,20^\circ}_{12'}$ patches with two different realizations of small scales at $12'$ from ForSE+S12, after the normalization mentioned above, in the second and third columns, compared with the deterministic results from ForSE in the first column. Both the differences at small scales and consistency at large scales between the outputs from ForSE and ForSE+S12 show the capability of the trained model to produce small-scale features in the map space.

To further validate these maps, we calculated the second-order statistics by means of the power spectrum, using the Namaster package (Alonso et al., 2019)[6]. In Figure 5.6, we show the EE and BB power spectra from the QU squared patches of low-resolution maps, the output from ForSE, and 100 realizations of ForSE+S12 in black, green, and gray, respectively. The mean values of power spectra from 100 stochastic realizations are also shown in red. The output maps from ForSE+S12 are consistent with the deterministic output maps in terms of the power spectra, as was expected.

[6] https://namaster.readthedocs.io/en/latest/sample_flat.html

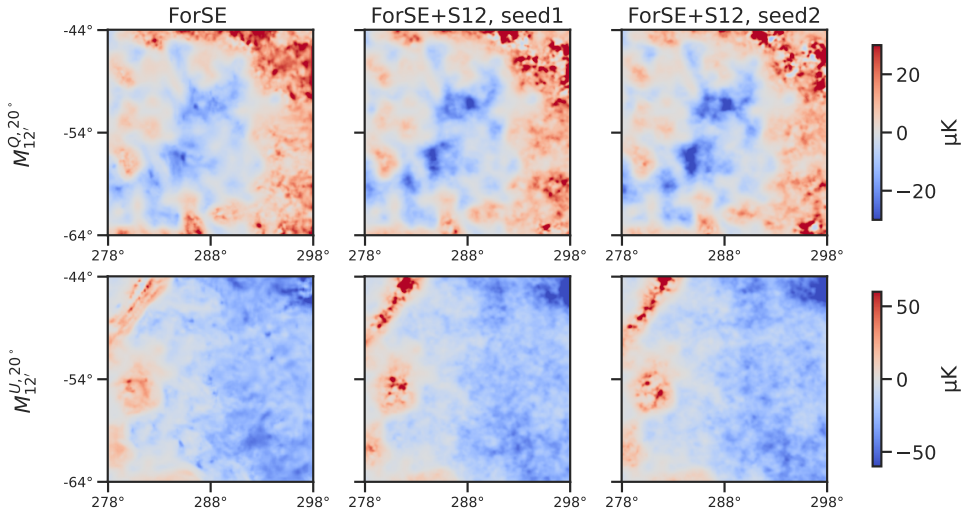

Figure 5.5: Maps of $20^\circ \times 20^\circ$ patches at $12'$. From left to right are the deterministic map from ForSE and two stochastic realizations from ForSE+S12. All the maps are shown in Galactic coordinates.

5.3.2 ForSE+D and ForSE+S3 to $3'$

We describe now the procedures that we followed in order to generate maps at the resolution of $3'$, by using our GAN model iteratively both in the case of ForSE+D and for ForSE+S3. The whole procedures, including several pre- and post-processing steps, are shown in Figure 5.7 and described in the following (see also Foschi (2021)).

5.3.2.1 Pre-processing for the training of ForSE+D

As was mentioned above, we reached the resolution of $3'$ by assuming scale invariance in the statistics of the thermal dust emission. We exploited the output of the first GAN model as the input to a second generative step by using the same training set and considering it to be composed of 350 patches with dimensions of $5^\circ \times 5^\circ$ at a resolution of $3'$, as was explained in Section 5.2.2.1. Therefore, since the first iteration of ForSE allows to go from maps with dimensions of $20^\circ \times 20^\circ$ and a resolution of $80'$ to maps at a resolution of $12'$, the second iteration can produce $5^\circ \times 5^\circ$ maps at a resolution of $3'$. In order to preserve the proportions among all the relevant quantities (i.e., patch dimension, resolution of input, and resolution of output), the input patches for the second iteration should have dimensions corresponding to $5^\circ \times 5^\circ$ and a resolution of $20'$. We can obtain those patches by smoothing and subdividing the output of ForSE.

In practice, we pre-processed each of the 174 $M_{12'}^{Q/U,20^\circ}$ maps with 320×320 pixels obtained from the first iteration in the following way.

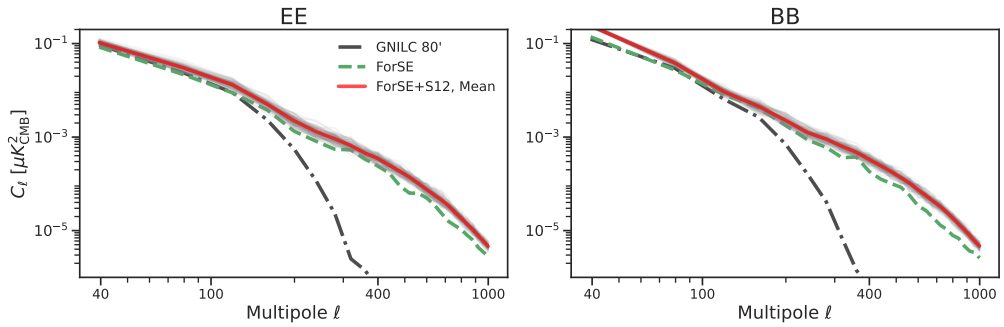

Figure 5.6: EE and BB power spectra of the squared patches at $12'$ shown in Figure 5.5. Dash-dotted black lines are the power spectra for GNILC $80'$ patches and green lines are for the deterministic $12'$ patches. Gray lines show the power spectra of all the 100 realizations from ForSE+S12 and red lines are the means.

1. Each map with 320×320 pixels is re-sampled to 1280×1280 by repeating each pixel four times.

2. The maps are smoothed with a Gaussian kernel in order to reach a resolution of $20'$.

3. Each of the large squared patches is subdivided into $5^\circ \times 5^\circ$ ones, individually containing 320×320 pixels. We divided each large patch into 49 small ones, with a large overlap among them, made of 160 pixels on each side. This overlap is needed in order to avoid border effects when the composition and reprojection on the sphere is performed.

4. At the end of this procedure, we have a set of $174 \times 49 = 8526$ patches for Q and U, which is the total amount of patches covering the full sky and represents the $M_{20'}^{Q/U,5^\circ}$ that will be used as the input to the second GAN iteration.

We applied the same pre-processing to the output of ForSE and ForSE+S12 in order to produce maps at $3'$ in both the deterministic case and the stochastic one. In the stochastic case, we added an additional random component, as is described in Section 5.2.2.2.

5.3.2.2 Training and post-processing of ForSE+D

Once the pre-processing steps described above are performed, the obtained 8526 patches can be used to train a new GAN model. However, the time cost is basically linear with the number of patches. We note that the 8526 patches have repeating pixels among them (see the steps above to get 8526 patches); thus, they are actually not independent. In order to save computational time, we fed as input to the generator, G, only a subset of 696 patches,

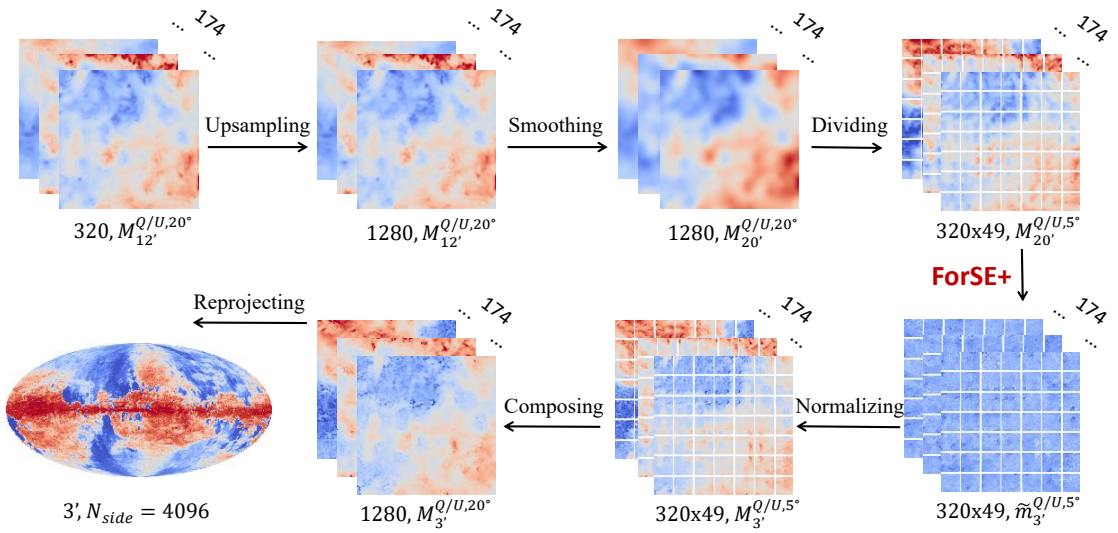

Figure 5.7: Sketch of the pipeline to prepare the training data for ForSE+D (upper row, from left to right) and post-processing to transform the output patches from ForSE+D into the full-sky map at $3'$ in the `HEALPix` format (lower row, from right to left). 174 in the upper right corner of each tile means the number of images. The first number beneath the images indicates the number of pixels on each side of the image and the second expression has the same subscript and superscript as that described in Section 5.2.1. We note that after the "Dividing" and before the "Composing" steps, each original image was divided into 49 sub-patches, with a side length of 5°. At the end, all the flat patches were reprojected onto a `HEALPix` map with N_{side} equal to 4096.

randomly selected from the total 8526 patches. Once the network was trained, we applied it to the remaining patches.

In Figure 5.8 we show the MFs of the generated small scales at $3'$. The overlap with the target distribution is at a level of 70-80% in the deterministic case. In the stochastic case, which is not shown, on the other hand, the overlap ranges between 60% and 70%, showing therefore that we are also able to generate non-Gaussian small scale features at this higher resolution.

The output of the GAN models are patches, $\tilde{m}_{3'}^{Q/U,5^\circ}$, containing the small-scale features that, as in the first iteration, have pixel values in the range of $[-1, 1]$. We therefore normalized them in physical units before multiplying them with the large-scale maps at

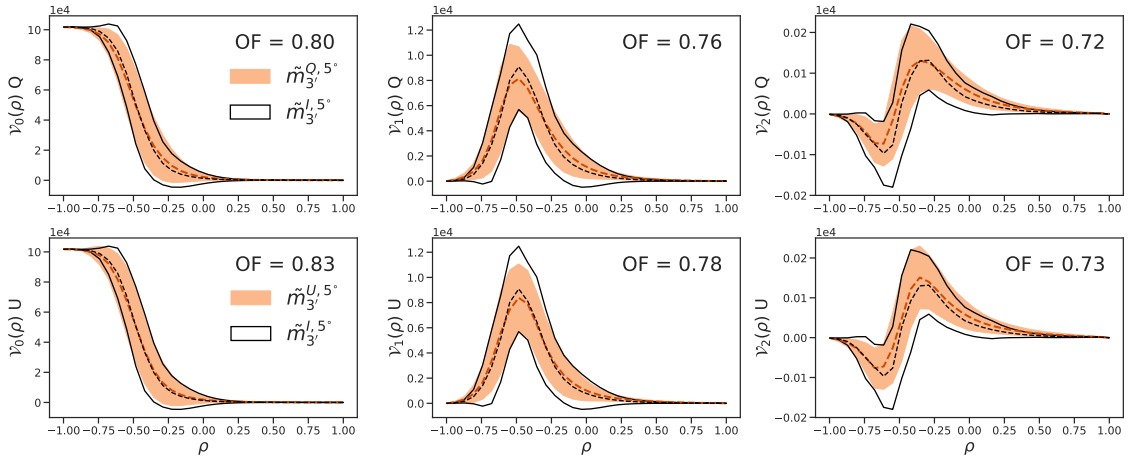

Figure 5.8: MFs overlapping between deterministic $3'$ small scales and intensity small scales.

the resolution of $20'$, obtaining 8526 $M^{Q/U,5^\circ}_{3'}$ maps.

We recall that each of these patches comes from a sub-division of the larger maps with physical dimensions of $20^\circ \times 20^\circ$ (as is described in Section 5.3.2.1) into 49 sub-patches with a large overlap among each other. Therefore, before reprojecting them on the sphere to obtain the full-sky maps, we needed to recombine them. In order to avoid border effects, we did this by using $\cos^2$ apodization window functions, as is shown in Figure 5.9: each sub-patch was weighted with the corresponding window function, then they were summed together to form the 174 $M^{Q/U,20^\circ}_{3'}$ maps that could then be reprojected on the sphere.

5.3.2.3 Results of ForSE+D and ForSE+S3 at $3'$

In Figure 5.10, we show the comparisons of a selected patch at $80'$, $12'$ from ForSE and maps at $3'$ from ForSE+D, from left to right. The small scale structures that ForSE+D can inject are evident, following the modulation of the large-scale emission.

The power spectra, computed on the same patch, are shown in Figure 5.11. As can be seen, the amplitude at low ℓ matches the one from the low-resolution GNILC maps, and the generated small scales have power at higher multipoles, with no breaks in the power spectrum that follows a power law, as was expected.

ForSE+S3 was utilized to generate stochastic small scales at $3'$, as is mentioned in 5.2.2.2. Two realizations of small scales for the Q map in the range of [-1, 1] with a side length of 5° and centered on $[288^\circ, -61.5^\circ]$ (i.e., at the position of the dashed red box in the upper right plot of Figure 5.10) are shown in the upper panel of Figure 5.12, and in the lower panel we show the normalized maps combined with the large scales. The differences between the two realizations should be noted and both of them trace the large-scale features

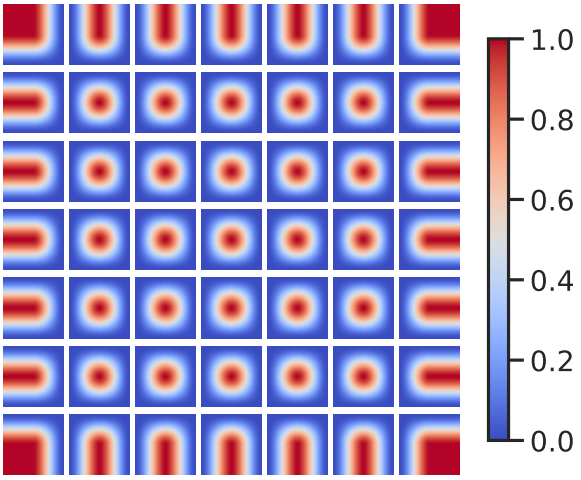

Figure 5.9: Apodized window function of each sub-patch at different positions to compose 49 sub-patches with a side length of 5° into a patch with a length of 20°.

of the input maps. We also show the power spectra of 100 realizations in Figure 5.11, where we also plot the mean, validating the results of stochasticity on the power spectrum level.

5.4 Validations of full-sky maps from ForSE+

In this Section, we show the maps and power spectra after reprojecting the flat patches back to the sphere, following the algorithm in the Appendix of KP2021. Before showing the results, we introduce a further step to adjust the E-to-B ratio in the simulated maps to match the observations at large scales.

5.4.1 Fine-tuning of the E-to-B ratio to match observations

We recall that, due to the limitation of observational data in polarization, we used the statistical properties of the total intensity small scales to be the ground truth of both Q and U during the training process. This implies that the output high-resolution map will have the same power for E and B modes. However, high-frequency observations of the Planck satellite have shown the existence of an asymmetry between the measured power of thermal dust emission in the E and B modes, with $A_{BB}/A_{EE} \sim 0.5$ over the multipole range of $40 \leq \ell \leq 600$ (Planck Collaboration XI, 2020). Therefore, in order to match the real observations, we applied a fine-tuning to the full-sky maps, obtained after all the steps mentioned above.

We first transformed QU maps into the harmonic space to obtain the $a^E_{\ell m}$ and $a^B_{\ell m}$ coefficients. Then we applied a factor of $\sqrt{0.5}$ to the $a^B_{\ell m}$ to decrease its power, since $a^E_{\ell m}$ and $a^B_{\ell m}$ have the same variance as was just mentioned. Finally, we transformed the tuned

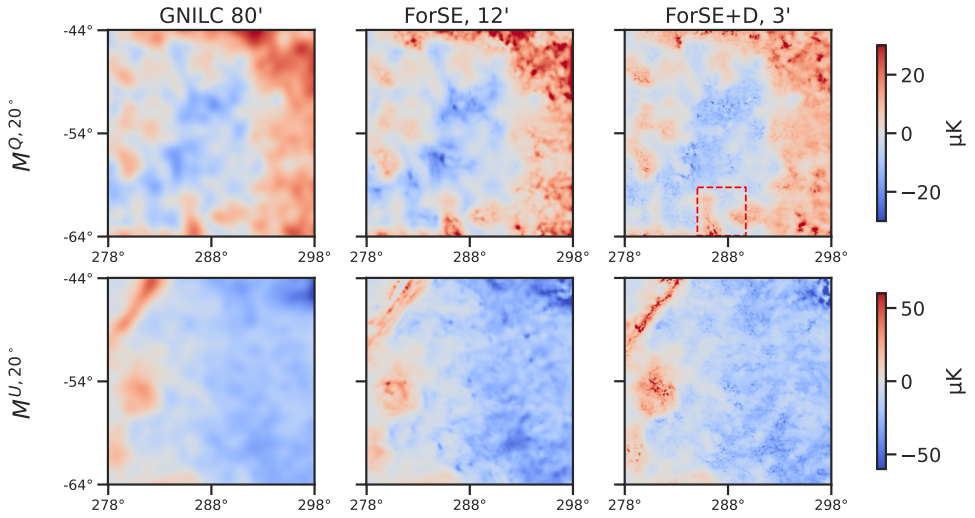

Figure 5.10: $20^\circ \times 20^\circ$ patches of three different resolutions. From left to right are GNILC maps at $80'$, ForSE maps at $12'$, and ForSE+D maps at $3'$.

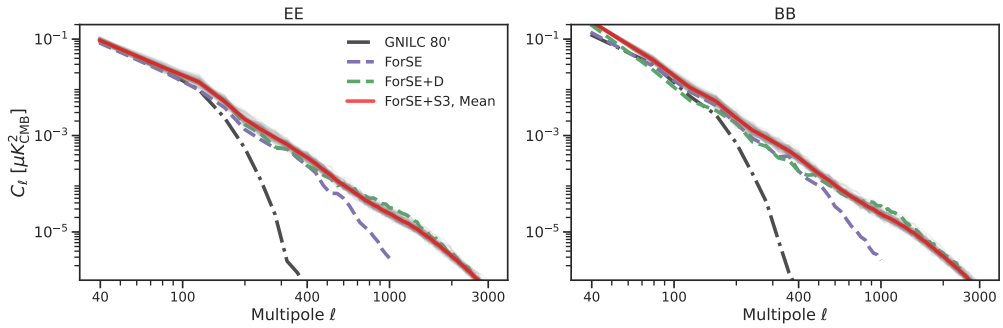

Figure 5.11: EE and BB power spectra of the squared patches at $3'$ shown in Figure 5.10. Dash-dotted black lines are the power spectra for GNILC $80'$ patches and purple lines are for the deterministic $12'$ patches. Green lines depict the behavior of ForSE+D maps, while gray lines show the power spectra of all the 100 realizations from ForSE+S3 and red lines are the means.

$a_{\ell m}s$ back to the map space to get maps that match the observed ratio of 0.5 at the power spectra level. We note that the large scales in the output maps of ForSE/ForSE+ remain to be the observed ones, so the tuning was applied only to the small scales; that is, $a_{\ell m}s$ belonging to $\ell > 135$[7] and the transition between large and small scales was smoothed with

[7]Corresponding to $80'$: $\ell = \pi/\theta = \pi/(80/60/180 * \pi) = 135$.

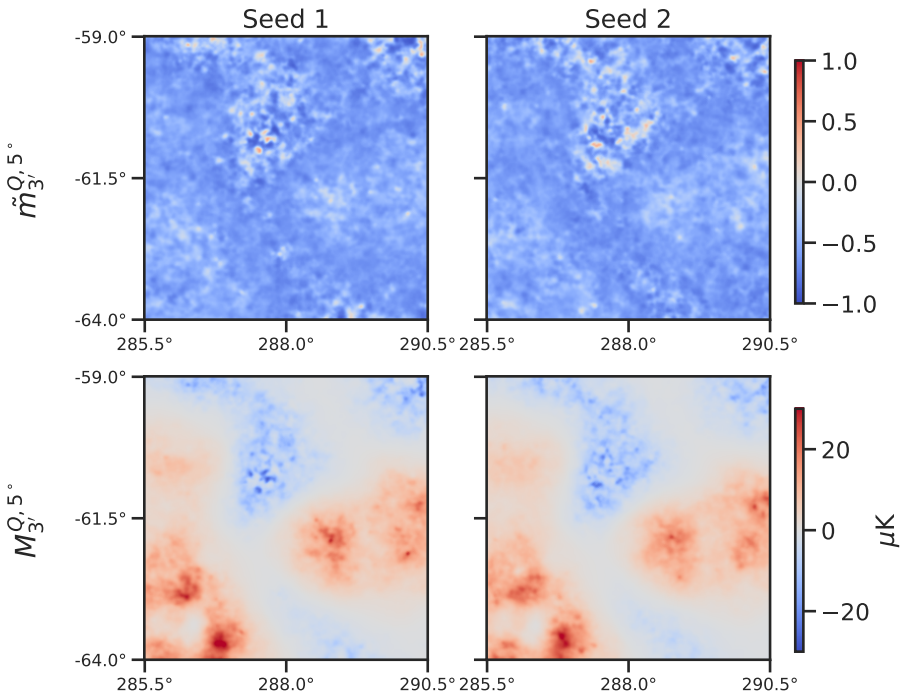

Figure 5.12: Upper panel: Two stochastic realizations of Q maps, $\tilde{m}_{3'}^{Q,5^\circ}$, from FORSE+S3. Lower panel: $M_{3'}^{Q,5^\circ}$ maps of the upper panel after the normalization step. This patch is at the position of the dashed red box in the upper right plot of Figure 5.10.

a sigmoid function to avoid discontinuities in the final power spectra.

The E-to-B ratios of the power spectra calculated for different fractions of sky are shown in Figure 5.13. The red lines show the ratios after the tuning steps, which were indeed corrected to ~ 2 for the injected small scales.

5.4.2 Full-sky maps

We are now ready to present the full-sky maps and specifically, we show the FORSE+D maps at $3'$, at Nside $= 4096$, in Figure 5.14, compared with the input GNILC ones at $80'$. The difference between the two highlights the presence of small-scale features in the FORSE+D maps. When zooming into a patch that consists of two $M_{3'}^{Q/U,20^\circ}$ patches we also find no clear edge effects. These results show that border effects from reprojection are negligible.

In Figure 5.15, the power spectra of the maps on the sphere at different resolutions are shown for different sky fractions. As was expected, our maps at $3'$ can further extrapolate

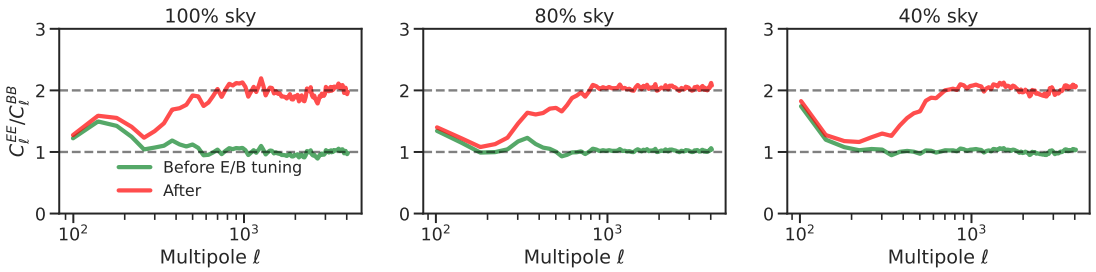

Figure 5.13: E-to-B ratios of non-tuned and tuned maps in green and red lines, for different sky masks.

the power up to $\ell \sim 3600$, which corresponds to the drop scale of $3'$. We also note the absence of discontinuities at the transition from large scales to small scales ($\ell > 200$), implying that the small scales are produced with a similar pattern as the one at large scales, attributed to the normalization step to rescale the generated small scales in the range of [-1, 1] to the correct amplitude, as was mentioned in Section 5.3.2.2. In order to make a comparison with the latest `d9` dust model from `PySM3`, we also show the power spectra of `d9` maps at 353GHz in blue. Although the latter was produced with entirely different methods, the power spectra of ForSE+D maps at $3'$ are impressively close to those of `d9` maps, even for different sky fractions.

We also calculated the power spectra of 100 realizations of full-sky maps at $3'$, generated with ForSE+S3, with a 80% sky mask, up to $\ell_{max} = 4096$ and with a bin width of $\Delta\ell = 160$. The covariance matrix from these 100 realizations is shown in Figure 5.16. The correlation among multipoles at small scales is further evidence that the small scales at $\ell > 800$ were synthesized in a non-Gaussian way. In fact, if the small-scale features were produced with Gaussian properties, we would not observe any non-diagonal correlation, which is verified from our experiment to calculate the covariance matrix of a purely Gaussian field. We devote the next Section to further deepening the non-Gaussian properties of our maps.

5.4.3 Non-Gaussianity measured on the sphere

In previous Sections, we considered the MFs in order to characterize non-Gaussianity for flat patches. Here, we expand the analysis to the full-sky maps, by exploiting the algorithms described in Grewal et al. (2022b), in order to calculate MFs for spherical maps in the `HEALPix` format. We focus on the small scales injected by ForSE and ForSE+D and here we used the multipole range [200, 2048] to band-pass filter the raw maps and applied a 80% sky mask to ignore the Galactic plane.

In Figure 5.17 we show the results of the MFs statistics applied to the sphere, confirming our previous claims. Differences in the ForSE+D map are visible with respect to the case

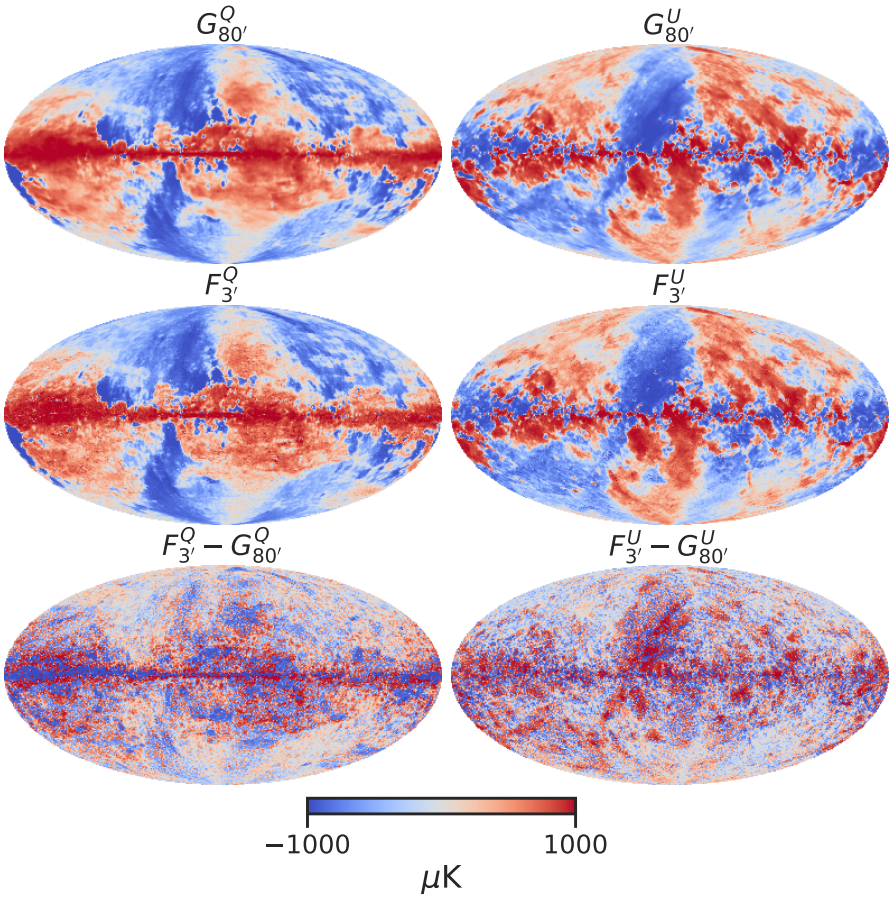

Figure 5.14: Top panel: full-sky polarization maps (left: Stokes Q, right: Stokes U) for the GNILC template at a $80'$ angular resolution. These maps are the input to our algorithm. Middle panel: maps with small scale features, up to $3'$, generated by FORSE+D. Bottom panel: the difference between the two maps. The residuals mostly encode smaller angular scales, as was expected.

of Gaussian maps in dashed gray for all three kinds of MFs. The Gaussian maps were generated from a random realization from the power spectra of the FORSE+D Q map. We also show the results of the latest `PySM3 d9` dust maps in blue, which exhibits a deviation from Gaussianity, although being similar to the modulated Gaussian maps in orange, whose non-Gaussianity is supposed to derive only from the modulation of large scales. We further checked that the results are robust for the 40% sky mask and for $\ell_{min} = 500$ and 1000.

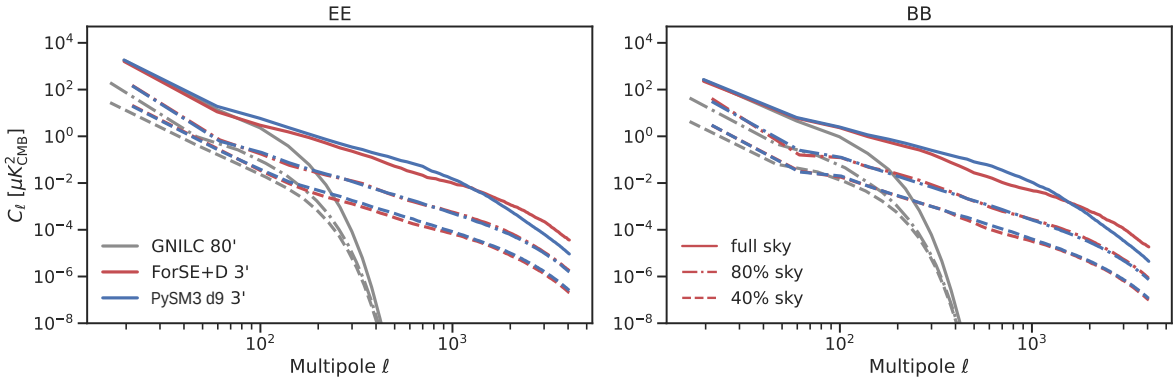

Figure 5.15: EE and BB Power spectra of GNILC 80′, deterministic 3′ in gray and red, with $f_{sky} = 1$, 0.8, and 0.4 in solid, dash-dotted, and dashed lines, respectively. In order to make a comparison, we also show the power spectra of `PySM3 d9` dust map at 353GHz in blue.

5.5 Summary

In this Chapter, we extend the ability of the ForSE model proposed in KP2021 based on the GAN technique to simulate non-Gaussian stochastic small scales of polarized thermal dust emission up to 3′. We have trained three new models, which are summarized in Table 5.1, together with the one trained in KP2021.

Based on the results obtained in KP2021, our first test was to bring stochasticity into our models by adding a random component into the input and to train a new network called ForSE+S12 so that it can generate different maps with different seeds. MFs were used to quantify the level of non-Gaussianity in the maps and in Figure 5.4 we demonstrate that the polarized thermal dust small scales have a similar level of non-Gaussianity to that in the intensity small scales. Different realizations of maps at 12′ for a specific patch and the corresponding power spectra are shown in Figure 5.6, which indeed have expected variations at small scales and the correct amplitude scaling with multipoles for power spectra.

We then considered the case of a 3′ angular scale, where lensing B-modes have the strongest signal, and we studied the deterministic case first, ForSE+D. By relying on the scale invariance assumption discussed in Section 5.2.2.1 and the pre- and post-processing steps outlined in Figure 5.7, we trained the model to generate maps at 3′ out of those at 12′, which are the output from ForSE. MFs distributions in Figure 5.8 represent a verification of the training process. Maps and power spectra of a selected patch of maps at 3′ are shown in Figure 5.10, where the 3′ power is present as expected. ForSE+S3 was finally trained in order to generate stochastic small scales at 3′. Two realizations of small scales are shown in Figure 5.12, with their power spectra shown in the right panel of

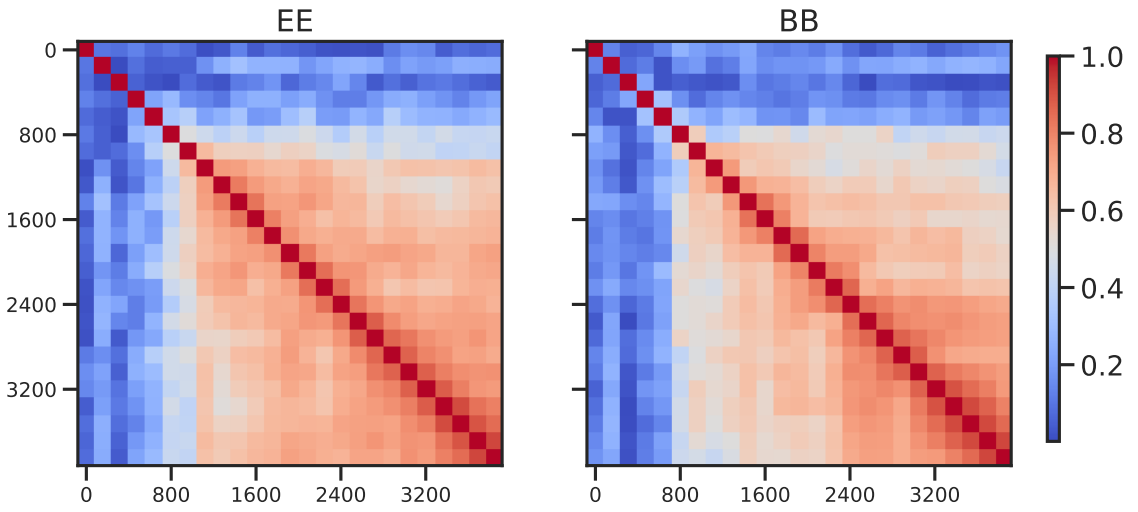

Figure 5.16: Covariance matrices of maps at $3'$ on the sphere with an 80% sky mask, shown in absolute values. Calculated for power spectra of an ℓ-bin range of [40, 4096] with a bin width of 160. Non-diagonal terms are normalized with the diagonal values, i.e., $R_{ij} = \frac{C_{ij}}{\sqrt{C_{ii}C_{jj}}}$.

Figure 5.10, showing the expected multipole scaling.

After obtaining the small scales on flat patches, we re-projected them onto the celestial sphere in order to get full-sky maps in the `HEALPix` format, with $N_{side} = 2048$ for maps at $12'$ and 4096 for maps at $3'$. We show the Mollview projection of the deterministic maps at $3'$ in Figure 5.14 and compare them with the observed *Planck* GNILC maps, validating both the effectiveness of the injected small scales and the reprojection process. The power spectra of deterministic maps at $80', 12'$, and $3'$ with $100\%, 80\%$, and 40% sky masks are plotted in Figure 5.15, indicating that the small scales generated preserve the same anisotropies as the low-resolution observations.

We further obtain the covariance matrix of power spectra up to $\ell_{max} \sim 4000$ from 100 realizations of maps at $3'$ in Figure 5.16, which has a strong correlation between different multipoles at small scales, and thus highlights the non-Gaussianity in our maps. We note that for a Gaussian field, the variances along the diagonal line are smaller than the variances we obtained here and the off-diagonal correlation is zero. We repeated the calculation of the covariance matrix for the `PySM3 d11` model, which is also designed to generate multiple realizations of small scales of thermal dust emission (PanEx Collaboration, 2024), and find that off-diagonal elements are also close to zero, meaning that the level of non-Gaussianity of the injected small scales on the full sky is small.

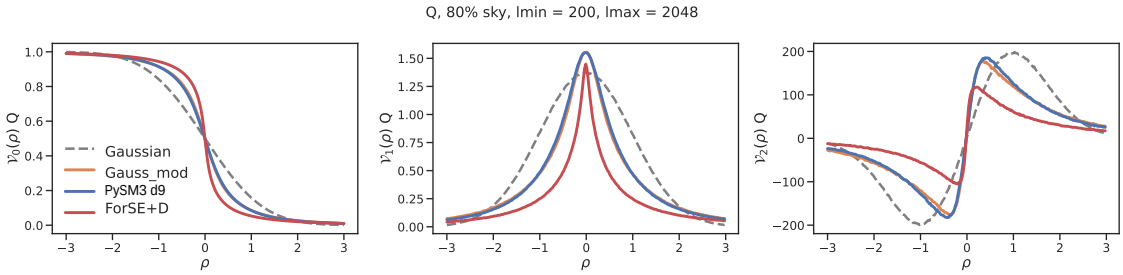

Figure 5.17: The three kinds of MFs for the ForSE+D Q full-sky map at $3'$ with an 80% sky mask (red). The raw map is band-pass filtered to keep small scales only, corresponding to the multipole range [200, 2048]. The dashed gray lines show the MFs of the Gaussian maps. Results for `PySM3 d9` and modulated Gaussian maps are also shown in blue and orange, respectively.

Finally, we measured the level of non-Gaussianity using MFs in the simulated full-sky maps in Figure 5.17, and compared it with the small scales simulated within the Gaussian assumption. The difference between the MFs obtained from the two kinds of maps is another clear indication of the non-Gaussian small-scale component generated with ForSE+. We shall discuss further exploitation of the maps obtained by ForSE+ in the Conclusions.

Future improvements in the ForSE algorithm are foreseeable. First, more observations are needed. In fact, the assumptions made in Section 5.2.2 are somewhat a compromise due to the lack of observation at the required resolution. The models will get more reliable as more observations become available. Second, by considering the network architecture, the loss function accounting for the non-Gaussianity of the targets produced by the GAN may be considered, as in the current implementation this process is not automatized. A way to quantify the level of non-Gaussianity with a formalism that is differentiable with respect to the input pixels would be desirable, as then we could construct the loss function of the network in order to include the information of non-Gaussianity, which will effectively guide the generator. The last point we want to mention is that the operation of adding noise is to some extent like the training process of diffusion models in deep learning, which is more natural than what is done in this work.

The code to generate maps has also been made publicly available[8].

[8] https://github.com/yaojian95/ForSEplus.

6

Conclusions

With the aim to push down the upper limit of the tensor-to-scalar value, many CMB experiments are constantly upgrading the detectors to improve the sensitivity, resolution, sky and frequency coverage of the observations. The advancements in instrumentation enhance not only direct observations of the CMB but also significantly improve foreground control. This capability is crucial for modern observations aimed at probing PGWs, as observational evidences indicate that foreground power is comparable to or even surpasses the CMB across all frequencies and angular scales, reaching down to arcminute resolutions. In this situation, where accurate data on foregrounds are lacking in particular, it is imperative not only to design methods capable of controlling and removing the foreground emission out of a multi-frequency observations, but also, having good and complete models of foregrounds, in order to validate those techniques. This is the subject of the problem we face in this Thesis: we construct models of the main polarized foreground, the thermal dust emission in our own Galaxy, which enable to simulate the emission at unobserved frequencies and angular resolutions beyond current observational limits. This approach maximizes the use of available observational data while reflecting the present uncertainties in the spatial distribution and frequency dependence of foregrounds. We concentrate on two foreground models, both designed to meet the requirements of CMB data analysis.

Chapter 4 describes our contribution within the collaboration PanEx GSWG to update the widely used package `PySM3` to simulate CMB foregrounds. It integrates optimized data and new models in the literature to provide different level of complexity when preparing the simulations for CMB data analysis. In particular, we use MFs as a tool to quantify the

non-Gaussianity injected into the small scales of thermal dust emission generated by the new model (called `d10` in `PySM3`) based on the PolTens framework, which imprints non-Gaussianity by transforming the maps back and forth non-linearly. As expected, we found that the non-Gaussianity in the small scales simulated in this manner is similar to that of modulated small scales when averaging over the sky within `GAL80` mask which means that the induced non-Gaussianity comes from the modulation process. We also investigated this process locally, i.e. by considering small flat patches individually, and found that the measured MFs of `d10` indicate a non-Gaussian pattern which however might be caused by local deviation from perfect large-scale modulation. Therefore, even for the most advanced technique implemented in the `PySM3` and in particular for the `d10` model, a pure modulation effect as observed on the large scale foreground power is capable of accounting for the entire non-Gaussian effects injected into small scales.

We face this problem with the work which is described in Chapter 5, based on Yao et al. (2024), where we present a new methodology called ForSE+ based on NN. It is able to simulate foreground pattern at the arcminute scale and generate multiple realizations, preserving all the non-Gaussian statistics which is present at observed large scales, as indicated by MFs. We use the same network in KP2021 in order to obtain the polarized thermal dust emission with small-scale information at 353 GHz. The extension to arcminute scale is achieved through the scale invariance assumption, in which our training samples at $12'$ can equally be treated as having patches at $3'$ and thus can be treated as the target for the NN to learn to generate small scales. We validate the generated maps by comparing with observations at large scales, in terms of power spectra and non-Gaussianity. Once the steps above are achieved, we can use the synthetic dust Stokes Q and U maps at 353 GHz at $3'$ resolution as a template and appropriately scale across different frequencies by taking the observed dust SEDs, similar to what `PySM3` does.

Toolkits such as `PySM3` and ForSE+ play a crucial role in the simulation of foreground maps, which are essential for studying cosmological signals in the presence of astrophysical contamination. These tools allow for the generation of realistic foreground realizations, which can be used to assess the effectiveness and robustness of component separation algorithms. By simulating multiple foreground realizations, researchers can quantify the scatter and uncertainties in the separation process, ensuring that the extraction of the cosmological signal remains accurate across various foreground models.

Furthermore, high-resolution non-Gaussian maps are vital for testing and validating lensing reconstruction methods. Lensing from inhomogeneous gravitational field distorts the path of CMB photons and introduces non-Gaussianity to the observed CMB maps, dominating the B-modes at small scales. Lensing reconstruction methods try to recover the gravitational potential which can be used to delensing the CMB BB spectra. The residual non-Gaussian foregrounds can lead to bias to these two processes and the effects have been tested so far on foreground models where the arcminute structure is either absent or Gaussian (Lonappan et al., 2023), or based on models of the Galactic magnetic fields in order to reproduce a non-Gaussian pattern (Beck et al., 2020). High-resolution simu-

lations of foregrounds with the level of non-Gaussianity constrained by the data provide a detailed benchmark against which lensing reconstruction algorithms can be compared, ensuring their reliability and performance in real data analyses. These maps help to identify and correct potential biases or inaccuracies that could arise in low-resolution datasets, ultimately improving the accuracy of cosmological inferences.

Thanks to the results presented in this Thesis, we can start these analysis in order to give responses to the CMB community about these outstanding questions, at least with the current, and unprecedented, faithfulness of non-Gaussian pattern in foregrounds, at all the angular scales of interest.

Bibliography

Abazajian, K., Addison, G., Adshead, P., et al. 2019, arXiv e-prints, arXiv:1907.04473, doi: 10.48550/arXiv.1907.04473

Abazajian, K. N., Adshead, P., Ahmed, Z., et al. 2016, arXiv e-prints, arXiv:1610.02743, doi: 10.48550/arXiv.1610.02743

Abril-Cabezas, I., Hervías-Caimapo, C., von Hausegger, S., Sherwin, B. D., & Alonso, D. 2024, MNRAS, 527, 5751, doi: 10.1093/mnras/stad3529

Ade, P., Aguirre, J., Ahmed, Z., et al. 2019, J. Cosmology Astropart. Phys., 2019, 056, doi: 10.1088/1475-7516/2019/02/056

Albrecht, A., & Steinhardt, P. J. 1982, Phys. Rev. Lett., 48, 1220, doi: 10.1103/PhysRevLett.48.1220

Allys, E., Levrier, F., Zhang, S., et al. 2019, A&A, 629, A115, doi: 10.1051/0004-6361/201834975

Alonso, D., Sanchez, J., Slosar, A., & LSST Dark Energy Science Collaboration. 2019, MNRAS, 484, 4127, doi: 10.1093/mnras/stz093

Aluri, P. K., & Rath, P. K. 2016, MNRAS, 458, 4269, doi: 10.1093/mnras/stw283

Alzubaidi, L., Zhang, J., Humaidi, A. J., et al. 2021, Journal of Big Data, 8. https://api.semanticscholar.org/CorpusID:232434552

Anderson, L., Aubourg, E., Bailey, S., et al. 2012, MNRAS, 427, 3435, doi: 10.1111/j.1365-2966.2012.22066.x

Aylor, K., Haq, M., Knox, L., Hezaveh, Y., & Perreault-Levasseur, L. 2021, MNRAS, 500, 3889, doi: 10.1093/mnras/staa3344

Baccigalupi, C. 2003, New A Rev., 47, 1127, doi: 10.1016/j.newar.2003.09.038

Baccigalupi, C., Bedini, L., Burigana, C., et al. 2000, MNRAS, 318, 769, doi: 10.1046/j.1365-8711.2000.03751.x

Bardeen, J. M. 1980, Phys. Rev. D, 22, 1882, doi: 10.1103/PhysRevD.22.1882

Bardeen, J. M., Steinhardt, P. J., & Turner, M. S. 1983, Phys. Rev. D, 28, 679, doi: 10.1103/PhysRevD.28.679

Bartolo, N., Komatsu, E., Matarrese, S., & Riotto, A. 2004, Phys. Rep., 402, 103, doi: 10.1016/j.physrep.2004.08.022

Bassett, B., & Hlozek, R. 2010, in Dark Energy: Observational and Theoretical Approaches, ed. P. Ruiz-Lapuente, 246, doi: 10.48550/arXiv.0910.5224

Baumann, D. 2009, arXiv e-prints, arXiv:0907.5424, doi: 10.48550/arXiv.0907.5424

Baumann, D. 2022, Cosmology (Cambridge University Press)

Beck, D., Errard, J., & Stompor, R. 2020, J. Cosmology Astropart. Phys., 2020, 030, doi: 10.1088/1475-7516/2020/06/030

Ben-David, A., von Hausegger, S., & Jackson, A. D. 2015, J. Cosmology Astropart. Phys., 2015, 019, doi: 10.1088/1475-7516/2015/11/019

Bennett, C. L., Larson, D., Weiland, J. L., et al. 2013, ApJS, 208, 20, doi: 10.1088/0067-0049/208/2/20

Bernardi, G., Carretti, E., Fabbri, R., et al. 2004, MNRAS, 351, 436, doi: 10.1111/j.1365-2966.2004.07797.x

Bertone, G., & Hooper, D. 2018, Reviews of Modern Physics, 90, 045002, doi: 10.1103/RevModPhys.90.045002

BeyondPlanck Collaboration I. 2023, A&A, 675, A1, doi: 10.1051/0004-6361/202244953

BICEP2 Collaboration, Ade, P. A. R., Aikin, R. W., et al. 2014, Phys. Rev. Lett., 112, 241101, doi: 10.1103/PhysRevLett.112.241101

BICEP2 Collaboration, Keck Array Collaboration, Ade, P. A. R., et al. 2016, Phys. Rev. Lett., 116, 031302, doi: 10.1103/PhysRevLett.116.031302

BICEP2/Keck Collaboration, Planck Collaboration, Ade, P. A. R., et al. 2015, Phys. Rev. Lett., 114, 101301, doi: 10.1103/PhysRevLett.114.101301

Bicep/Keck Collaboration XIII. 2021, Phys. Rev. Lett., 127, 151301, doi: 10.1103/PhysRevLett.127.151301

Blau, M. 2022, Lecture Notes on General Relativity, http://www.blau.itp.unibe.ch/GRLecturenotes.html

Bonjean, V., Tanimura, H., Aghanim, N., Bonnaire, T., & Douspis, M. 2024, A&A, 686, A91, doi: 10.1051/0004-6361/202245624

Cabella, P., Pietrobon, D., Veneziani, M., et al. 2010, MNRAS, 405, 961, doi: 10.1111/j.1365-2966.2010.16542.x

Cardoso, J.-F., Martin, M., Delabrouille, J., Betoule, M., & Patanchon, G. 2008, arXiv e-prints, arXiv:0803.1814, doi: 10.48550/arXiv.0803.1814

Carones, A., CarrónDuque, J., Marinucci, D., Migliaccio, M., & Vittorio, N. 2024, MNRAS, 527, 756, doi: 10.1093/mnras/stad3002

Carones, A., & Remazeilles, M. 2024, J. Cosmology Astropart. Phys., 2024, 018, doi: 10.1088/1475-7516/2024/06/018

Choi, S. K., Hasselfield, M., Ho, S.-P. P., et al. 2020, J. Cosmology Astropart. Phys., 2020, 045, doi: 10.1088/1475-7516/2020/12/045

Clark, S. E., & Hensley, B. S. 2019, ApJ, 887, 136, doi: 10.3847/1538-4357/ab5803

Coil, A. L. 2013, The Large-Scale Structure of the Universe, ed. T. D. Oswalt & W. C. Keel (Dordrecht: Springer Netherlands), 387–421, doi: 10.1007/978-94-007-5609-0_8

Cooke, R. J., Pettini, M., & Steidel, C. C. 2018, ApJ, 855, 102, doi: 10.3847/1538-4357/aaab53

Coulton, W. R., & Spergel, D. N. 2019, J. Cosmology Astropart. Phys., 2019, 056, doi: 10.1088/1475-7516/2019/10/056

Das, S., Sherwin, B. D., Aguirre, P., et al. 2011, Phys. Rev. Lett., 107, 021301, doi: 10.1103/PhysRevLett.107.021301

Delabrouille, J., & Cardoso, J. F. 2007, arXiv e-prints, astro, doi: 10.48550/arXiv.astro-ph/0702198

Delabrouille, J., Cardoso, J. F., Le Jeune, M., et al. 2009, A&A, 493, 835, doi: 10.1051/0004-6361:200810514

Delabrouille, J., Cardoso, J. F., & Patanchon, G. 2003, MNRAS, 346, 1089, doi: 10.1111/j.1365-2966.2003.07069.x

Delouis, J. M., Allys, E., Gauvrit, E., & Boulanger, F. 2022, A&A, 668, A122, doi: 10.1051/0004-6361/202244566

Dicke, R. H., Peebles, P. J. E., Roll, P. G., & Wilkinson, D. T. 1965, ApJ, 142, 414, doi: 10.1086/148306

Dickinson, C., Ali-Haïmoud, Y., Barr, A., et al. 2018, New A Rev., 80, 1, doi: 10.1016/j.newar.2018.02.001

Diego-Palazuelos, P., Vielva, P., & Herranz, D. 2021, J. Cosmology Astropart. Phys., 2021, 048, doi: 10.1088/1475-7516/2021/03/048

Dodelson, S., & Schmidt, F. 2020, Modern Cosmology (Academic Press), doi: 10.1016/C2017-0-01943-2

Draine, B. T. 2011, Physics of the Interstellar and Intergalactic Medium (Princeton University Press)

Draine, B. T., & Hensley, B. 2013, ApJ, 765, 159, doi: 10.1088/0004-637X/765/2/159

Draine, B. T., & Lazarian, A. 1998, ApJ, 508, 157, doi: 10.1086/306387

Einstein, A. 1917, Sitzungsberichte der Königlich Preussischen Akademie der Wissenschaften, 142

Eriksen, H. K., Jewell, J. B., Dickinson, C., et al. 2008, ApJ, 676, 10, doi: 10.1086/525277

Eriksen, H. K., O'Dwyer, I. J., Jewell, J. B., et al. 2004, ApJS, 155, 227, doi: 10.1086/425219

Errard, J., Stivoli, F., & Stompor, R. 2011, Phys. Rev. D, 84, 069907, doi: 10.1103/PhysRevD.84.069907

Fernández-Torreiro, M., Génova-Santos, R. T., Rubiño-Martín, J. A., et al. 2024, MNRAS, 527, 11945, doi: 10.1093/mnras/stad3145

Finkbeiner, D. P., Davis, M., & Schlegel, D. J. 1999, ApJ, 524, 867, doi: 10.1086/307852

Foschi, M. 2021, Master's thesis, University of Trento. https://www5.unitn.it/Biblioteca/it/Web/TesiDocente/195543

Fraisse, A. A., Brown, J.-A. C., Dobler, G., et al. 2009, in American Institute of Physics Conference Series, Vol. 1141, CMB Polarization Workshop: Theory and Foregrounds: CMBPol Mission Concept Study, ed. S. Dodelson, D. Baumann, A. Cooray, J. Dunkley, A. Fraisse, M. G. Jackson, A. Kogut, L. Krauss, M. Zaldarriaga, & K. Smith (AIP), 265–310, doi: 10.1063/1.3160889

Friedmann, A. 1922, Zeitschrift fur Physik, 10, 377, doi: 10.1007/BF01332580

Ganesan, V. 2017, Geometrical and topological properties of CMB polarization fields

Gawiser, E., & Silk, J. 2000, Phys. Rep., 333, 245, doi: 10.1016/S0370-1573(00)00025-9

Ghosh, S., Liu, Y., Zhang, L., et al. 2022, J. Cosmology Astropart. Phys., 2022, 063, doi: 10.1088/1475-7516/2022/10/063

Goodfellow, I. J., Pouget-Abadie, J., Mirza, M., et al. 2014, arXiv e-prints, arXiv:1406.2661, doi: 10.48550/arXiv.1406.2661

Górski, K. M., Hivon, E., Banday, A. J., et al. 2005, ApJ, 622, 759, doi: 10.1086/427976

Grewal, N., Zuntz, J., Tröster, T., & Amon, A. 2022a, The Open Journal of Astrophysics, 5, 13, doi: 10.21105/astro.2206.03877

—. 2022b, The Open Journal of Astrophysics, 5, 13, doi: 10.21105/astro.2206.03877

Guth, A. H. 1981, Phys. Rev. D, 23, 347, doi: 10.1103/PhysRevD.23.347

Hadwiger, H. 1957, Vorlesungen ueber Inhalt, Oberflache und Isoperimetrie, Die Grundlehren der mathematischen Wissenschaften (Springer). https://books.google.it/books?id=YiA4tAEACAAJ

Hanany, S., Ade, P., Balbi, A., et al. 2000, ApJ, 545, L5, doi: 10.1086/317322

Hanson, D., Hoover, S., Crites, A., et al. 2013, Phys. Rev. Lett., 111, 141301, doi: 10.1103/PhysRevLett.111.141301

Harrison, E. R. 1970, Phys. Rev. D, 1, 2726, doi: 10.1103/PhysRevD.1.2726

Henning, J. W., Sayre, J. T., Reichardt, C. L., et al. 2018, ApJ, 852, 97, doi: 10.3847/1538-4357/aa9ff4

Herman, D., Hensley, B., Andersen, K. J., et al. 2023, A&A, 675, A15, doi: 10.1051/0004-6361/202243081

Hervías-Caimapo, C., & Huffenberger, K. M. 2022, ApJ, 928, 65, doi: 10.3847/1538-4357/ac54b2

Heurtel-Depeiges, D., Burkhart, B., Ohana, R., & Régaldo-Saint Blancard, B. 2023, arXiv e-prints, arXiv:2310.16285, doi: 10.48550/arXiv.2310.16285

Hikage, C., Komatsu, E., & Matsubara, T. 2006, ApJ, 653, 11, doi: 10.1086/508653

Hu, W. 2000, Phys. Rev. D, 62, 043007, doi: 10.1103/PhysRevD.62.043007

Hu, W., & Dodelson, S. 2002, ARA&A, 40, 171, doi: 10.1146/annurev.astro.40.060401.093926

Hu, W., & Okamoto, T. 2002, ApJ, 574, 566, doi: 10.1086/341110

Hu, W., & White, M. 1997, New A, 2, 323, doi: 10.1016/S1384-1076(97)00022-5

Ichiki Kiyotomo. 2014, Progress of Theoretical and Experimental Physics, 2014, 06B109, doi: 10.1093/ptep/ptu065

Irfan, M. O. 2023, MNRAS, 520, 6070, doi: 10.1093/mnras/stad526

Jung, G., Racine, B., & van Tent, B. 2018, J. Cosmology Astropart. Phys., 2018, 047, doi: 10.1088/1475-7516/2018/11/047

Kamionkowski, M., Kosowsky, A., & Stebbins, A. 1997, Phys. Rev. D, 55, 7368, doi: 10.1103/PhysRevD.55.7368

Kamionkowski, M., & Kovetz, E. D. 2014, Phys. Rev. Lett., 113, 191303, doi: 10.1103/PhysRevLett.113.191303

Kim, C.-G., Choi, S. K., & Flauger, R. 2019, ApJ, 880, 106, doi: 10.3847/1538-4357/ab29f2

Kingma, D. P., & Ba, J. 2014, arXiv e-prints, arXiv:1412.6980, doi: 10.48550/arXiv.1412.6980

Kogut, A., Banday, A. J., Bennett, C. L., et al. 1996, ApJ, 464, L5, doi: 10.1086/310072

Komatsu, E. 2002, arXiv e-prints, astro, doi: 10.48550/arXiv.astro-ph/0206039

—. 2010, Classical and Quantum Gravity, 27, 124010, doi: 10.1088/0264-9381/27/12/124010

Komatsu, E., & Spergel, D. N. 2001, Phys. Rev. D, 63, 063002, doi: 10.1103/PhysRevD.63.063002

Kovac, J. M., Leitch, E. M., Pryke, C., et al. 2002, Nature, 420, 772, doi: 10.1038/nature01269

Krachmalnicoff, N., Baccigalupi, C., Aumont, J., Bersanelli, M., & Mennella, A. 2016, A&A, 588, A65, doi: 10.1051/0004-6361/201527678

Krachmalnicoff, N., & Puglisi, G. 2021, ApJ, 911, 42, doi: 10.3847/1538-4357/abe71c

Krachmalnicoff, N., & Puglisi, G. 2023, The Astrophysical Journal, 947, 93, doi: 10.3847/1538-4357/acc9c0

Krachmalnicoff, N., & Tomasi, M. 2019, A&A, 628, A129, doi: 10.1051/0004-6361/201935211

Krachmalnicoff, N., Carretti, E., Baccigalupi, C., et al. 2018, A&A, 618, A166, doi: 10.1051/0004-6361/201832768

Kritsuk, A. G., Flauger, R., & Ustyugov, S. D. 2018, Phys. Rev. Lett., 121, 021104, doi: 10.1103/PhysRevLett.121.021104

Larson, D., Dunkley, J., Hinshaw, G., et al. 2011, ApJS, 192, 16, doi: 10.1088/0067-0049/192/2/16

Leach, S. M., Cardoso, J. F., Baccigalupi, C., et al. 2008, A&A, 491, 597, doi: 10.1051/0004-6361:200810116

LeCun, Y., Bengio, Y., & Hinton, G. 2015, Nature, 521, 436, doi: 10.1038/nature14539

LeCun, Y., Boser, B. E., Denker, J. S., et al. 1989, in Neural Information Processing Systems. https://api.semanticscholar.org/CorpusID:2542741

Lemaître, G. 1931, MNRAS, 91, 483, doi: 10.1093/mnras/91.5.483

Lenz, D., Hensley, B. S., & Doré, O. 2017, ApJ, 846, 38, doi: 10.3847/1538-4357/aa84af

Lesgourgues, J. 2011, arXiv e-prints, arXiv:1104.2932, doi: 10.48550/arXiv.1104.2932

Lewis, A., & Bridle, S. 2002, Phys. Rev. D, 66, 103511, doi: 10.1103/PhysRevD.66.103511

Lewis, A., Challinor, A., & Lasenby, A. 2000, ApJ, 538, 473, doi: 10.1086/309179

Li, H., Li, S.-Y., Liu, Y., et al. 2018, National Science Review, 6, 145, doi: 10.1093/nsr/nwy019

Linde, A. D. 1982, Physics Letters B, 108, 389, doi: 10.1016/0370-2693(82)91219-9

LiteBIRD Collaboration, Allys, E., Arnold, K., et al. 2023, Progress of Theoretical and Experimental Physics, 2023, 042F01, doi: 10.1093/ptep/ptac150

Lonappan, A. I., Namikawa, T., Piccirilli, G., et al. 2023, arXiv e-prints, arXiv:2312.05184, doi: 10.48550/arXiv.2312.05184

Lorensen, W. E., & Cline, H. E. 1987, SIGGRAPH Comput. Graph., 21, 163, doi: 10.1145/37402.37422

Lyth, D. H., Ungarelli, C., & Wands, D. 2003, Phys. Rev. D, 67, 023503, doi: 10.1103/PhysRevD.67.023503

Macellari, N., Pierpaoli, E., Dickinson, C., & Vaillancourt, J. E. 2011, MNRAS, 418, 888, doi: 10.1111/j.1365-2966.2011.19542.x

Madhavacheril, M. S., Qu, F. J., Sherwin, B. D., et al. 2024, ApJ, 962, 113, doi: 10.3847/1538-4357/acff5f

Maldacena, J. 2003, Journal of High Energy Physics, 2003, 013, doi: 10.1088/1126-6708/2003/05/013

Mantz, H., Jacobs, K., & Mecke, K. 2008, Journal of Statistical Mechanics: Theory and Experiment, 2008, 12015, doi: 10.1088/1742-5468/2008/12/P12015

Martin, J., Ringeval, C., & Vennin, V. 2014, Physics of the Dark Universe, 5, 75, doi: 10.1016/j.dark.2014.01.003

Martire, F. A., Banday, A. J., Martínez-González, E., & Barreiro, R. B. 2023, J. Cosmology Astropart. Phys., 2023, 049, doi: 10.1088/1475-7516/2023/04/049

Martire, F. A., Barreiro, R. B., & Martínez-González, E. 2022, J. Cosmology Astropart. Phys., 2022, 003, doi: 10.1088/1475-7516/2022/04/003

Masi, S. 2002, Progress in Particle and Nuclear Physics, 48, 243, doi: 10.1016/S0146-6410(02)00131-X

Mather, J. C., Cheng, E. S., Cottingham, D. A., et al. 1994, ApJ, 420, 439, doi: 10.1086/173574

McCulloch, W. S., & Pitts, W. 1943, The Bulletin of Mathematical Biophysics, 5, 115–133, doi: https://doi.org/10.1007/bf02478259

Minkowski, H. 1903, Mathematische Annalen, 57, 447. http://eudml.org/doc/158108

Miville-Deschênes, M. A., Duc, P. A., Marleau, F., et al. 2016, A&A, 593, A4, doi: 10.1051/0004-6361/201628503

Miville-Deschênes, M. A., Lagache, G., Boulanger, F., & Puget, J. L. 2007, A&A, 469, 595, doi: 10.1051/0004-6361:20066962

Mousset, L., Allys, E., Price, M. A., et al. 2024, arXiv e-prints, arXiv:2407.07007, doi: 10.48550/arXiv.2407.07007

Mudur, N., & Finkbeiner, D. P. 2022, arXiv e-prints, arXiv:2211.12444, doi: 10.48550/arXiv.2211.12444

Padoan, P., Goodman, A., Draine, B. T., et al. 2001, ApJ, 559, 1005, doi: 10.1086/322504

Page, L., Hinshaw, G., Komatsu, E., et al. 2007, ApJS, 170, 335, doi: 10.1086/513699

PanEx Collaboration. 2024

Partridge, R. B. 1995, Cambridge Astrophysics Series, 25

Peebles, P. J. E., & Yu, J. T. 1970, ApJ, 162, 815, doi: 10.1086/150713

Penzias, A. A., & Wilson, R. W. 1965, ApJ, 142, 419, doi: 10.1086/148307

Perlmutter, S., Aldering, G., Goldhaber, G., et al. 1999, ApJ, 517, 565, doi: 10.1086/307221

Planck Collaboration Int. XLVIII. 2016a, A&A, 596, A109, doi: 10.1051/0004-6361/201629022

—. 2016b, A&A, 596, A109, doi: 10.1051/0004-6361/201629022

Planck Collaboration Int. XX. 2015, A&A, 576, A105, doi: 10.1051/0004-6361/201424086

Planck Collaboration Int. XXII. 2015, A&A, 576, A107, doi: 10.1051/0004-6361/201424088

Planck Collaboration Int. XXX. 2016, A&A, 586, A133, doi: 10.1051/0004-6361/201425034

Planck Collaboration Int. XXXVIII. 2016, A&A, 586, A141, doi: 10.1051/0004-6361/201526506

Planck Collaboration IV. 2020, A&A, 641, A4, doi: 10.1051/0004-6361/201833881

Planck Collaboration IX. 2020, A&A, 641, A9, doi: 10.1051/0004-6361/201935891

Planck Collaboration V. 2020, A&A, 641, A5, doi: 10.1051/0004-6361/201936386

Planck Collaboration VI. 2020, A&A, 641, A6, doi: 10.1051/0004-6361/201833910

Planck Collaboration VII. 2020, A&A, 641, A7, doi: 10.1051/0004-6361/201935201

Planck Collaboration VIII. 2020, A&A, 641, A8, doi: 10.1051/0004-6361/201833886

Planck Collaboration X. 2016, A&A, 594, A10, doi: 10.1051/0004-6361/201525967

Planck Collaboration XI. 2020, A&A, 641, A11, doi: 10.1051/0004-6361/201832618

Planck Collaboration XII. 2020, A&A, 641, A12, doi: 10.1051/0004-6361/201833885

Planck Collaboration XIII. 2014, A&A, 571, A13, doi: 10.1051/0004-6361/201321553

—. 2016, A&A, 594, A13, doi: 10.1051/0004-6361/201525830

Planck Collaboration XXIV. 2014, A&A, 571, A24, doi: 10.1051/0004-6361/201321554

Poidevin, F., Génova-Santos, R. T., Rubiño-Martín, J. A., et al. 2023, MNRAS, 519, 3481, doi: 10.1093/mnras/stac3151

POLARBEAR Collaboration. 2017, ApJ, 848, 121, doi: 10.3847/1538-4357/aa8e9f

—. 2022, ApJ, 931, 101, doi: 10.3847/1538-4357/ac6809

Puglisi, G., Galluzzi, V., Bonavera, L., et al. 2018, ApJ, 858, 85, doi: 10.3847/1538-4357/aab3c7

Regaldo-Saint Blancard, B., Levrier, F., Allys, E., Bellomi, E., & Boulanger, F. 2020, A&A, 642, A217, doi: 10.1051/0004-6361/202038044

Remazeilles, M., Delabrouille, J., & Cardoso, J.-F. 2011, MNRAS, 418, 467, doi: 10.1111/j.1365-2966.2011.19497.x

Remazeilles, M., Dickinson, C., Banday, A. J., Bigot-Sazy, M. A., & Ghosh, T. 2015, MNRAS, 451, 4311, doi: 10.1093/mnras/stv1274

Riess, A. G., Filippenko, A. V., Challis, P., et al. 1998, AJ, 116, 1009, doi: 10.1086/300499

Robertson, H. P. 1935, ApJ, 82, 284, doi: 10.1086/143681

Rosenblatt, F. 1958, Psychological review, 65 6, 386. https://api.semanticscholar.org/CorpusID:12781225

Rotti, A., & Huffenberger, K. 2016, J. Cosmology Astropart. Phys., 2016, 034, doi: 10.1088/1475-7516/2016/09/034

Rubin, V. C., & Ford, W. Kent, J. 1970, ApJ, 159, 379, doi: 10.1086/150317

Rybicki, G. B., & Lightman, A. P. 1985, Radiative processes in astrophysics. (John Wiley and Sons)

Sachs, R. K., & Wolfe, A. M. 1967, ApJ, 147, 73, doi: 10.1086/148982

Saha, R., Prunet, S., Jain, P., & Souradeep, T. 2008, Phys. Rev. D, 78, 023003, doi: 10.1103/PhysRevD.78.023003

San, M., Herman, D., Erikstad, G. B., Galloway, M., & Watts, D. 2022, A&A, 666, A107, doi: 10.1051/0004-6361/202244133

Sato, K. 1981, MNRAS, 195, 467, doi: 10.1093/mnras/195.3.467

Sayre, J. T., Reichardt, C. L., Henning, J. W., et al. 2020, Phys. Rev. D, 101, 122003, doi: 10.1103/PhysRevD.101.122003

Seljebotn, D. S., Bærland, T., Eriksen, H. K., Mardal, K. A., & Wehus, I. K. 2019, A&A, 627, A98, doi: 10.1051/0004-6361/201732037

Silk, J. 1968, ApJ, 151, 459, doi: 10.1086/149449

Smoot, G. F., Bennett, C. L., Kogut, A., et al. 1992, ApJ, 396, L1, doi: 10.1086/186504

Spider Collaboration. 2022, ApJ, 927, 174, doi: 10.3847/1538-4357/ac20df

SPT Collaboration. 2023, Phys. Rev. D, 108, 023510, doi: 10.1103/PhysRevD.108.023510

Starobinsky, A. A. 1982, Physics Letters B, 117, 175, doi: 10.1016/0370-2693(82)90541-X

Stevenson, M. A. 2014, ApJ, 781, 113, doi: 10.1088/0004-637X/781/2/113

Stompor, R., Errard, J., & Poletti, D. 2016, Phys. Rev. D, 94, 083526, doi: 10.1103/PhysRevD.94.083526

Stompor, R., Leach, S., Stivoli, F., & Baccigalupi, C. 2009, MNRAS, 392, 216, doi: 10.1111/j.1365-2966.2008.14023.x

Sunyaev, R. A., & Zeldovich, Y. B. 1972, Comments on Astrophysics and Space Physics, 4, 173

Tegmark, M., & Efstathiou, G. 1996, MNRAS, 281, 1297, doi: 10.1093/mnras/281.4.1297

Thorne, B., Dunkley, J., Alonso, D., & Næss, S. 2017, MNRAS, 469, 2821, doi: 10.1093/mnras/stx949

Thorne, B., Knox, L., & Prabhu, K. 2021, MNRAS, 504, 2603, doi: 10.1093/mnras/stab1011

Tristram, M., & Ganga, K. 2007, Reports on Progress in Physics, 70, 899, doi: 10.1088/0034-4885/70/6/R02

Tristram, M., Banday, A. J., Górski, K. M., et al. 2022, Phys. Rev. D, 105, 083524, doi: 10.1103/PhysRevD.105.083524

Tristram, M., Banday, A. J., Douspis, M., et al. 2024, A&A, 682, A37, doi: 10.1051/0004-6361/202348015

von Hausegger, S., Gammelgaard Ravnebjerg, A., & Liu, H. 2019, MNRAS, 487, 5814, doi: 10.1093/mnras/stz1582

Walker, A. G. 1937, Proceedings of the London Mathematical Society, 42, 90, doi: 10.1112/plms/s2-42.1.90

Wang, G.-J., Shi, H.-L., Yan, Y.-P., et al. 2022, ApJS, 260, 13, doi: 10.3847/1538-4365/ac5f4a

Weinberg, S. 1977, The First Three Minutes. A Modern View of the Origin of the Universe (Basic Books)

Weinberg, S. 2008, Cosmology (Oxford University Press)

Yan, Y.-P., Wang, G.-J., Li, S.-Y., & Xia, J.-Q. 2023, ApJ, 947, 29, doi: 10.3847/1538-4357/acbfb4

Yao, J., Krachmalnicoff, N., Foschi, M., Puglisi, G., & Baccigalupi, C. 2024, A&A, 686, A290, doi: 10.1051/0004-6361/202449827

Yao, J., Zhang, L., Zhao, Y., et al. 2018, ApJS, 239, 36, doi: 10.3847/1538-4365/aaef7a

Zaldarriaga, M., & Seljak, U. 1997, Phys. Rev. D, 55, 1830, doi: 10.1103/PhysRevD.55.1830

Zeldovich, Y. B. 1972, MNRAS, 160, 1P, doi: 10.1093/mnras/160.1.1P

Zonca, A., Singer, L., Lenz, D., et al. 2019, Journal of Open Source Software, 4, 1298, doi: 10.21105/joss.01298

Zonca, A., Thorne, B., Krachmalnicoff, N., & Borrill, J. 2021, Journal of Open Source Software, 6, 3783, doi: 10.21105/joss.03783

Zwicky, F. 2009, General Relativity and Gravitation, 41, 207, doi: 10.1007/s10714-008-0707-4